STATISTICAL SIGNAL PROCESSING FOR ACOUSTIC DIRECTION FINDING AND FOR ROADWAY SOUND-LEVEL DISTRIBUTION MODELING

MUHAMMAD MUAZ

Ph.D

The Hong Kong Polytechnic University

2018

The Hong Kong Polytechnic University

Department of Electronic and Information Engineering

Statistical Signal Processing for Acoustic Direction Finding and for Roadway Sound-Level Distribution Modeling

Muhammad MUAZ

A thesis submitted in partial fulfilment of the requirements

for the degree of Doctor of Philosophy

April 2018

CERTIFICATE OF ORIGINALITY

I hereby declare that this thesis is my own work and that, to the best of my knowledge and belief, it reproduces no material previously published or written, nor material that has been accepted for the award of any other degree or diploma, except where due acknowledgment has been made in the text.

_____ (Signed)

Muhammad MUAZ (Name of student)

Abstract

This thesis presents two investigations in two parts:

I *Azimuth-elevation bivariate direction finding using a higher-order "figure-8" sensor and an isotropic sensor.*

A "p-u probe" (a.k.a. a "p-v probe") comprises one pressure-sensor (which is isotropic) and one uni-axial particle-velocity sensor (which has a "figure-8" bi-directional spatial directivity). This p-u probe may be generalized, by allowing the figure-8 bi-directional sensor to have a higher order of directivity. This "higher-order p-v probe" has not previously been investigated anywhere in the open literature (to the best knowledge of the present authors). For such a sensing system, this work is first (1) to develop closed-form eigen-based signal-processing algorithms for azimuth-elevation direction finding; (2) to analytically derive the associated Cramér-Rao lower bounds (CRB), which is expressed explicitly in terms of the two constituent sensors' spatial geometry and in terms of the figure-8 sensor's directivity order; (3) to verify (via Monte Carlo simulations) the proposed direction-of-arrival estimators' efficacy and closeness to the Cramér-Rao lower bounds. Here, the two constituent sensors of higher-order p-v probe may be spatially displaced.

II *Leptokurtic probability density modeling of roadway sound-levels measured at different floors of a high-rise building.*

The tails of roadway sound-level distributions decay slower than the tails of the Gaussian distribution. This highlights the need to instead use leptokurtic distributions in modeling. To gain new insights into the roadway sound-level distribution, this work is first in the open literature (1) to try out a wide range of well-known leptokurtic probability-density functions of two, three and four parameters, and ranks their goodness-of-fit to sound-pressure-level data measured at a high-rise building in Hong Kong, overlooking the roadway vehicular traffic; (2) to check if a probability density (scalar) metric (i.e. variance, skewness, excess-kurtosis, third central-moment, fourth central moment, fourth cumulant, and peakedness) is a "sufficient statistic" to explain the goodness-of-fit ranks of a candidate probability density function; (3) to analyze the statistical distributions of roadway sound-level data empirically-measured at different days and different vertical locations of a high-rise building.

Publications

Journal paper

1. **M. Muaz**, Y. I. Wu, K. T. Wong, and D. Su, "A higher-order "figure-8" sensor and an isotropic sensor for azimuth-elevation bivariate direction finding," accepted on March 06, 2018 to appear in *The Journal of the Acoustical Society of America*.

Papers under preparation:

2. T.-c. Lin, **M. Muaz**, K. T. Wong, S.-k. Tang, and H. T. Ng, "Probability distribution modeling of roadway sound-level measured on different days at a high-rise building."

3. T.-c. Lin, **M. Muaz**, K. T. Wong, S.-k. Tang, and H. T. Ng, "Variation in the roadway sound-level probability distribution with the microphone's floor-level in a high-rise building."

Conference papers (presented and published)

1. **M. Muaz**, S.-k. Tang, T.-c. Lin, and H. T. Ng, "Fitting "bad urban" roadside motor traffic sound level to skewed distribution models," *INTER-NOISE and NOISE-CON Congress and Conference Proceedings (INCE)*, vol. 255, no. 2, pp. 5909-5914, August 2017.

2. **M. Muaz**, Y. I. Wu, D. Su, and K. T. Wong, "Direction finding using a p-v probe of higher order," *The Journal of the Acoustical Society of America*, vol. 141, no. 5, p. 3651, June 2017.

Acknowledgments

I am thankful to Almighty God for giving me the strength to continue this work.

I am most indebted to my mentor, Dr. Kainam Thomas Wong, who helped me to get the opportunity to study in Hong Kong. I could not have achieved my current academic standing without his patient guidance, problem formulations, design of the high-level approach, fine-tuning of the methodologies, the various drafts' thorough revisions, word-by-word checking of my papers and this thesis, and the formation of the multidisciplinary team of researchers.

I am very thankful to the Hong Kong Polytechnic University for providing a conducive working atmosphere and financial support for 3 years. I acknowledge the flexibility and the final year's financial support of the Higher Education Commission of Pakistan during my studies in Hong Kong.

I am highly obliged to Professor Tsair-chuan Lin (National Taipei University, Taiwan) for providing the statistical concepts, algorithms and many computer codes for the statistical analysis in Chapters 4–6. I am extremely thankful to Dr. Yue Ivan Wu (Sichuan University, China) and Dr. Yang Song (Nanyang Technological University, Singapore) for guiding me in great details with the algorithm development, the analysis, and the Monte Carlo simulations in Chapter 2. I am highly appreciative of Professor Shiu-keung Tang (Hong Kong Polytechnic University) for his financial backup and support for providing the data in Chapters 4–6. I am greatly thankful to my colleagues, Mr. Ho Ting Ng and Mr. Chibuzo Joseph Nnonyelu, in helping me to obtain the necessary research data and computer.

Lastly, I am always grateful to the unending love and care of my parents, sisters, sisters-in-law, brothers, friends, and fiancè.

Table of Contents

Part I

Azimuth-elevation bivariate direction finding using a higher-order figure-8 sensor and an isotropic sensor

In part I, a non-collocated "p-v probe" of higher order for direction-of-arrival estimation is described [1].

Contribution: This work presents general-order non-collocated p-v probe [1] as an alternative to existing sensing systems, like the "v-v probe" [2], or the tri-axial velocity sensor [3, 4], or the four-component acoustic vector-sensor (AVS) consisting of a tri-axial velocity sensor and a collocating pressure-sensor [5, 6, 7]. The use of a pressure sensor (instead of additional "figure-8" sensor/s) may simplify the hardware and any calibration.

Chapter 1 introduces the non-collocated "higher-order p-v probe".

[1] The term non-collocated means that the constituent pressure sensor and the figure-8 sensor are not mathematically assumed to be located at the same spatial coordinates.

Chapter 1

Introduction

1.1 Non-collocated "higher-order p-v probe"

The p-v probe is an acoustical sensing system that comprises

(a) an isotropic *p*ressure-sensor, and

(b) a uni-axial [1] particle-*v*elocity [2] sensor, whose gain-response is bi-directional [3] , like a figure-8, i.e. $\cos(\gamma)$ in mathematical form, where γ represents the angle of impinging signal from the directional sensor's axis. Such a uni-axial particle-velocity sensor measures one Cartesian component of the acoustical wavefield's particle velocity vector.

[1] Uni-axial means that the sensor has a single imaginary line along which the gain response of the sensor is oriented.

[2] Particle velocity here is referring to the velocity of air particles when the sound wave is transmitted.

[3] Bi-directional means the sensor is designed to receive signals from two opposite directions.

For a listing of the key literature on p-v probes and their physical shapes, please refer to [8].

A single sensor array like the higher-order p-u probe has been used in the open literature for closed-form eigen-based direction-of-arrival estimation [9, 10, 11, 12].

For instance, [13] has used one pressure sensor and three high order velocity sensors located at the origin but orthogonal to each other. The paper presents the three velocity sensor in a vector with unit power as:

$$\mathbf{a} \stackrel{\text{def}}{=} \left[\left\{ \sin\theta\cos\phi \right\}^k, \left\{ \sin\theta\sin\phi \right\}^k, \left\{ \cos\theta \right\}^k, 1 \right]^T \tag{1.1}$$

where k is the order of velocity sensor's direction cosine and the fourth row represents the isotropic pressure sensor. The author's eigen-based parameter estimation calculates the steering vector that is unknown to a complex factor c. That estimated steering vector received at the sensor array is:

$$\hat{\mathbf{a}} \stackrel{\text{def}}{=} \left[\hat{a}_x, \hat{a}_y, \hat{a}_z, \hat{a}_p \right]^{\mathrm{T}} \approx \; c \; \mathbf{a}_{(k_x, k_y, k_z, 1)} \tag{1.2}$$

where k_ε refers to the order of velocity sensors with $\varepsilon \in x, y, z$. The estimated arrival angles are then formulated with the help of equations (1.3) and (1.4).

$$\hat{\theta} = \cos^{-1}\left[\left| \left(\frac{\hat{a}_z}{\hat{a}_p} \right)^{1/k_z} \right| \operatorname{sgn}\left(\Re\left(\frac{\hat{a}_z}{\hat{a}_p} \right) \right) \right] \tag{1.3}$$

$$\hat{\phi} = \operatorname{sgn}\left[\left| \left(\frac{\hat{a}_y}{\hat{a}_p} \right)^{1/k_y} \right| \operatorname{sgn}\left(\Re\left(\frac{\hat{a}_y}{\hat{a}_p} \right) \right) \right] \cos^{-1}\left[\csc(\hat{\theta}) \left| \left(\frac{\hat{a}_x}{\hat{a}_p} \right)^{1/k_x} \right| \operatorname{sgn}\left(\Re\left(\frac{\hat{a}_x}{\hat{a}_p} \right) \right) \right] \tag{1.4}$$

In equations (1.3) and (1.4), $k = \{1, 3, 5, ...\}$. Similarly, [14] has used a pressure sensor and three spatially spread first order velocity sensors oriented along the axis they lie on and has derived the closed form solutions of (θ, ϕ) using the array manifold given in (1.5) and depicted in figure 1.1.

$$\mathbf{a} \overset{\text{def}}{=} \left[\sin\theta\cos\phi\ e^{j\frac{2\pi\Delta_{px}}{\lambda}\sin\theta\cos(\phi)},\ \ \sin\theta\sin\phi\ e^{j\frac{2\pi\Delta_{py}}{\lambda}\sin\theta\sin\phi},\ \ \cos\theta\ e^{j\frac{2\pi\Delta_{pz}}{\lambda}\cos\theta},\ \ 1\right]^T \tag{1.5}$$

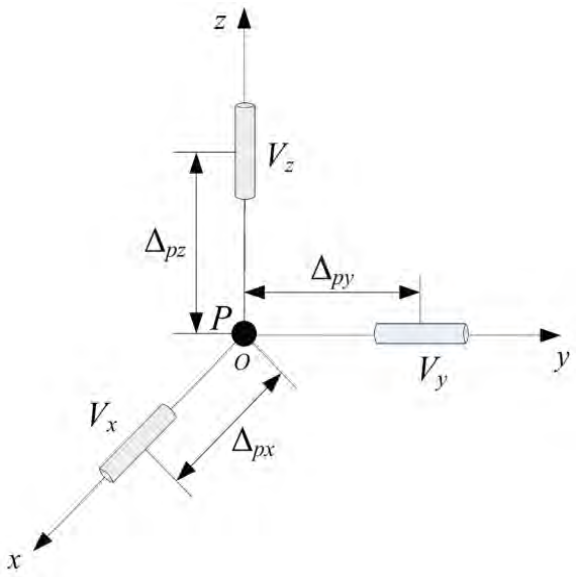

Figure 1.1: One pressure sensor and 3 non-collocated velocity sensors creating pyramid kind of configuration [14].

Similarly, high directional velocity sensors have been described and explored in [15, 16, 17, 18]. To approximate the arrival angles of an acoustic signal through the velocity vector sensor, both numerical and closed form solutions are obtained (e.g., see [19, 8, 13]).

This work generalizes the customary p-v probe, by allowing the figure-8 sensor to have any arbitrarily higher (positive integer) order k of directivity. The name "higher-order p-v probe" is coined for the p-v probe with high-order gain response for its constituent figure-8 sensor (mathematically as $\cos^k(\gamma)$, $k \in \mathbb{W}$).

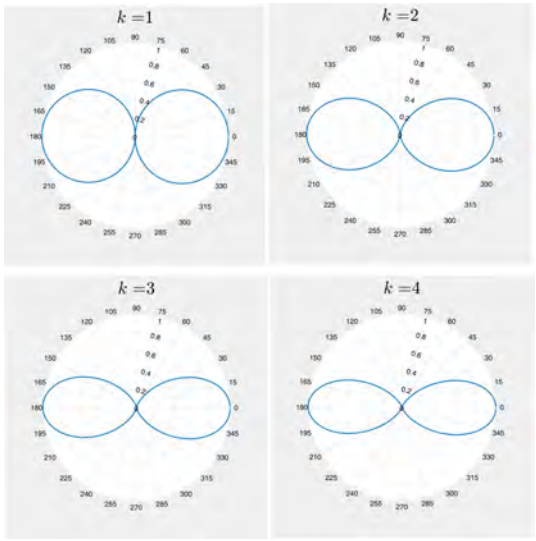

Figure 1.2: Gain response of a kth-order figure-8 sensor.

1.2 Higher-order "figure-8" sensor

1.2.1 Gain response

Gain response refers to the directivity gain, which measures the difference in the response of a sensor or a sensor array to the signals impinging from different directions. The "figure-8" gain response can be achieved by an acoustic sensor measuring the gradient of the sound pressure. The first-order gradient of sound pressure is proportional to the sensor's gain response i.e., $\cos(\theta)$. The second-order gradient corresponds to the square of sensor's gain response i.e., $\cos^2(\theta)$, and so

on. With increasing value of k, in the gain response of the higher-order figure-8 sensor $\cos^k(\gamma)$, the lobes of figure-8 sensor becomes more sharper or more narrowly directional (see Figure 1.2) [15, Chapter 8]. Among the three Cartesian axes, if a kth-order figure-8 sensor is:

- Oriented along the x-axis, its gain response equals $[\sin(\theta)\cos(\phi)]^k$. Here, $\theta \in [0, \pi]$ represents the polar angle (a.k.a. the zenith angle), and $\phi \in [0, 2\pi)$ denotes the azimuth angle measured from the positive x-axis (see Figure 1.3).
- Oriented along the y-axis, the gain response becomes $[\sin(\theta)\sin(\phi)]^k$.
- Oriented along the z-axis, the gain response becomes $\cos^k(\theta)$.

1.2.2 Hardware implementations

There has been a number of hardware implementations of higher-order pressure gradient sensors to achieve the figure-8 bi-directional gain response. Second-order figure-8 bi-directional acoustic sensors have been implemented in hardware in [20, 21, 22, 23, 24, 25, 26, 27, 28, 29, 30, 31]. Third-order ones have been implemented in hardware in [23, 29, 16] page. Fifth-order ones have been implemented in hardware in [32]. Other higher-order ones have been implemented in hardware in [23, 29]. These hardware implementations of *second*-order or *higher*-order p-v probes, dating over from 1942 to 2008, show that second-order/"higher-order p-v probes" are established yet current sensing systems with continuing practical relevance.

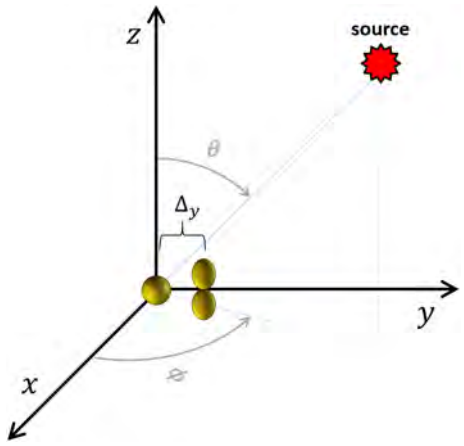

Figure 1.3: An acoustic source impinging from (θ, ϕ) angles of arrival with reference to a "p-v probe".

1.3 Nine configurations of higher-order p-v probe

Specifically, suppose that the isotropic sensor (i.e. a pressure-sensor) is located at the origin. Also, assume that the figure-8 sensor lies on one of the three Rectangular axes as well as is oriented in parallel to one of the Cartesian axes. Then, there would be 9 distinct combinations of the figure-8 sensor's location and axial orientation. Please see Figure 1.4. Figure 1.4(a), for example, corresponds to a pressure sensor at the Cartesian origin, with a figure-8 directional sensor at the Cartesian position of $(\Delta_x, 0, 0)$ but orienting along the x-axis. Figure 1.4(b), in contrast, has the figure-8 directional sensor at the Cartesian position of $(0, \Delta_y, 0)$ but still orienting along the x-axis.

Chapter 2 explains the proposed direction-of-arrival estimator using the non-collocated higher-order p-v probe. Therein, the new eigen-based closed-form direction finding algorithm is discussed. Next, the Monte Carlo simulations show

the proposed estimators' (statistical) efficiency. In the end, Part I (Chapters 1 – 2) is concluded as the paragraph numbered (Part I) in the conclusion chapter.

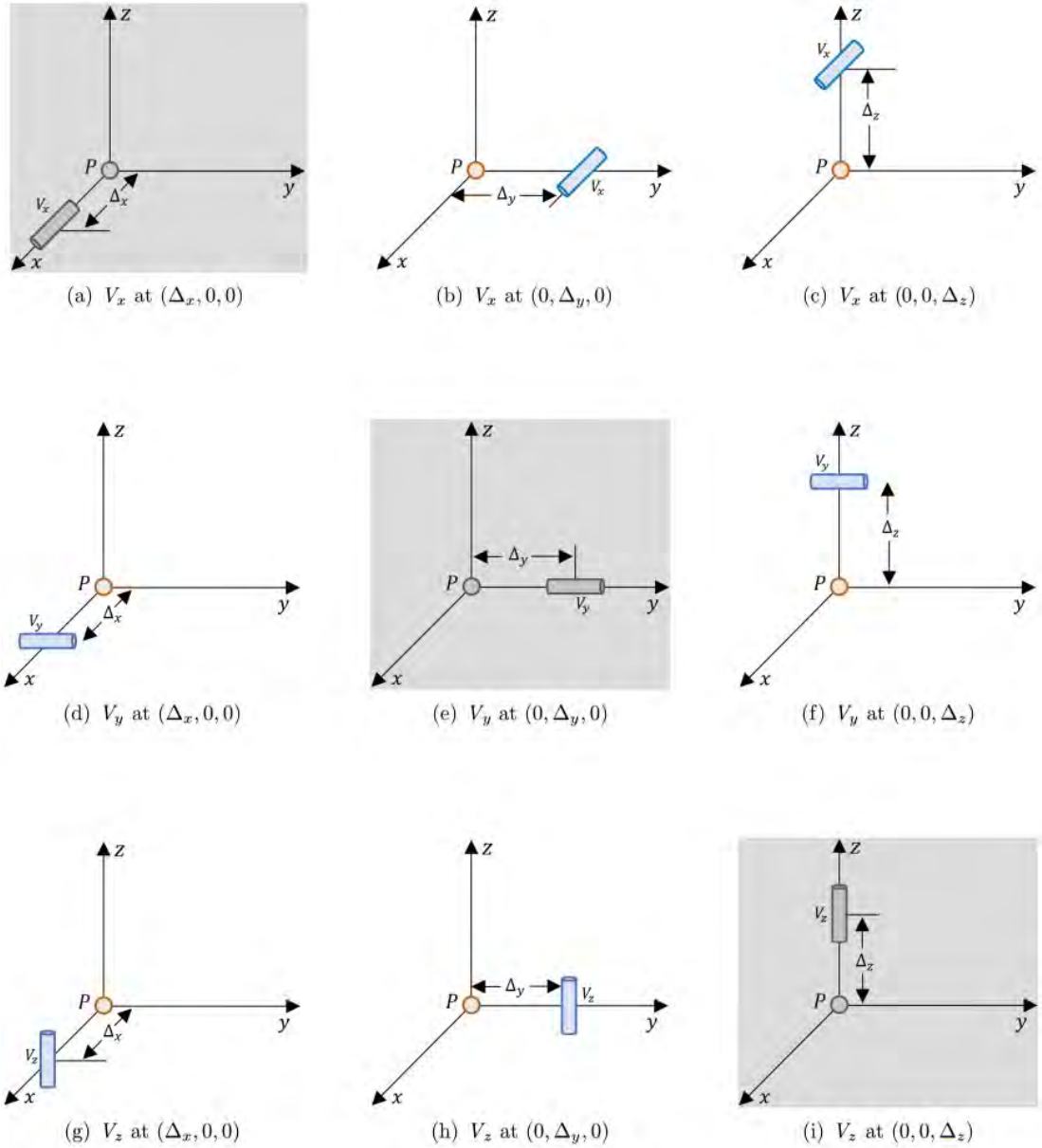

(a) V_x at $(\Delta_x, 0, 0)$ (b) V_x at $(0, \Delta_y, 0)$ (c) V_x at $(0, 0, \Delta_z)$

(d) V_y at $(\Delta_x, 0, 0)$ (e) V_y at $(0, \Delta_y, 0)$ (f) V_y at $(0, 0, \Delta_z)$

(g) V_z at $(\Delta_x, 0, 0)$ (h) V_z at $(0, \Delta_y, 0)$ (i) V_z at $(0, 0, \Delta_z)$

Figure 1.4: The nine configurations of higher-order p-v probe under investigation. The shaded configurations cannot facilitate bivariate azimuth-elevation direction-of-arrival estimation. Please see Chapter 2.

Chapter 2

Closed-form direction-of-arrival estimation of the higher-order p-v probe

Section 1.3 showed nine configurations of the non-collocated higher-order p-v probe. In this chapter, for each of these 9 configurations at any specific sensor-order k, Section 2.1 will define their array manifold. Section 2.2 will derive a new closed-form estimator of the incident source's azimuth-elevation bivariate direction-of-arrival (or, for 3 of the 9 array configurations, will explain why such an estimator is mathematically impossible), Section 2.3 will analytically derive the corresponding Cramér-Rao lower bound, in a simple mathematical form that is explicitly in terms of the array geometry and explicitly in terms of sensor order k. Section 2.4 will then present Monte Carlo simulations of the proposed estimator, showing its closeness to the derived Cramér-Rao lower bound.

2.1 The array manifold vector of the generalized p-u probe's nine configurations under investigation

The 2×1 array manifold of any location/orientation configuration of Figure 1.4 is mathematically denoted as

$$\mathbf{a}_{P,V_\zeta}^{(\varepsilon)}(\theta,\phi) \;=\; \begin{bmatrix} 1 \\ \eta_1^k \; e^{j2\pi\frac{\Delta_\varepsilon}{\lambda}\eta_2} \end{bmatrix}, \tag{2.1}$$

The first entry refers to the isotropic sensor at the Cartesian origin, whereas the second entry corresponds to the figure-8 directional sensor placed away from the Cartesian origin. Here, the superscript $\varepsilon \in \{x, y, z\}$ identifies the Rectangular axis on which the higher-order figure-8 sensor lies, the subscript $\zeta \in \{x, y, z\}$ indicates the direction of higher-order figure-8 sensor, and

$$\eta_1 \;:=\; \begin{cases} \cos(\theta), & \text{if } \zeta = z; \\ \sin(\phi)\sin(\theta), & \text{if } \zeta = y; \\ \cos(\phi)\sin(\theta), & \text{if } \zeta = x. \end{cases}$$

$$\eta_2 \;:=\; \begin{cases} \cos(\theta), & \text{if } \epsilon = z; \\ \sin(\phi)\sin(\theta), & \text{if } \epsilon = y; \\ \cos(\phi)\sin(\theta), & \text{if } \epsilon = x. \end{cases}$$

The first entry's magnitude equals unity, on account of the pressure-sensor's isotropicity. It has no complex phase, because of its location at the Cartesian origin, hence no spatial phase factor. The second entry's magnitude of η_1^k corresponds

to the kth-order figure-8 gain pattern oriented along the ζ Cartesian coordinate. The second entry's complex phase $e^{j2\pi\frac{\Delta_\epsilon}{\lambda}\eta_2}$ represents a spatial phase factor for the figure-8 sensor's location of $\Delta_\epsilon \approx 0$ out on the ϵ Cartesian coordinate. The sign of the real-valued scalar η_1 specifies the hemisphere from which the source impinges. E.g. at $\zeta = z$, $\text{sgn}(\eta_1) = \text{sgn}(\cos(\theta)) > 0$ would mean that the source impinges from the upper hemisphere, whereas $\text{sgn}(\eta_1) = \text{sgn}(\cos(\theta)) < 0$ means the lower hemisphere. Here, $\text{sgn}(\cdot)$ denotes the signum function.

Figure 1.4's nine location/orientation configurations' array manifolds are presented in Table 2.1.

Table 2.1: The array manifold for various configurations of kth-order p-u probe. (Please see Equation (2.1).)

configuration (a): $\mathbf{a}^{(x)}_{P,V_x}(\theta,\phi) = \begin{bmatrix} 1 & \\ u^k & e^{j2\pi\frac{\Delta_x}{\lambda}u} \end{bmatrix}$	configuration (b): $\mathbf{a}^{(y)}_{P,V_x}(\theta,\phi) = \begin{bmatrix} 1 & \\ u^k & e^{j2\pi\frac{\Delta_y}{\lambda}v} \end{bmatrix}$	configuration (c): $\mathbf{a}^{(z)}_{P,V_x}(\theta,\phi) = \begin{bmatrix} 1 & \\ u^k & e^{j2\pi\frac{\Delta_z}{\lambda}w} \end{bmatrix}$
configuration (d): $\mathbf{a}^{(x)}_{P,V_y}(\theta,\phi) = \begin{bmatrix} 1 & \\ v^k & e^{j2\pi\frac{\Delta_x}{\lambda}u} \end{bmatrix}$	configuration (e): $\mathbf{a}^{(y)}_{P,V_y}(\theta,\phi) = \begin{bmatrix} 1 & \\ v^k & e^{j2\pi\frac{\Delta_y}{\lambda}v} \end{bmatrix}$	configuration (f): $\mathbf{a}^{(z)}_{P,V_y}(\theta,\phi) = \begin{bmatrix} 1 & \\ v^k & e^{j2\pi\frac{\Delta_z}{\lambda}w} \end{bmatrix}$
configuration (g): $\mathbf{a}^{(x)}_{P,V_z}(\theta,\phi) = \begin{bmatrix} 1 & \\ w^k & e^{j2\pi\frac{\Delta_x}{\lambda}u} \end{bmatrix}$	configuration (h): $\mathbf{a}^{(y)}_{P,V_z}(\theta,\phi) = \begin{bmatrix} 1 & \\ w^k & e^{j2\pi\frac{\Delta_y}{\lambda}v} \end{bmatrix}$	configuration (i): $\mathbf{a}^{(z)}_{P,V_z}(\theta,\phi) = \begin{bmatrix} 1 & \\ w^k & e^{j2\pi\frac{\Delta_z}{\lambda}w} \end{bmatrix}$

These nine array manifolds are functionally inter-related:

$$\text{(b)} \leftrightarrow \text{(d)}: \quad \mathbf{a}^{(x)}_{P,V_y}(\theta,\phi) = \mathbf{a}^{(y)}_{P,V_x}\left(\theta, \frac{\pi}{2}-\phi\right), \tag{2.2}$$

$$\text{(c)} \leftrightarrow \text{(f)}: \quad \mathbf{a}^{(z)}_{P,V_x}(\theta,\phi) = \mathbf{a}^{(z)}_{P,V_y}\left(\theta, \frac{\pi}{2}-\phi\right), \tag{2.3}$$

$$\text{(g)} \leftrightarrow \text{(h)}: \quad \mathbf{a}^{(y)}_{P,V_z}(\theta,\phi) = \mathbf{a}^{(x)}_{P,V_z}\left(\theta, \frac{\pi}{2}-\phi\right), \tag{2.4}$$

$$\text{(e)} \leftrightarrow \text{(a)}: \quad \mathbf{a}^{(y)}_{P,V_y}(\theta,\phi) = \mathbf{a}^{(x)}_{P,V_x}\left(\theta, \frac{\pi}{2}-\phi\right), \tag{2.5}$$

$$\text{(i)} \leftrightarrow \text{(a)} \leftrightarrow \text{(e)}: \quad \mathbf{a}^{(z)}_{P,V_z}(\theta,\phi) = \mathbf{a}^{(x)}_{P,V_x}\left(\frac{\pi}{2}-\theta, 0\right), \tag{2.6}$$

$$= \mathbf{a}^{(y)}_{P,V_y}\left(\frac{\pi}{2}-\theta, \frac{\pi}{2}\right). \tag{2.7}$$

Lastly, if the locations of two component-sensors are interchanged, the resulting array manifold is obtainable from the old one by a complex conjugation, then a multiplication by $e^{j2\pi\frac{\Delta_\epsilon}{\lambda}\eta_2}$.

2.2 Eigen-based closed-form estimation of the azimuth-elevation direction-of-arrival

Eigen-based direction-of-arrival estimation involves an intermediate algorithmic step, wherein the incident signal's steering vector is approximated maximally to an undefined c (a complex number). This undefined c occurs from the data-covariance matrix after being passed through the eigen-decomposition step. (Suppose $\mathbf{e}$ equals eigenvector of the data correlation matrix, then $c\mathbf{e}$ must also be a valid eigenvector $\forall c \neq 0$.) That is, available to subsequent algorithmic steps is a steering-vector estimate, $\hat{\mathbf{a}}^{(\varepsilon)}_{P,V_\zeta} \approx c\, \mathbf{a}^{(\varepsilon)}_{P,V_\zeta}(\theta,\phi)$. [1]

[1] Suppose a signal $s(t)$ reaches the p-u probe, but becomes corrupted additively by the p-u probe's thermal noise-vector $\mathbf{n}(t)$. The p-u probe's measurement then equals to a 2×1 data

(In the ideal case of no noise or an infinite number of time samples, this approximation would become equality.) Hence, the problem is how to estimate θ and ϕ, given $\hat{\mathbf{a}}^{(\varepsilon)}_{P,V_\zeta}$, for each of the 9 configurations in Figure 1.4 and Table 2.1, with k being any natural number that is prior known.

The unknown scalar c may be eliminated as follows, on account of (2.1):

$$\frac{\left[\hat{\mathbf{a}}^{(\varepsilon)}_{P,V_\zeta}\right]_2}{\left[\hat{\mathbf{a}}^{(\varepsilon)}_{P,V_\zeta}\right]_1} \;=\; \eta_1^k \; e^{j2\pi\frac{\Delta_\varepsilon}{\lambda}\eta_2}, \tag{2.8}$$

with $[\cdot]_j$ denoting jth vector element.

For any prior known $\Delta_\varepsilon \in \left(0, \frac{\lambda}{2}\right]$, [2] Equation (2.8) leads to

$$\hat{\eta}_1 \;=\; \left|\frac{\left[\hat{\mathbf{a}}^{(\varepsilon)}_{P,V_\zeta}\right]_2}{\left[\hat{\mathbf{a}}^{(\varepsilon)}_{P,V_\zeta}\right]_1}\right|^{1/k} \operatorname{sgn}(\eta_1), \tag{2.9}$$

$$\hat{\eta}_2 \;=\; \frac{\lambda}{2\pi\Delta_\varepsilon}\,\angle\left(\operatorname{sgn}(\eta_1)\,\frac{\left[\hat{\mathbf{a}}^{(\varepsilon)}_{P,V_\zeta}\right]_2}{\left[\hat{\mathbf{a}}^{(\varepsilon)}_{P,V_\zeta}\right]_1}\right). \tag{2.10}$$

If $\Delta_\varepsilon > \frac{\lambda}{2}$, the spatial phase factor $e^{j\frac{2\pi\Delta_\varepsilon}{\lambda}\eta_2}$ has no one-to-one mapping with η_2; hence, Equations (2.9) and (2.10) cannot distinctively estimate both the azimuth

vector of $\mathbf{z}(t_m) = s(t_m)\mathbf{a} + \mathbf{n}(t_m)$ at the mth time sample. From M such time samples, a data correlation matrix of $\hat{\mathbf{C}} = \sum_{m=1}^{M} \mathbf{z}(t_m)[z(t_m)]^H$ is formed, where the superscript ^{H} symbolizes the Hermitian operator. Suppose further that $\{s(t)\}$ and $\{\mathbf{n}(t)\}$ are each temporally stationary and not cross-correlated between them. Then, $\hat{\mathbf{C}} \approx \mathbf{C} = MP_s\mathbf{a}\mathbf{a}^H + MP_n\mathbf{I}$, where P_s denotes the power of the incident signal, $\mathbf{a}$ symbolizes the impinging source's steering vector, P_n refers to the thermal noise power at each component-sensor, and $\mathbf{I}$ signifies a 2×2 identity matrix. This 2×2 matrix $\hat{\mathbf{C}}$ is Hermitian, and asymptotically approaches $\mathbf{C}$ as $M \to \infty$. The asymptotic $\hat{\mathbf{C}}$ has a principal eigenvector equal to $c\mathbf{a}$, where c is some complex-valued scalar that is algebraically independent of $\mathbf{a}$.

[2] If $\Delta_\varepsilon = 0$ (i.e. if the two sensors are collocated at one point in space), η_2 cannot be estimated in (2.10), even though η_1 may still be estimated via (2.9).

and elevation angles. Still, the extended-aperture procedure can be utilized to determine the situations with Δ_ε beyond $\lambda/2$. [33, 34, 35, 36].

From the above $\hat{\eta}_1$ and $\hat{\eta}_2$, the closed-form estimates $\hat{\theta}$ and $\hat{\phi}$ are specified in tables A.1 to A.3 of Appendix A, for $\varepsilon \neq \zeta$.

There, due to sgn (η_1) and due to the cyclic ambiguities of inverse trigonometric functions inherent in η_1 and η_2, $\hat{\theta}$ and $\hat{\phi}$ can be unambiguous for only a tetartosphere (i.e. a quarter of a sphere). For configuration (b), the necessary prior knowledge is whether $\theta \in \left[0, \frac{\pi}{2}\right)$ or $\theta \in \left[\frac{\pi}{2}, \pi\right)$ (i.e. upper vs. lower hemisphere) and whether $u > 0$ or $u < 0$ (i.e. front vs. back hemisphere). For configuration (c), the necessary prior knowledge is whether $\phi \in [0, \pi)$ or $\phi \in [\pi, 2\pi)$ (i.e. right vs. left hemisphere) and whether $u > 0$ or $u < 0$ (i.e. front vs. back hemisphere). For configuration (d), the necessary prior knowledge is whether $\theta \in \left[0, \frac{\pi}{2}\right)$ or $\theta \in \left[\frac{\pi}{2}, \pi\right)$ (i.e. upper vs. lower hemisphere) and whether $v > 0$ or $v < 0$ (i.e. right vs. left hemisphere). For configuration (f), the necessary prior knowledge is whether $\phi \in \left[-\frac{\pi}{2}, \frac{\pi}{2}\right)$ or $\phi \in \left[\frac{\pi}{2}, \frac{3\pi}{2}\right)$ (i.e. front vs. back hemisphere) and whether $v > 0$ or $v < 0$ (i.e. right vs. left hemisphere). For configuration (g), the necessary prior knowledge is whether $\phi \in [0, \pi)$ or $\phi \in [\pi, 2\pi)$ (i.e. right vs. left hemisphere) and whether $w > 0$ or $w < 0$ (i.e. upper vs. lower hemisphere). For configuration (h), the necessary prior knowledge is whether $\phi \in \left[-\frac{\pi}{2}, \frac{\pi}{2}\right)$ or $\phi \in \left[\frac{\pi}{2}, \frac{3\pi}{2}\right)$ (i.e. front vs. back hemisphere) and whether $w > 0$ or $w < 0$ (i.e. upper vs. lower hemisphere).

At $\theta = 0, \pi$, the impinging signal has none of its energy projected onto the x-y plane; hence, $\hat{\phi}$ would be impossible by any estimator.

If $\eta_1 = \eta_2$, or equivalently if $\varepsilon = \zeta$ (as in configurations (a) and (e) and (i)), the system of Equations in (2.9) and (2.10) would be indeterminable, because the

right sides of (2.9) and (2.10) would be equal, thereby offering only one constraint for two unknowns.

If the two sensors' have their locations switched: The array manifold's multiplicative factor $\left(e^{j2\pi\frac{\Delta_\epsilon}{\lambda}\eta_2}\right)$ will be absorbed into the eigen-composition c, hence poses no change to the estimation formulas there. The array manifold's complex conjugation would result simply in a sign change at the appropriate places of each estimator.

2.3 The Cramèr-Rao bound for the kth-order p-v probe in various configurations

The Cramér-Rao bound (CRB) lower-bounds the error variance obtainable from *any* unbiased estimator, given the statistical model that connects the observed data to the unknown parameter being estimated. To focus on the directivity order k and on the spatial configuration, the following analysis will use a simple statistical model for the incident signal and for the corrupting noise. This analysis could be readily extended to more complicated signal/noise scenarios.

To focus on higher-order p-v probe and its various configurations, model the incident signal as a pure-tone

$$s(t) \quad = \quad \sqrt{P_s}\; e^{j(\omega t+\varphi)}, \tag{2.11}$$

where P_s denotes the signal power and φ the initial phase, both deterministic but allowed to be unknown. Let there be additive noise, modeled as Gaussian, zero-

mean, statistically uncorrelated over time and across the two component-sensors, with an unknown power of P_n.

At the mth time instant of $t = mT_s$ (where T_s denotes the time-sampling period), the p-u probe provides a 2×1 data vector of

$$\tilde{\mathbf{z}}(mT_s) \quad = \quad \mathbf{a}\ s(mT_s) + \tilde{\mathbf{n}}(mT_s), \quad \forall m = 1, 2, \cdots, M. \tag{2.12}$$

Assumed as prior known are ω, Δ_ϵ, and λ.

This statistical data model has five real-valued scalar unknowns: θ, ϕ, P_s, P_n, φ. Hence, the resulting Fisher information matrix (FIM) is 5×5 in size. The corresponding Cramér-Rao bounds are derived (using Section 8.2.3.1 of [37]) and stated in Table B.1 of Appendix B. Therein, for example, the superscript in $\mathrm{CRB}_{\theta}^{(\mathrm{a})}(\theta, \phi)$ refers to configuration (a), whereas the subscript $_\theta$ identifies the to-be-estimated parameter whose Cramér-Rao bound is symbolized.

Figures 2.1 to 2.6 plot the Cramér-Rao bounds at various values of the sensor-order k, for the six configurations that allow bivariate azimuth-elevation direction-of-arrival estimation. The figures show that the accuracy achievable by the generalized p-v probe reduces near the infinite Cramér-Rao bounds as the order of figure-8 sensor increases. The remaining three configurations, shaded in Figure 1.4 and Table 2.1, would not allow such bivariate direction finding, for reasons already explained at the end of Section 2.2.

2.3.1 Inter-relationships among various configurations' Cramér-Rao bounds

Because the various configurations' array manifolds are functionally inter-related as in Equations (2.2)-(2.7), their corresponding Cramér-Rao bounds are also cor-

respondingly inter-related as follows:

$$\text{(b)} \leftrightarrow \text{(d)}: \qquad \mathrm{CRB}_{\times}^{(\mathrm{b})}(\theta,\phi) = \mathrm{CRB}_{\times}^{(\mathrm{d})}\left(\theta, \frac{\pi}{2}-\phi\right), \tag{2.13}$$

$$\text{(c)} \leftrightarrow \text{(f)}: \qquad \mathrm{CRB}_{\times}^{(\mathrm{c})}(\theta,\phi) = \mathrm{CRB}_{\times}^{(\mathrm{f})}\left(\theta, \frac{\pi}{2}-\phi\right), \tag{2.14}$$

$$\text{(g)} \leftrightarrow \text{(h)}: \qquad \mathrm{CRB}_{\times}^{(\mathrm{g})}(\theta,\phi) = \mathrm{CRB}_{\times}^{(\mathrm{h})}\left(\theta, \frac{\pi}{2}-\phi\right), \tag{2.15}$$

$$\text{(e)} \leftrightarrow \text{(a)}: \qquad \mathrm{CRB}_{\times}^{(\mathrm{e})}(\theta,\phi) = \mathrm{CRB}_{\times}^{(\mathrm{a})}\left(\theta, \frac{\pi}{2}-\phi\right), \tag{2.16}$$

with the subscript $\times \in \{\theta, \phi\}$.

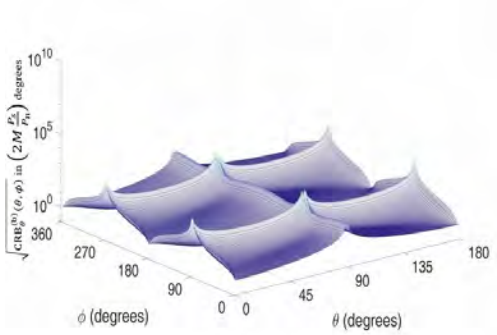

(i) $k = 1$

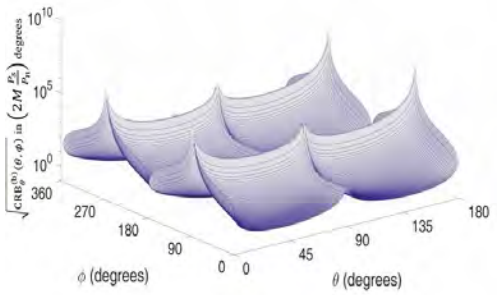

(ii) $k = 2$

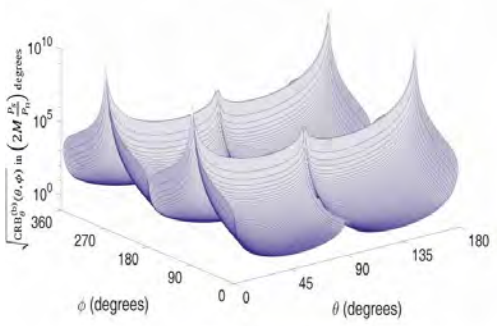

(iii) $k = 3$

Figure 2.1: Configuration (b): CRB of θ $\left[\mathrm{CRB}_{\theta}^{(\mathrm{b})}(\theta,\phi)\right]$ for various orders (k) of figure-8 sensor.

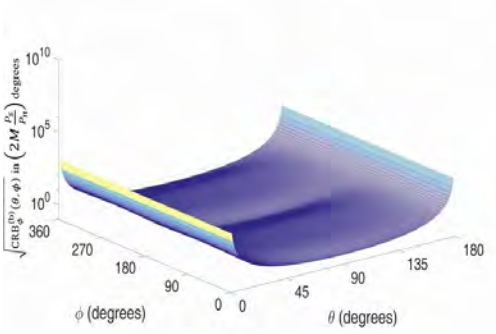

(i) $k = 1$

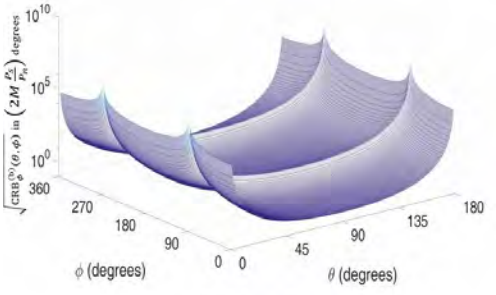

(ii) $k = 2$

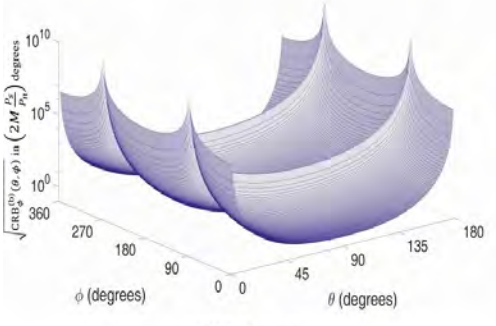

(iii) $k = 3$

Figure 2.2: Configuration (b): CRB of ϕ $\left[\mathrm{CRB}_{\phi}^{(\mathrm{b})}(\theta,\phi)\right]$ for various orders (k) of figure-8 sensor.

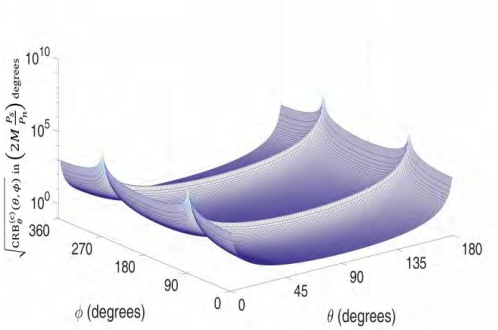

(i) $k = 1$

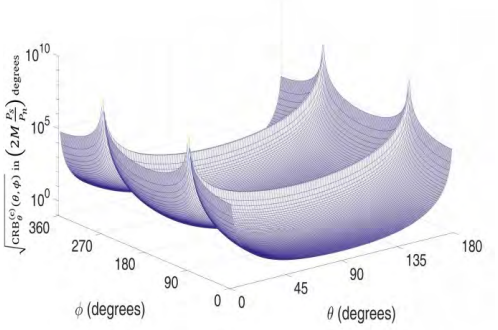

(ii) $k = 2$

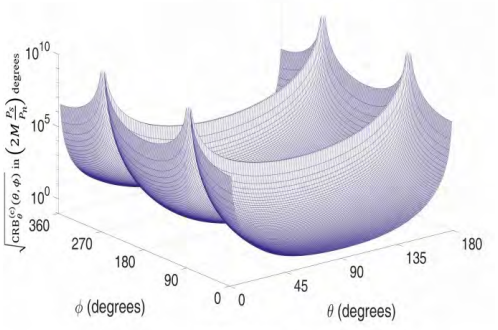

(iii) $k = 3$

Figure 2.3: Configuration (c): CRB of θ $\left[\mathrm{CRB}_{\theta}^{(\mathrm{c})}(\theta, \phi)\right]$ for various orders (k) of figure-8 sensor.

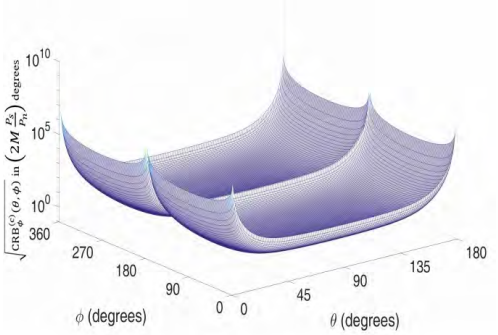

(i) $k = 1$

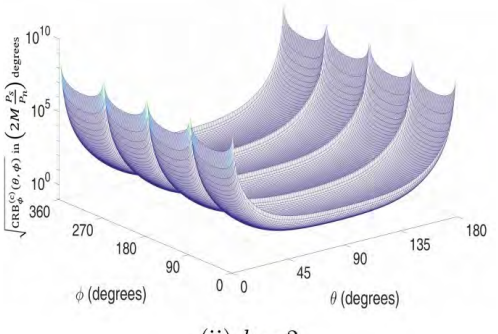

(ii) $k = 2$

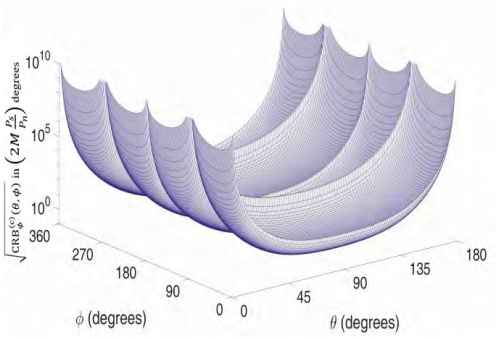

(iii) $k = 3$

Figure 2.4: Configuration (c): CRB of ϕ $\left[\mathrm{CRB}_{\phi}^{(\mathrm{c})}(\theta, \phi)\right]$ for various orders (k) of figure-8 sensor.

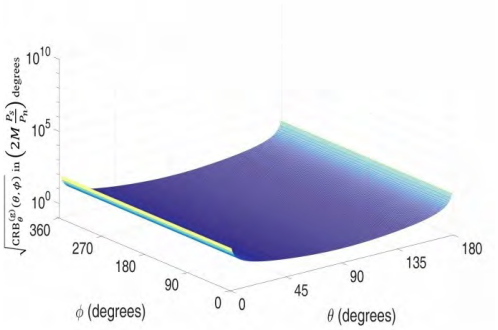

(i) $k = 1$

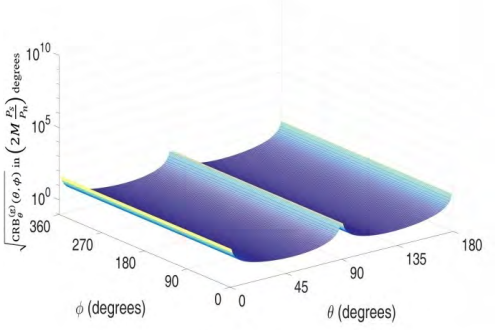

(ii) $k = 2$

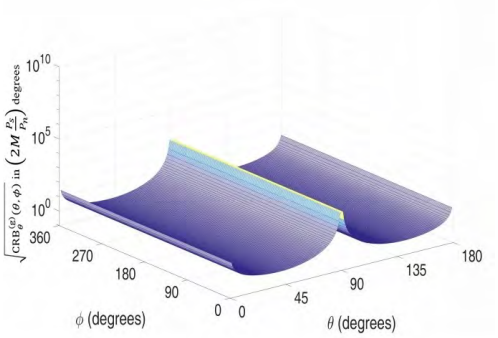

(iii) $k = 3$

Figure 2.5: Configuration (g): CRB of θ $\left[\mathrm{CRB}_{\theta}^{(\mathrm{g})}(\theta,\phi)\right]$ for various orders (k) of figure-8 sensor.

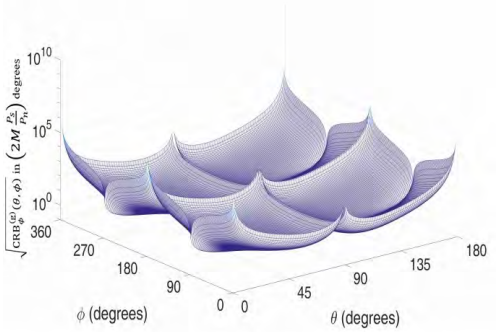

(i) $k = 1$

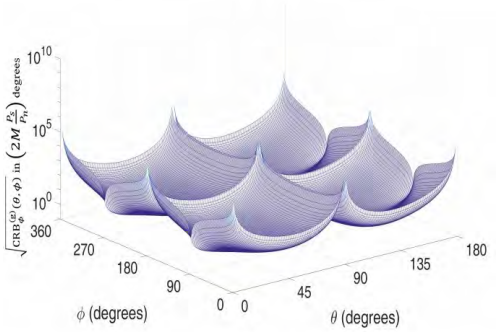

(ii) $k = 2$

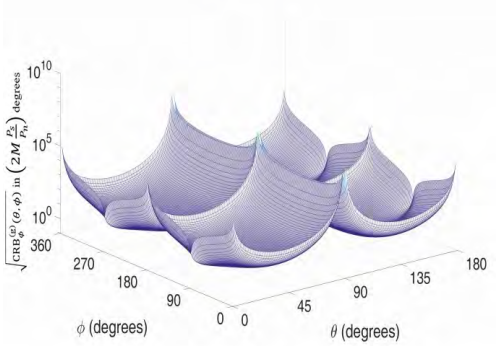

(iii) $k = 3$

Figure 2.6: Configuration (g): CRB of ϕ $\left[\mathrm{CRB}_{\phi}^{(\mathrm{g})}(\theta,\phi)\right]$ for various orders (k) of figure-8 sensor.

2.3.2 Symmetries in each Cramér-Rao bound

Each Cramér-Rao bound is

(i) symmetric with respect to $\theta = 90°$ over $\theta \in [0°, 180°]$,

(ii) symmetric with respect to $\phi = 0°$ over $\phi \in [-90°, 90°]$,

(iii) symmetric with respect to $\phi = 90°$ over $\phi \in [0°, 180°]$,

(iv) symmetric with respect to $\phi = 180°$ over $\phi \in [90°, 270°]$, and

(v) symmetric with respect to $\phi = 270°$ over $\phi \in [180°, 360°]$.

These symmetries arise mathematically in every Cramér-Rao bound expression due to the even powers to which the trigonometric functions are raised. Physically speaking, these symmetries exist because the figure-8 sensor's gain response (a) has a longitudinal cross-section that is 360° rotationally invariant with regard to the figure-8 sensor's axis, and (b) has two lobes that are left/right symmetric to each other. Please see Figure 2.7.

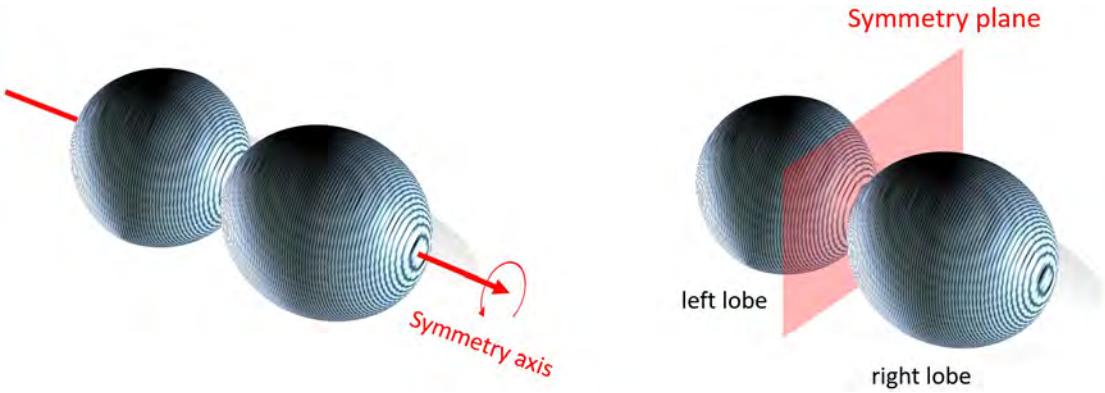

Figure 2.7: Symmetries in the figure-8 sensor's gain response.

2.3.3 To compare across the various configurations in Figure 1.4 and Table 2.1

To compare across various configurations by their direction-finding precision: Figures 2.8-2.10 plot the Cramér-Rao bound's cumulative histogram, which reveals the percentage of all possible incident direction-of-arrival from the two-dimensional support region of $\{\theta \in [0, \pi]\} \cup \{\phi \in [0, 2\pi)\}$, at which the corresponding configuration can estimate better than or equal to the precision specified by the abscissa. Figure 2.8 is for sensor-order $k = 1$, Figure 2.9 for $k = 2$, and Figure 2.10 for $k = 3$. Each figure compares all 6 configurations (i.e. all those that allow bivariate direction finding); nonetheless, the identities in (2.13)-(2.15) imply only 3 *distinct* cumulative histogram curves for each of Figures 2.8-2.10. These cumulative histograms are computed here using spatially uniform sampling over the unit-sphere's surface $\forall(\theta, \phi)$, i.e. a equal number of uniformly spaced samples per any unit area on the unit-sphere's surface. [38] The number of spatial samples equals 1.5 million over the spherical surface. Recall that the Cramér-Rao bound represents the hypothetically best precision obtainable in estimating the direction-of-arrival: the smaller the Cramér-Rao bound the better, hence the higher the cumulative histogram the better.

Some qualitative observations on $\mathrm{CRB}_\theta^{(\cdot)}(\theta, \phi)$:

1) Configurations (b) and (d)'s $\mathrm{CRB}_\theta^{(\mathrm{b})}(\theta, \phi) = \mathrm{CRB}_\theta^{(\mathrm{d})}(\theta, \phi)$ are worse than the other configurations' $\mathrm{CRB}_\theta^{(\cdot)}(\theta, \phi)$. This is intuitively reasonable, because these 2 configurations

   (i) *orient* the figure-8 directional sensor to yield *no* θ-directivity, and

   (ii) *space* the two component-sensors to yield *no* vertical aperture.

2) Configurations (g)'s and (h)'s cumulative histogram is crossed over by that of configurations (c) and (f), as the abscissa gets sufficiently large. Moreover, this cross-over abscissa drops, as the directivity order k increases. The explanation is as follows: Configurations (c) and (f) provide an inter-sensor spatial aperture along the vertical, but no vertical directivity exists in its figure-8 sensor. In contrast, configurations (g) and (h) offer vertical directivity but no vertical aperture. Figures 2.8-2.10 indicate that a $\frac{\lambda}{2}$ vertical aperture is more important than the vertical directivity, to attain a very low Cramér-Rao bound for selected (θ, ϕ) sectors. However, this advantage diminishes, as the directivity order k increases, when configurations (c) and (f) become decisively better than configurations (g) and (h). Configurations (c) and (f) provide a horizontal directivity, but *no* horizontal aperture. In contrast, configurations (g) and (h) offer *no* horizontal directivity but a horizontal aperture. As discussed above, the figure-8 sensor directivity is more important to attain the lowest Cramér-Rao bound for selected (θ, ϕ) sectors. A sufficiently high k could dominate any lack of aperture.

Some qualitative observations on $\mathrm{CRB}_{\phi}^{(\cdot)}(\theta, \phi)$:

3) For $\mathrm{CRB}_{\phi}^{(\cdot)}(\theta, \phi)$, configurations (b) and (d) are better than the other configurations. This is also intuitively reasonable, because these two configurations

   (i) *orient* the figure-8 directional sensor to maximize ϕ-directivity, as well as

   (ii) *space* the two component-sensors to give maximum *horizontal* inter-sensor aperture.

4) Configurations (g) and (h)'s cumulative histogram crosses over that of configurations (c) and (f), as the abscissa gets sufficiently large. Moreover, this cross-over abscissa drops, as the directivity order k increases. The explanation is exactly same as that under point 2) above.

5) The Cramér-Rao bounds would be unaffected by any switch of the two component-sensors' locations.

Lastly:

6) The four-component acoustic vector-sensor (AVS), comprising a tri-axial velocity-sensor and a collocating pressure-sensor, offers better Cramér-Rao bounds, than any of the high-order p-u probes. This is unsurprising, because the acoustic vector-sensor has more component-sensors.

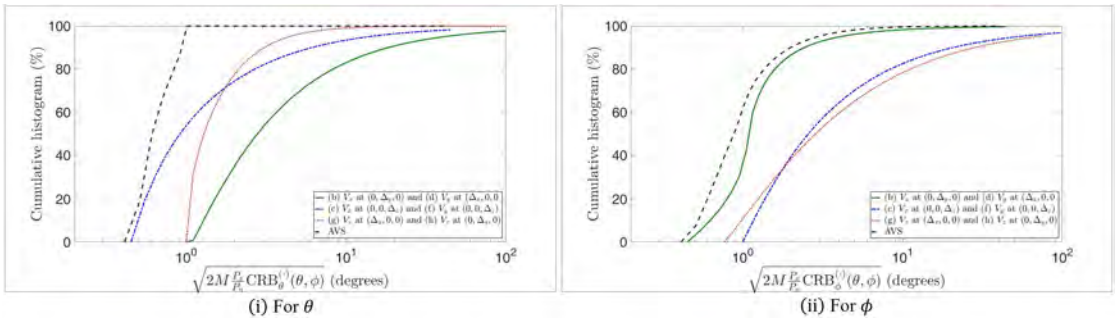

(i) For θ (ii) For ϕ

Figure 2.8: Cumulative histograms to compare the 6 configurations with the figure-8 sensor at order $k = 1$, versus the customary four-component acoustic vector-sensor (AVS).

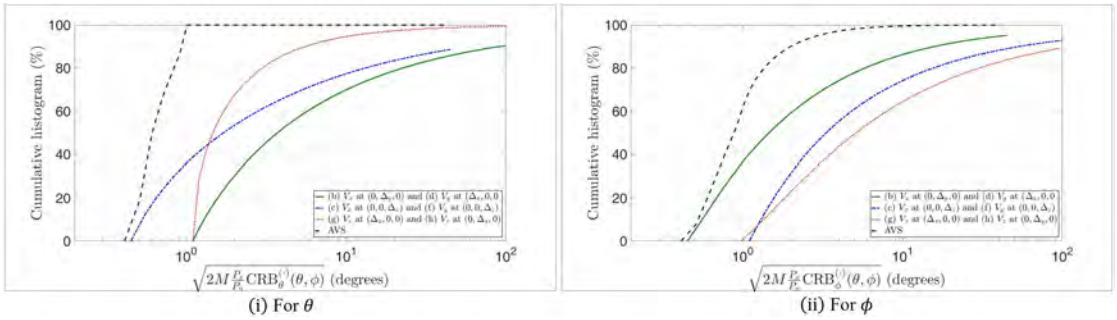

(i) For θ (ii) For ϕ

Figure 2.9: Cumulative histograms to compare the 6 configurations with the figure-8 sensor at order $k = 2$, versus the customary four-component acoustic vector-sensor (AVS).

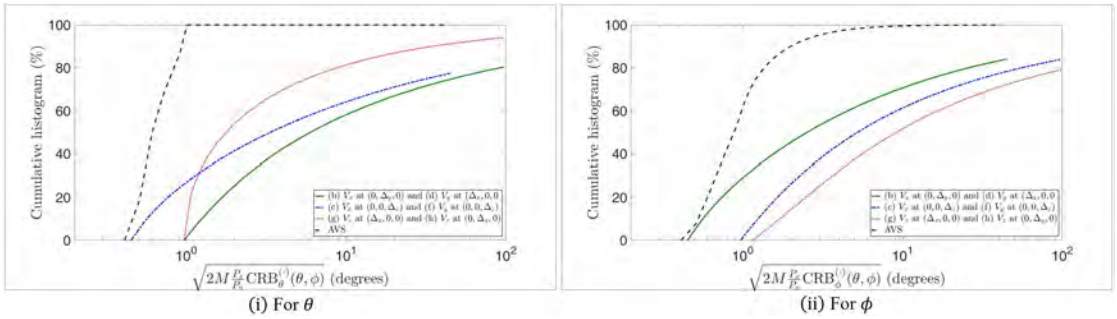

(i) For θ (ii) For ϕ

Figure 2.10: Cumulative histograms to compare the 6 configurations with the figure-8 sensor at order $k = 3$, versus the customary four-component acoustic vector-sensor (AVS).

2.4 Monte Carlo simulations of the estimators proposed in Section 2.2

This section presents Monte Carlo simulations of the estimator proposed in Section 2.2 for configuration (b), as an illustrative example. These simulations show the estimator's efficacy, with an estimation error variance very close to the Cramér-Rao bound derived in Section 2.3.

The statistical data model of Section 2.3 is retained here. Moreover, $\frac{\Delta_\epsilon}{\lambda} = \frac{1}{2}$, $\omega = 1885$ radians/second, and $\varphi = 0$.

Figures 2.11-2.14 compare configuration (b)'s estimators in the second row of Table A.1 of Appendix A, against the corresponding Cramér-Rao bounds in the second row of Table B.1 of Appendix B. Each icon on each figure represent 1000 independent Monte Carlo trials. These figures unanimously verify the proposed estimator's efficacy and closeness to the Cramér-Rao bounds. Figures 2.15-2.18 do the same for configuration (c)'s estimators in the third row of Table A.1, against the corresponding Cramér-Rao bounds in the third row of Table B.1.

Figures 2.11-2.12 and 2.15-2.16 show that the Cramér-Rao bounds decrease (i.e. improve) as the SNR increases for $k = 1, 2, 3$, as would be expected. Figures 2.13-2.14 and 2.17-2.18 show that the Cramér-Rao bounds also decrease as the inter-sensor spacing Δ_ϵ increases (and thus the array aperture is enlarged) for $k = 1, 2, 3$, as also would be expected.

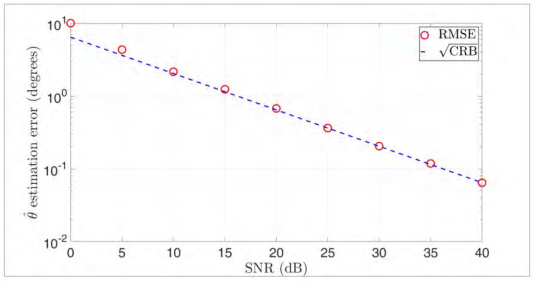

(i) $k = 1$

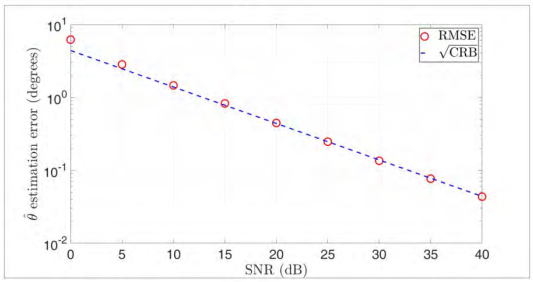

(ii) $k = 2$

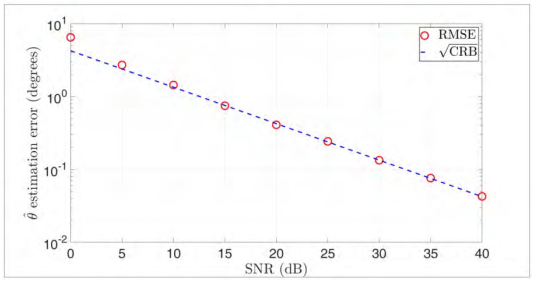

(iii) $k = 3$

Figure 2.11: Configuration (b): The proposed $\hat{\theta}$'s RMSE versus $\sqrt{\mathrm{CRB}_{\theta}^{(\mathrm{b})}(\theta, \phi)}$, at various sensor-orders k.

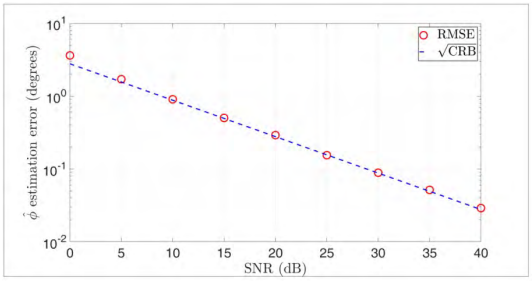

(i) $k = 1$

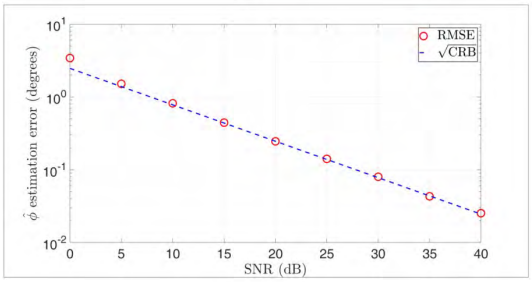

(ii) $k = 2$

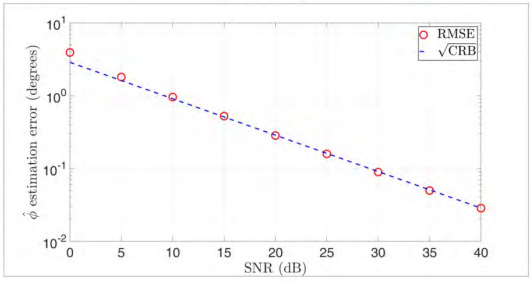

(iii) $k = 3$

Figure 2.12: Configuration (b): The proposed $\hat{\phi}$'s RMSE versus $\sqrt{\mathrm{CRB}_{\phi}^{(\mathrm{b})}(\theta, \phi)}$, at various sensor-orders k.

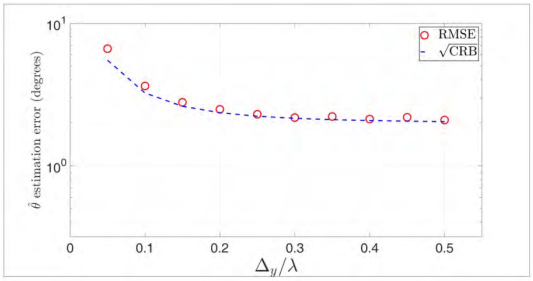

(i) $k = 1$

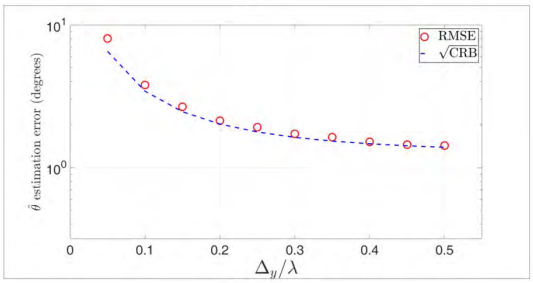

(ii) $k = 2$

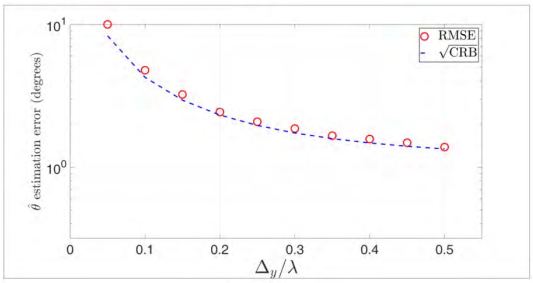

(iii) $k = 3$

Figure 2.13: Configuration (b): The proposed $\hat{\theta}$'s RMSE and $\sqrt{\mathrm{CRB}_{\theta}^{(\mathrm{b})}(\theta,\phi)}$ versus sensor's separation Δ_y/λ, at various sensor-orders k.

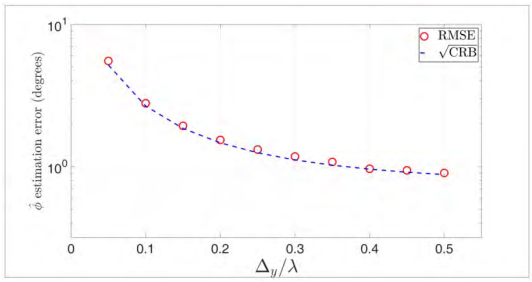

(i) $k = 1$

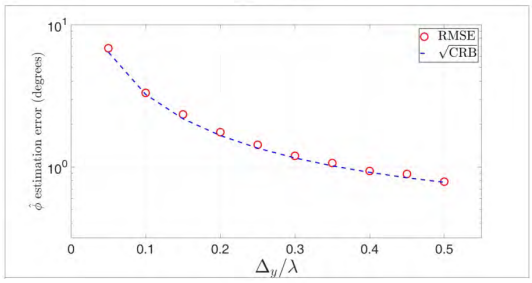

(ii) $k = 2$

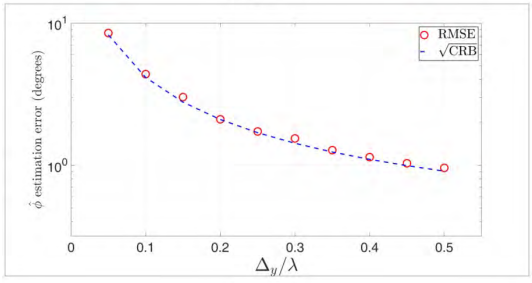

(iii) $k = 3$

Figure 2.14: Configuration (b): The proposed $\hat{\phi}$'s RMSE and $\sqrt{\mathrm{CRB}_{\phi}^{(\mathrm{b})}(\theta,\phi)}$ versus sensor's separation Δ_y/λ, at various sensor-orders k.

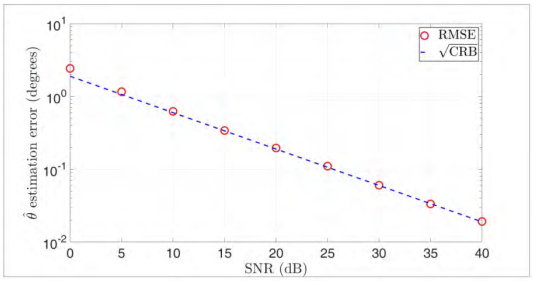

(i) $k = 1$

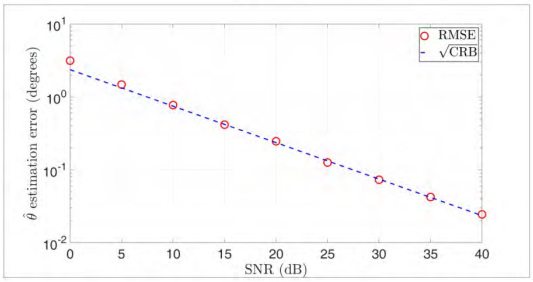

(ii) $k = 2$

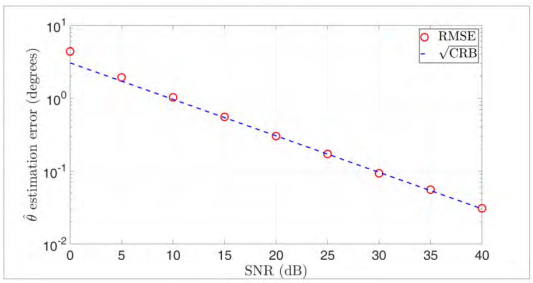

(iii) $k = 3$

Figure 2.15: Configuration (c): The proposed $\hat{\theta}$'s RMSE versus $\sqrt{\mathrm{CRB}_{\theta}^{(\mathrm{c})}(\theta, \phi)}$, at various sensor-orders k.

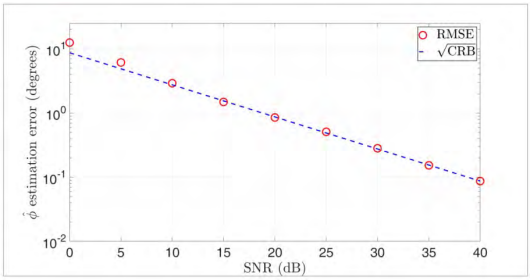

(i) $k = 1$

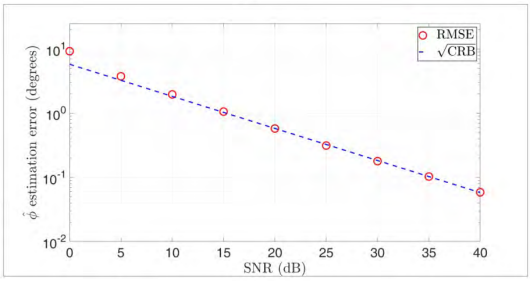

(ii) $k = 2$

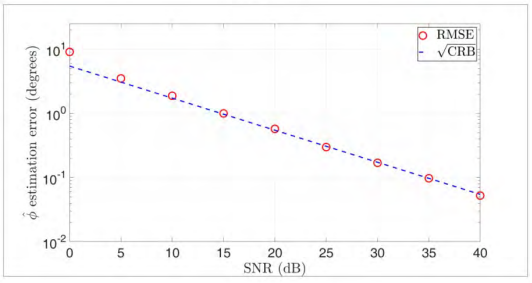

(iii) $k = 3$

Figure 2.16: Configuration (c): The proposed $\hat{\phi}$'s RMSE versus $\sqrt{\mathrm{CRB}_{\phi}^{(\mathrm{c})}(\theta, \phi)}$, at various sensor-orders k.

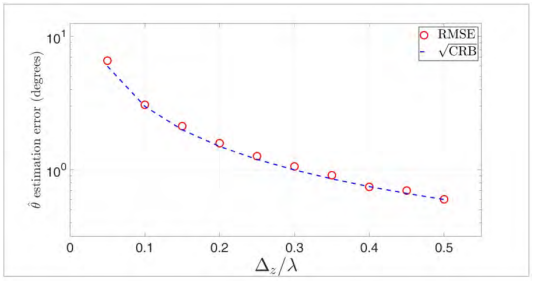

(i) $k = 1$

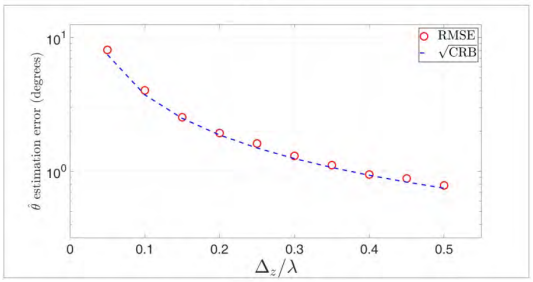

(ii) $k = 2$

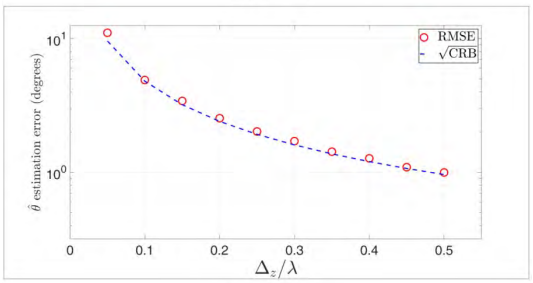

(iii) $k = 3$

Figure 2.17: Configuration (c): The proposed $\hat{\theta}$'s RMSE and $\sqrt{\mathrm{CRB}_{\theta}^{(\mathrm{c})}(\theta,\phi)}$ versus sensor's separation Δ_z/λ, at various sensor-orders k.

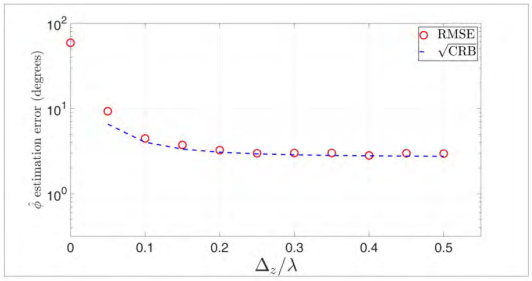

(i) $k = 1$

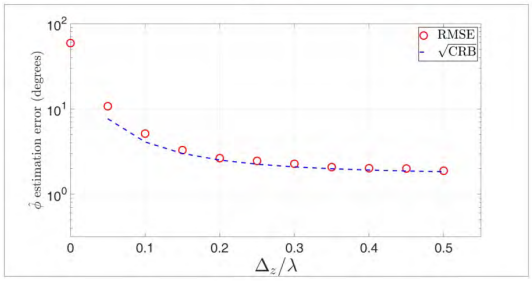

(ii) $k = 2$

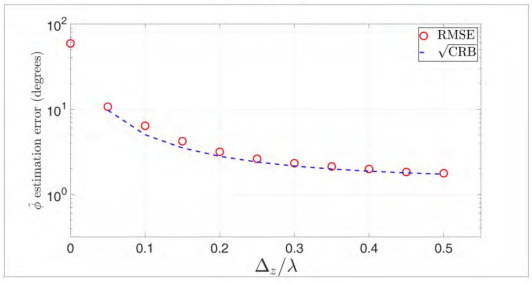

(iii) $k = 3$

Figure 2.18: Configuration (c): The proposed $\hat{\phi}$'s RMSE and $\sqrt{\mathrm{CRB}_{\phi}^{(\mathrm{c})}(\theta,\phi)}$ versus sensor's separation Δ_z/λ, at various sensor-orders k.

Part II

Leptokurtic probability density modeling of roadway sound-levels measured at a high-rise building

Part II of this thesis explores various leptokurtic probability density models for gaining new insights into the roadway sound-level distribution.

Contribution: Previous work [39, 40] indicate that roadway sound-level is leptokurtically distributed i.e. the fourth standardized moment (kurtosis) of the probability density exceeds that of a Gaussian distribution. Various leptokurtic probability densities will be tried out to fit several roadway sound-level datasets.

Part II contains three chapters:

Chapter 4 discusses the statistical background:

(i) the Jarque-Bera test to test a dataset on Gaussianity versus leptokurticity;

(ii) the candidate leptokurtic PDFs to be subsequently fit to the empirical datasets;

(iii) the goodness-of-fit assessment metric;

(iv) the statistical moments and "peakedness" (for quantifying the PDF shapes) as possible scalar metrics to predict a PDF's goodness-of-fit.

Chapter 5 discusses the empirical measurement environment and apparatus. This chapter analyzes two datasets collected at exactly the same location of a same high-rise building overlooking a roadway but on two different days, to see variability in the sound-level statistics.

Chapter 6 is analogous to Chapter 5, but now the data was collected on two different floors of the same building, to see how the sound-level statistics would vary as the roadway sound propagates up a high-rise building.

2.5 Link between Part I and Part II

Direction finding using the higher-order p-u probe (Part I) assumes white Gaussian noise. While estimating the direction-of-arrival using a sensing system like the higher-order p-u probe in a roadway noise environment, the white Gaussian noise assumption may not be appropriate because the equivalent sound pressure-level data is leptokurtic [39, 41]. As Part II of this thesis is a probabilistic modeling approach of a roadway noise environment, therefore, Part II's methodology can be used to study the distributions other than Gaussian. This may then provide a more real-world noise scenario for Monte Carlo simulations of Part I.

Part I assumes a point source that is not moving; environment with no reverberation; an impinging signal that is pure-tone and originates from the far-field. However, in Part II's real-world measurements, all these assumptions are violated. Therefore, the technique of Part I cannot readily be employed for direction finding of moving vehicles in the roadway environment of Part II.

Chapter 3

Literature review

Roadside vehicular traffic sound (or roadway sound) is a major contributor to environmental (acoustic) noises in urban areas. Roadway sounds adversely affect human health and the quality of life; those effects have been ongoing topics of research [42, 43, 44, 45, 46, 47, 48, 49, 50, 51, 52, 53, 54, 55]. Roadway sound-level has been investigated [56, 57, 42] for decades.

3.1 Significance of roadway sound-level's PDF modeling

Sound-level distribution helps to characterize its environment's "noise climate" [58, 41, 59, 60, 61] and "traffic noise index" [40, 44, 55], both of which well predict human annoyance [44, 45, 61]. Their definitions are as follows:

$$\text{noise climate} \quad = \quad L_{\text{A10},T} - L_{\text{A90},T}, \tag{3.1}$$

$$\text{traffic noise index} \quad = \quad 4\,(L_{\text{A10},T} - L_{\text{A90},T}) + L_{\text{A90},T} - 30, \tag{3.2}$$

where T is the time duration and $L_{\text{Ap},T}$ is the $(1-p)$th percentile of A-weighted sound pressure level data averaged over T. As both noise climate and traffic noise index are the function of percentile levels of A-weighted sound pressure level and as the percentile levels are different for different probability density functions, therefore, finding a more appropriate probability density function would help in better estimating the noise climate and traffic noise index. The leptokurtic distributions are more "peaked" near the center as compared to the Gaussian distribution. This means that both the noise climate and traffic noise index would be estimated higher than its actual value if Gaussian distribution is used. For the details about the A-weighted sound pressure level, please see Section 4.1.

[62] mentions the use of roadway sound-level models by

- highway engineers, to verify if their plans would stay within the permitted ceilings of traffic noise, and whether/what noise-abatement strategies would be needed.

- architectural acousticians, in designing buildings and offices next to major highways, in order to make them more habitable and conducive to work.

- acoustic specialists, to specify government policies for environmental noise reduction and regulations. These include developing noise maps and action plans.

3.2 Roadway sounds measured at a high-rise building

High-rise buildings (commercial or residential) are ubiquitous in the world's metropolises, especially those in East Asia. There, roads are urban canyons, boxed in on both sides by cement cliffs, which are formed by the walls of high-rise buildings. As the roadside sounds reverberate up these cement cliffs, the sound levels change.

Many studies have been conducted on roadway sound data measured at a high-rise building. For example,

(a) [55] measures roadway sound-level data at 24 independent high-rise buildings in Hong Kong, each for more than 24 hours. [55] then finds that arbitrarily chosen 30-minute period suffice to characterize the noise climate in the "evening" time (19:00 – 21:00) within +/-3 dB, for 85% of the cases.

(b) [63] profiles the roadway sound vertically along the height of a high-rise building. The sound energy is reported to increase from ground level up to the 9th floor and then to monotonically decrease.

(c) [61] conducts more than 270 roadway sound-level measurements from various high-rise buildings in Hong Kong, and concludes that the "intensity ratio" (Equation (1) of [64]) of roadway sound follows a "log–tanh" distribution.

(d) Other studies are [46, 65, 66, 67, 68, 69]. However, these studies do not model the roadway sound-level distribution.

3.3 Earlier probability distribution models

Table 3.1 surveys the open literature in empirical based modeling of roadway sound-level probability distribution. In contrast, for non-empirical models based on a priori theoretical conjectures, see Appendix C. [1] All these references together offer only the following elementary insights:

(a) [70] concludes that the PDF of L_{eq} measured at roadside "looks" Gaussian. However, this claim is not tested statistically and was only for the sound-levels occurring between the 10th percentile and 90th percentile of the (percentage) time distribution.

(b) Subsequent papers [39, 40, 71, 72, 73, 74, 75, 76] refute the above claim of Gaussianity. [39] concludes the L_{eq} to be leptokurtic i.e., the PDF's kurtosis exceeds that of Gaussian distribution.

(c) [40, 61, 71, 77, 78] use the Pearson distribution family on L_{Aeq} but these studies do not consider other leptokurtic distributions.

Hence, there has not yet been any systematic testing of leptokurtic PDFs to fit roadway sound-level data. This thesis is thus first in the open literature to comprehensively fit many leptokurtic PDFs to roadway sound-level data, to the best of the author's knowledge.

[1] Some studies measure the roadway sound as "equivalent sound pressure level" L_{eq} or "A-weighted equivalent sound pressure level" L_{Aeq}.

Table 3.1: Earlier probability distribution models of roadway sound-level.

Ref.	**Model based on what?**	**Verification by Empirical data?** [2]	**Traffic flow** [3]	**CDF or PDF?** [4]	**Comments**
[70]**	Empirical data	Yes (roadside)	Freely flowing	PDF	PDF looks Gaussian between 10th and 90th percentile.
[41]	Empirical data	Yes (roadside)	Freely flowing	PDF	No model proposed but refutes Gaussian PDF.
[40]**	Empirical data	Yes (high-rise)	Any	PDF	Used Pearson distribution family, Gaussian, extreme value, exponential, rectangular, logistic, Laplace, gamma, inverse-Gaussian, Poisson, Weibull.
[61]	Empirical data	Yes (high-rise)	Any	Both	Used Log-tanh, Weibull, Pearson type-III of sound intensity ratio.
[77]**	Empirical data	Yes (high-rise)	Any	PDF	Used Pearson family.
[78]**	Empirical data	Yes (high-rise)	Any	PDF	Used Pearson family.
[71]**	Empirical data	Yes (high-rise)	Any	PDF	Used Pearson family.

* used time-equivalent sound pressure level data L_{eq}.

** used A-weighted time-equivalent sound pressure level data L_{Aeq}.

For the definitions of L_{eq} and L_{Aeq}, please see Section 4.1.

[2] If a study presents empirical data to support its model, the column titled 'Verification by Empirical data?' would so indicate while specifying the location of the microphone (whether the microphone was placed on roadside or up a high-rise building outside its façade).

[3] The column titled 'Traffic flow' describes whether free- or interrupted-flow of vehicles (categorized in [40]) is observed due to the traffic conditions such as traffic signals, traffic jam, etc.

[4] The column titled 'CDF or PDF?' mentions if the respective papers use the Cumulative Distribution Function (CDF) or Probability Density Function (PDF) or both.

Chapter 4

Various statistical tests to subsequently analyze the empirical data

This chapter is organized as follows:

Section 4.1 will explain the acoustic unit representing the sound-level. Section 4.2 will explain the Jarque–Bera test to verify the conclusion of earlier papers that the probability distribution of roadway sound-level is non-Gaussian. Section 4.3 will list leptokurtic PDFs to be used in subsequent chapters to model empirical data. Section 4.4 will specify the statistical metrics to assess any PDF model's goodness-of-fit. Section 4.5 will explore whether the statistical moment or "peakedness" could predict any PDF model's goodness-of-fit.

4.1 Data metric

The data metric is in terms of the T-equivalent A-weighted sound pressure level $L_{\text{Aeq},T}$ [1], where T is the time period of one data sample and is set to one second.

The $L_{\text{Aeq},T}$ calculation from the sound pressure data has the following steps (which is done by the sound level meter):

1. For our case, the sound pressure data at the microphone is measured at a sampling frequency of 51,200 Hz.

2. Compute the spectrum of data over 1 second and divide it into one-third octave bands.

3. Compute RMS power of the 1/3 octave bands denote it as L_{RMS}. (Say, we have 30 bands, so the length of L_{RMS} vector is 30.)

4. Add A-weights to L_{RMS}. Denote it as $L_{\text{A.RMS}}$ (length of $L_{\text{A.RMS}}$ vector is 30.)

5. Logarithmically add all 30 elements of $L_{\text{A.RMS}}$, which is $L_{\text{Aeq},1s}$.

$L_{\text{Aeq},T}$ together with the noise climate [see Equation (3.1)], and the traffic noise index [see Equation (3.2)] are associated with the subjective human response to a noisy environment [44, 45, 49]. [50] suggests the use of $L_{\text{Aeq},T}$ for roadway sound-level measurements. Studies conducted in Hong Kong for roadway sound-level measurement have also used $L_{\text{Aeq},T}$ as their acoustic-noise descriptor [40, 55,

[1] Human ears do not have flat spectral response in the audible range (20Hz to 20KHz). [79] experimentally calculated the "equal-loudness contours" for the first time by applying weights to the frequency spectrum in audible range in order to quantify the subjective human response to different acoustic-noise events. Different types of weightings exist known as A-, B-, C-, and D-weighting but the most commonly employed is the A-weighting as it is commissioned by the international standard IEC 61672 for use in the sound-level meters [80].

68, 64]. Also, the environmental protection department of Hong Kong assesses the environmental (acoustic) noise in terms of $L_{\text{Aeq},T}$ [81]. The unit of $L_{\text{Aeq},T}$ is decibel denoted as dB(A), where (A) is used to highlight that the data is A-weighted.

4.2 Jarque-Bera test to verify the dataset's non-Gaussianity

The Jarque-Bera test decides if a dataset follows the Gaussian distribution, by examining the data's sample skewness and sample kurtosis against the third and fourth standardized moments of Gaussian distribution.

First, define the third standardized moment also known as "Pearson's moment coefficient of skewness" or simply "skewness", for a random variable X as

$$\gamma_1 = E\left[\left(\frac{X-\mu}{\sigma}\right)^3\right], \tag{4.1}$$

where μ is the mean and σ^2 is the variance of X. Also, define the fourth standardized moment (or the "kurtosis") as

$$\gamma_2 = E\left[\left(\frac{X-\mu}{\sigma}\right)^4\right]. \tag{4.2}$$

Incidentally, $\gamma_1 = 0$ and $\gamma_2 = 3$ for the Gaussian distribution. A leptokurtic PDF has heavier tails than the Gaussian PDF i.e., the tail/s of a leptokurtic PDF with kurtosis greater than 3 decays slower than the tail/s of the Gaussian PDF with the kurtosis equal to 3.

The above γ_1 and γ_2 may be estimated from a dataset $\{x_1, x_2, \ldots, x_N\}$, via the sample skewness $\hat{\gamma_1}$ and sample kurtosis $\hat{\gamma_2}$:

$$\hat{\gamma}_1 \quad := \quad \frac{\frac{1}{N}\sum_{n=1}^{N}\left(x_n - \bar{x}\right)^3}{\left[\frac{1}{N}\sum_{n=1}^{N}\left(x_n - \bar{x}\right)^2\right]^{3/2}}, \tag{4.3}$$

$$\hat{\gamma}_2 \quad := \quad \frac{\frac{1}{N}\sum_{n=1}^{N}\left(x_n - \bar{x}\right)^4}{\left[\frac{1}{N}\sum_{n=1}^{N}\left(x_n - \bar{x}\right)^2\right]^{2}}, \tag{4.4}$$

where N denotes the total number of data samples and

$$\bar{x} = \frac{1}{N}\sum_{n=1}^{N} x_n. \tag{4.5}$$

The Jarque-Bera test measures how closely a dataset's sample skewness and sample kurtosis are to 0 and 3, respectively. [2] The Jarque-Bera test statistic is

$$JB \quad = \quad N\left(\frac{\hat{\gamma}_1^2}{6} + \frac{\left(\hat{\gamma}_2 - 3\right)^2}{24}\right). \tag{4.6}$$

The test statistic JB is asymptotically chi-squared distributed with 2 degrees-of-freedom under the assumption that the data realizes Gaussian random variable. Define $\chi^2_\alpha(2)$ to denote the $(100 \times \alpha)$ percentile of a chi-squared distribution with two degrees-of-freedom at a specified significance level of α. [3] α equals 0.05 and 0.01 for the 95% and 99% confidence levels, respectively.

[2] The Jarque-Bera test is implemented in the package *tseries* version 0.10-35 of the R software [82].

[3] $(100 \times \alpha)\,\% = 100 - \mathrm{CL}\%$, where CL stands for confidence level.

If $JB > \chi^2_\alpha(2)$, the dataset is statistically decided as non-Gaussian, with a significance level α. $\chi^2_{0.05}(2) = 5.99$; $\chi^2_{0.01}(2) = 9.21$. [4]

The "p-value" corresponding to JB is

$$p\text{-value} \quad = \quad 1 - F_{\chi^2(2)}\left(JB\right), \tag{4.7}$$

where $F_{\chi^2(2)}\left(.\right)$ is the cumulative distribution function of a chi-squared distribution with two degrees-of-freedom conditioned on the data being a Gaussian realization. [5] If p-value $< \alpha$, the data is not a Gaussian realization at the statistical significance of α. Setting α smaller (confidence level larger) means more unlikeliness to reject that the data is a realization of Gaussian random variable.

4.3 Leptokurtic probability density functions as candidate models of roadway sound-level

Many well-known PDFs have a kurtosis above 3. The common ones are given in Appendices D, E, and F.

Appendix D lists the candidate PDFs with two parameters. Appendix E lists the candidate PDFs with three parameters. Appendix F lists the candidate PDFs with four parameters. Appendix G relates the 2-parameter, 3-parameter, and 4-parameter PDFs in a diagram.

A PDF can have parameter with respect to the density's "location", "scale", and "shape".

[4] These values of $\chi^2_\alpha(2)$ are taken from the chi-squared distribution table e.g. [83, Table A.3].
[5] The p-value for a specified JB value can be seen from [83, Table A.3]. It can also be calculated in R software using the function 'pchisq' of the package 'stats' version 3.3.1 [84].

(1) "Location" refers to any shift of the density along the abscissa, thereby affecting the mean, the median, and the mode.

(2) "Scale" refers to the spread of the density affecting the variance.

(3) "Shape" refers to the density's skewness and/or density's kurtosis, thus affecting the asymmetry and/or the tailedness.

A density's any parameter could influence more than one of the above three properties of "location", "scale", and "shape". For instance, the "degrees-of-freedom" parameter of "student's t" distribution controls the spread as well as the shape.

More parameters in a PDF would increase that PDF's flexibility to fit a dataset. PDFs with only one parameter would likely be inadequate to fully model roadway sound-level, which is leptokurtic in shape, skewed, and non-zero in mean/median/mode. On the other hand, PDFs with four parameters may likely be adequate (or more than adequate) [85], as, four parameters could already control the first four statistical moments of a PDF.

Chapters 5 and 6 will conduct comprehensive comparisons among established leptokurtic PDFs of two parameters, of three parameters, or of four-parameters in terms of their goodness-of-fit to roadway sound-level datasets. Many of these PDFs belong to one or more of the following distribution families:

(A) The **Pearson distribution family** [86, 87] is used in [40, 77, 78, 71] for roadway sound-level analysis. This family has twelve specific probability distributions that are named as Pearson type I up to type XII.

(B) The **generalized hyperbolic distribution family** has "semi-heavy" tails [88]. It was first proposed for modeling wind-blown sand and has been used

in financial risk management and analysis. The special cases include generalized hyperbolic skewed student t distribution, variance gamma distribution, hyperbolic distribution, and generalized inverse Gaussian distribution.

(C) The **generalized beta distribution family** [89] includes leptokurtic PDFs of log-logistic, Fisk, Burr, and inverse Burr distributions. It has been used in modeling stock returns and the distribution of income.

(D) The **exponential generalized beta distribution family** [89] includes many leptokurtic distributions such as logistic, Gumbel, exponential distributions. It has been used to model hydrology, equity risks, and abnormal network-traffic in information technology.

(E) The **skewed generalized t distribution family** is proposed by [90] to accommodate the heavy tails and skewness in financial data. Its special cases are the generalized t distribution [91], the skewed t distribution [92], and the skewed generalized error distribution.

4.4 Metrics on various PDFs' goodness-of-fit to the datasets

To assess a PDF's goodness-of-fit to any dataset, the following procedure/metric will be used in Chapters 5–6:

1. **(Maximum likelihood estimation of the PDF parameters) [93, section 1.2.1]** Collect the parameters of a PDF $f(.)$ as entries in a vector of $\boldsymbol{\theta}$. For that particular PDF, the best-fitting value $\hat{\boldsymbol{\theta}}$ of $\boldsymbol{\theta}$ may be estimated via

maximum likelihood estimation (MLE):

$$\hat{\boldsymbol{\theta}} \quad := \quad \arg\max_{\boldsymbol{\theta}\in\Theta} \sum_{n=1}^{N} \ln\left(f\left(x_n|\boldsymbol{\theta}\right)\right). \tag{4.8}$$

2. **(Log-likelihood function)** [**93, section 1.2.2**] The goodness-of-fit of the above $\hat{\boldsymbol{\theta}}$ may be measured by the this likelihood function,

$$\mathcal{L}\left(\hat{\boldsymbol{\theta}}|\mathbf{x}\right) \quad := \quad \sum_{n=1}^{N} \ln[f(x_n|\hat{\boldsymbol{\theta}})]. \tag{4.9}$$

   The larger the above metric, the better is the fit.

3. **(Akaike information criterion (AIC))** Different PDFs have a different number (p_i) of parameters. To account for this difference in assessing the goodness-of-fit, the metric of AIC [94, 93, 95, 96, 97] modifies the log-likelihood function of (4.9) as follows:

$$\mathrm{AIC}_i \quad := \quad 2p_i - 2\,\mathcal{L}_i\left(\hat{\boldsymbol{\theta}}|\mathbf{x}\right), \tag{4.10}$$

   PDF with more number of parameters is penalized by AIC. The smaller the AIC; the better is the ith PDF's fitting.

4. **(AIC difference)** [**93, section 2.6**] To focus on the difference in the goodness-of-fit among competing PDFs, define the ith PDF's "AIC difference":

$$\Delta_i^{(\mathrm{AIC})} \quad := \quad \mathrm{AIC}_i - \mathrm{AIC}_{\min}, \tag{4.11}$$

where $\text{AIC}_{\min} := \min\{\text{AIC}_i, \forall i\}$. The larger $\Delta_i^{(\text{AIC})}$ is, the worst is the ith PDF's fit to the dataset under consideration.

[93] states the following rule of thumb to interpret $\Delta_i^{(\text{AIC})}$, repeated in Table 4.1.

Table 4.1: The rule of thumb interpretation of $\Delta_i^{(\text{AIC})}$ [93].

$\Delta_i^{(\text{AIC})}$	Empirical support of the ith PDF
0 – 2	Substantial
4 – 7	Noticeably less
> 10	Essentially none

5. **(Relative likelihood)** To further accentuate the various PDF's goodness-of-fit , define the "relative likelihood" [93, section 2.8], [98]:

$$\mathcal{L}^{(\text{rel})}\left(f_i|x\right) \quad \propto \quad \exp\left(-\frac{1}{2}\Delta_i^{(\text{AIC})}\right), \tag{4.12}$$

where the $\propto$ symbolizes "is proportional to". This relative likelihood lies in $[0, 1]$. The best-fitting model (corresponding to the lowest AIC value) is assigned a relative likelihood value of 1.

4.5 Moments and "peakedness" — as a PDF's "sufficient statistics" of goodness-of-fit?

Could one or two scalar metrics (instead of the entire probability density function) provide a "sufficient statistic" [6] to predict that PDF's goodness-of-fit to a dataset of roadway sound-levels?

The moments and "peakedness" each characterize the shape of a PDF. Various moments or peakedness of PDFs are each plotted against $\Delta_i^{(\mathrm{AIC})}$ (shown later in Sections 5.7, 6.6) in order to try to see if any of these PDF scalars have any quasi-monotonic relationship with the goodness-of-fit metric of $\Delta_i^{(\mathrm{AIC})}$. That is, if any of these scalars monotonically increases with $\Delta_i^{(\mathrm{AIC})}$, then that single scalar may suffice as a predictor of the PDF's goodness-of-fit. A test of monotonicity is given in Section 4.5.1. The candidate scalars are discussed below.

Statistical moments: The first (raw) moment μ is the mean of the PDF that describes its location. The mean value decreases with increasing distance of the microphone location from the roadway. The second central-moment, μ_2, is the variance. The third- and fourth central-moments are used to define the skewness (Equation (4.1)) and kurtosis (Equation (4.2)) as

$$\gamma_1 \quad = \quad \frac{\mu_3}{(\mu_2)^{3/2}}, \tag{4.13}$$

$$\gamma_2 \quad = \quad \frac{\mu_4}{(\mu_2)^2}, \tag{4.14}$$

[6] "Suffient statistic" (in statistics) refers to a statistic (say t) that is *enough* for the underlying parameter vector $\boldsymbol{\theta}$ of the dataset $\{z_1, z_2, \ldots, z_I\}$ i.e. $\Pr(\boldsymbol{z} \mid t, \theta) = \Pr(\boldsymbol{z} \mid t)$. [99]

where μ_3 = third central-moment, and μ_4 = fourth central-moment.

Skewness computes the asymmetry of a PDF while kurtosis quantifies the "tailedness" of a probability distribution. The term "excess-kurtosis" is the kurtosis minus three. Leptokurtic distribution functions have excess-kurtosis greater than zero.

Cumulants are an alternative set of measures for characterizing the shape of a probability distribution. The first cumulant is the first raw moment; the second cumulant is equal to the second central-moment; the third cumulant is equal to the third central moment; the fourth or higher cumulants are different than the fourth or higher central-moments.

"Peakedness" of a probability distribution ("frequency curve in the neighborhood of the mean" [100, 101]) is not quantified by any of the above mentioned moments or cumulants. Kurtosis does not describe peakedness of a probability distribution [100, 101, 102]. The references [101, 103, 104, 105] give a measure of peakedness of a random variable, where peakedness $\mathcal{P}$ of a random variable X at point a is defined as

$$\mathcal{P}_a(h) \quad = \quad P(|X - a| \leq h), \quad h \geq 0. \tag{4.15}$$

where a is sample mode of a dataset i.e., peakedness of each PDF is calculated at the sample mode of each dataset because unimodal histogram is peaked at the mode of dataset. If a random variable X is relatively more peaked than another

random variable Y, then the distribution function of X is also relatively more peaked than the distribution function of Y [103, 104, 105]. h can be any positive value. Here, $h = 1$ dB(A) for all PDFs.

The expressions of each PDF's moments can be found in its reference, as given in Appendices D, E, and F.

4.5.1 Monotonicity test in the scatter plots of $\Delta_i^{(\mathrm{AIC})}$ vs the PDFs' moments/peakedness

The Spearman's rank correlation coefficient [106] assesses the extent of any monotonic relationship between two variables. In this thesis, one variable is $\Delta_i^{(\mathrm{AIC})}$ and the other variable y_i is any entry of the following list:

(1) $\mu_{2_i}^{(\mathrm{params})}$ (ith PDF's variance or second central-moment),

(2) $\gamma_{1_i}^{(\mathrm{params})}$ (ith PDF's skewness or third standardized-moment),

(3) $\gamma_{e_i}^{(\mathrm{params})}$ (ith PDF's excess-kurtosis i.e. kurtosis minus three),

(4) $\mu_{3_i}^{(\mathrm{params})}$ (ith PDF's third central-moment),

(5) $\mu_{4_i}^{(\mathrm{params})}$ (ith PDF's fourth central-moment),

(6) $\kappa_{4_i}^{(\mathrm{params})}$ (ith PDF's fourth cumulant),

(7) $\mathcal{P}_i^{(\mathrm{params})}$ (ith PDF's peakedness),

(8) $|\mu_{2_i}^{(\mathrm{params})} - \hat{\mu}_2^{(\mathrm{data})}|$ (absolute deviation of ith PDF's variance from dataset's variance),

(9) $|\gamma_{1_i}^{(\text{params})} - \hat{\gamma}_1^{(\text{data})}|$ (absolute deviation of ith PDF's skewness from dataset's skewness),

(10) $|\gamma_{e_i}^{(\text{params})} - \hat{\gamma}_e^{(\text{data})}|$ (absolute deviation of ith PDF's excess-kurtosis from dataset's excess-kurtosis),

(11) $|\mu_{3_i}^{(\text{params})} - \hat{\mu}_3^{(\text{data})}|$, (absolute deviation of ith PDF's third central-moment from dataset's third central-moment),

(12) $|\mu_{4_i}^{(\text{params})} - \hat{\mu}_4^{(\text{data})}|$ (absolute deviation of ith PDF's fourth central-moment from dataset's fourth central-moment),

(13) $|\kappa_{4_i}^{(\text{params})} - \hat{\kappa}_4^{(\text{data})}|$ (absolute deviation of ith PDF's fourth cumulant from dataset's fourth cumulant),

(14) $|\mathcal{P}_i^{(\text{params})} - \hat{\mathcal{P}}^{(\text{data})}|$ (absolute deviation of ith PDF's peakedness from dataset's peakedness).

In the above list, the superscript "(params)" shows the number of parameters of PDFs and the superscript "(data)" is a dataset identifier i.e.

$$(\text{params}) \quad := \quad \begin{cases} (\text{ii}), & \text{for} \quad \text{2-parameter PDFs;} \\ (\text{iii}), & \text{for} \quad \text{3-parameter PDFs;} \\ (\text{iv}), & \text{for} \quad \text{4-parameter PDFs.} \end{cases}$$

$$(\text{data}) \quad := \quad \begin{cases} (\text{uppA}), & \text{for} \quad \text{37/F dataset (a);} \\ (\text{uppB}), & \text{for} \quad \text{37/F dataset (b);} \\ (\text{midA}), & \text{for} \quad \text{19/F dataset;} \\ (\text{midB}), & \text{for} \quad \text{25/F dataset.} \end{cases} \tag{4.16}$$

For the dataset identifiers "37/F dataset (a)" and "37/F dataset (b)", refer to Chapter 5. For the dataset identifiers "19/F dataset" and "25/F dataset", refer to Chapter 6.

The following will define the Spearman's rank correlation coefficient $\hat{\rho}_{\Delta,y}$ between $\{\Delta_i^{(\mathrm{AIC})}, \forall\ i = 1, 2, \cdots, I\}$ and $\{y_i, \forall\ i = 1, 2, \cdots, I\}$. Suppose there are altogether I candidate PDFs. Order the entries in $\{\Delta_i^{(\mathrm{AIC})}, \forall\ i = 1, 2, \cdots, I\}$ in ascending order, such that $r_i^{(\Delta)}$ represents the rank of the ith PDF. Similarly, order the entries $\{y_i, \forall\ i = 1, 2, \cdots, I\}$, such that $r_i^{(y)}$ represents the corresponding rank of the ith PDF. Define

$$d_i \quad := \quad r_i^{(\Delta)} - r_i^{(y)}. \tag{4.17}$$

Then, the Spearman's rank correlation coefficient $\rho_{\Delta,y}$ between $\{\Delta_i^{(\mathrm{AIC})}, \forall\ i = 1, 2, \cdots, I\}$ and $\{y_i, \forall\ i = 1, 2, \cdots, I\}$ is estimated as

$$\hat{\rho}_{\Delta,y} \quad := \quad 1 - \frac{6}{I(I^2-1)} \sum_{i=1}^{I} d_i^2. \tag{4.18}$$

It holds that $\hat{\rho}_{\Delta,y} \in [-1, +1]$, where $+1$ means a perfect monotonically increasing relationship, whereas -1 means a perfect monotonically decreasing relationship. A perfectly monotonically increasing relation has any two 2-dimensional coordinate values $\{x_i,\ y_i\}$ and $\{x_j,\ y_j\}$, such that $(x_i - x_j)$ and $(y_i - y_j)$ are of same sign.

The above defined $\hat{\rho}_{\Delta,y}$ may be used as follows to decide if $\{\Delta_i^{(\mathrm{AIC})}, \forall\ i = 1, 2, \cdots, I\}$ and $\{y_i, \forall\ i = 1, 2, \cdots, I\}$ have any monotonic relationship.

Define the test statistic

$$t \quad := \quad \hat{\rho}_{\Delta,y} \sqrt{\frac{I-2}{1-\left(\hat{\rho}_{\Delta,y}\right)^2}}. \tag{4.19}$$

The test statistic t, conditioned on a monotonic relationship between the two random variables, is "student's t" distributed with the degrees-of-freedom equal to $(I-2)$ [107]. Further, define

$$p\text{-value} \quad := \quad \begin{cases} 2 \; F_{(\text{student})}\left(t\right), & \text{if } t < 0; \\ 2 \; \left\{1 - F_{(\text{student})}\left(t\right)\right\}, & \text{if } t > 0. \end{cases} \tag{4.20}$$

In the above, $F_{(\text{student})}\left(.\right)$ denotes the cumulative distribution function of a student's t-distribution with $(I-2)$ degrees-of-freedom conditioned on a monotonic relationship between the two random variables. Lastly, the above p-value may be compared against a preset threshold of α:

(A) The two random variables are not monotonically related, if p-value $> \alpha$;

(B) The two random variables are monotonically related, if p-value $< \alpha$.

Setting α smaller (confidence level larger) means more unlikeliness or more strictness to accept the monotonic relationship between the two random variables. The commonly used values for α are 0.01 and 0.05.

Chapter 5

How the roadway sound-level distribution varies with the day of measurement?

This chapter will analyze two datasets collected at the same location on the same floor (the 37th-floor) of one high-rise building overlooking a highway, but on two different days. This analysis will show how much the roadway sound-level distribution could vary with the date of measurement, even if the circumstantial setting remains the same.

Section 5.1 will introduce the measurements' urban setting. Section 5.2 will describe the measurement apparatus. Section 5.3 will statistically show that the datasets are leptokurtic. Section 5.4 will fit the list of candidate PDFs of Appendices D – F to the datasets. Section 5.5 explains the interrelationships among the best-fitting 2-, 3-, and 4-parameter PDFs. Section 5.7 investigates if a single scalar could be enough to statistically predict a PDF's goodness-of-fit.

5.1 Measurement environment

The datasets were measured in the neighborhood shown in Figure 5.1. A highway, shown running left/right in Figure 5.1, is the "West Kowloon Corridor", which extends for 4.2km and is located in Hong Kong [108]. On this highway, vehicular traffic flowed freely and bidirectionally along a four-lane divided highway, elevated above surface streets, bordered on one side by high-rise residential buildings, but open on the other side. The roadway sound of West Kowloon Corridor has been found in [109] to be the major acoustic-noise source to Wing Cheong Estate.

No traffic signal existed for over 1 km from the Wing Cheong Estate. Hence, no non-stationarity is caused by the intermittent traffic because a nearby traffic signal causes cyclic trend in the mean of $L_{\text{Aeq},1sec}$ data due to variation in the number of vehicles passing by the microphone.

On the 37th-floor of a 40-floor high-rise building [110] within this Wing Cheong Estate, a microphone was hanged about a meter outside the building façade, as shown in Figure 5.2. This high-rise building was 30 meters horizontally aside from the highway. The microphone was 106 meters from the elevated highway. The time windows of the measured data are reported in Table 5.1. Both days were work days, not public holidays [111, 112]. Hence, the measurements were taken during the evening rush hours. [1]

[1] More than 1 hour measurement could be enough for estimating the noise climate of "evening" time (19:00 – 21:00) [113]). For instance, [55] examines 24 datasets (more than 24-hours each) measured at various high-rise buildings and observes that more than 85% of arbitrarily chosen 30-minute contiguous datasets in "evening" time predict the overall noise climate of the "evening" time within the accuracy of +/-3 dB(A).

Table 5.1: The 37th-floor datasets' measurement windows.

Dataset	**Date**	**Weekday**	**Time of the day**	**Duration**	Sample size
37/F dataset (a)	January 19, 2015	Monday	18:29:43 - 20:29:41	1:59:58	5399
37/F dataset (b)	May 27, 2014	Tuesday	17:37:24 - 19:19:04	1:41:40	4488

5.2 Data acquisition

The measurements used a Brüel & Kjaer sound-level meter type 2250, with a type 4189 microphone, at a sensitivity of about 50 milli-Volts/Pascal. The microphone was connected to the sound-level meter with a wire extension. The loss due to the wire extension was managed by Brüel & Kjaer calibrator type 4231. The sound-level meter automatically logged the data as $L_{\text{Aeq},1sec}$ which was retrieved by Brüel & Kjaer software of 'evaluator type 7820'.

There was no rain; the wind speed was less than 5 meters/second [61], and the microphone was covered with a wind shield.

Non-vehicular loud events are manually identified and excised from the datasets. Each non-vehicular loud event contains a distinctively audible sound in audio files and that is distinctively visible on the $L_{\text{Aeq},1sec}$ time-series chart (because of the larger $L_{\text{Aeq},1sec}$ values). Such *non*-vehicular loud events include ambulance sirens, horns, someone adjusting the microphone, hammering, and other construction noises. Not excised is the *vehicular* sounds of loud trucks, cars, or motorcycles.

Figure 5.1: Google Earth's 3D-viewer snapshot, showing the measurement's physical environment and the microphone's 37th-floor location.

Figure 5.2: The microphone was positioned about one meter outside the building façade. A 1.5-meter stick provided mechanical support to the microphone, with the other end of the stick supported by a tripod. A Bruel and Kjaer windscreen covered the microphone.

5.3 Leptokurtosis in the datasets

Table 5.2 reports the Jarque-Bera test results, the sample skewness, and the sample kurtosis. Therein, the large positive JB and the small p-values conclude that the datasets are realizations of a non-Gaussian random phenomenon. The p-values of less than 2.2×10^{-16} rejects the Gaussian realization of the datasets at a confidence level above 99 %. Table 5.2 also confirms the findings of [39], which concludes that the PDF of its roadside L_{eq} data is leptokurtic and skewed.

The normalized histograms of the 37th-floor datasets are shown in Figure 5.3. The sample skewness and sample kurtosis show the data as skewed to the right with heavy tails. The right tails of both normalized histograms are heavier than

the left tails. This is due to the occasional occurrence of very loud vehicular sounds, which produce outliers in the histograms.

Table 5.2: The sample skewness $\hat{\gamma}_1$, sample kurtosis $\hat{\gamma}_2$, JB test statistic, and p-values from the Jarque-Bera test applied on the two datasets of Table 5.1.

Data	$\hat{\gamma}_1$	$\hat{\gamma}_2$	JB	p-value
37/F dataset (a)	0.85	9.22	9349	$< 2.2 \times 10^{-16}$
37/F dataset (b)	1.31	12.1	16790	$< 2.2 \times 10^{-16}$

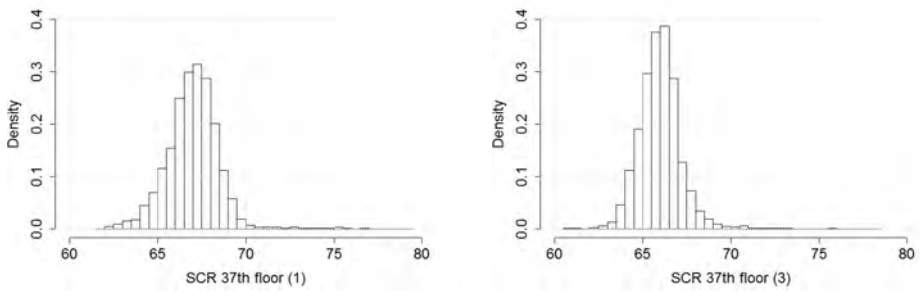

(a) 37/F dataset (a)

(b) 37/F dataset (b)

Figure 5.3: Normalized histograms of the datasets, showing a skewness unequal to zero and a kurtosis exceeding 3.

5.4 Various PDF models' goodness-of-fit

The 2-parameter PDFs (listed in Appendix D) have their $\Delta_i^{(\mathrm{AIC})}$ goodness-of-fit compared in Table 5.3. The best-fitting PDF is T2 (student's t-distribution having

two parameters i.e. degrees-of-freedom parameter (b) and location parameter (a)) with its $\Delta_i^{(\mathrm{AIC})}$ equal to zero. The PDF expression of T2 (in terms of a and b) is given in Table D.1. T2 is the only PDF with $\Delta_i^{(\mathrm{AIC})} < 2$ (see Table 4.1). T2 is symmetric and its degrees-of-freedom parameter (b) controls the kurtosis (which is $\frac{6}{b-4}$) as well as the variance (which is $\frac{1}{1-2/b}$).

Table 5.4 ranks the various 3-parameter PDFs by $\Delta_i^{(\mathrm{AIC})}$. Here, the only PDF with $\Delta_i^{(\mathrm{AIC})} < 2$ is symT3 (non-standardized student's t-distribution). symT3 is the only existing generalization of T2 in the 3-parameter PDFs with a location, a scale, and a degrees-of-freedom parameter.

Table 5.5 ranks various 4-parameter PDFs according to their $\Delta_i^{(\mathrm{AIC})}$ values. The 37/F dataset (a) is best-fit by sT4 (skewed t distribution) and the 37/F dataset (b) is best-fit by ghsT4 (generalized hyperbolic skewed student t distribution). gT4 (generalized t distribution) has $\Delta_i^{(\mathrm{AIC})} < 2$ for 37/F dataset (b), hence well-fitted (according to Table 4.1).

Table 5.3: $\Delta_i^{(\mathrm{AIC})}$ of 2-parameter PDFs fitted to the 37/F dataset (a) and 37/F dataset (b).

	37/F dataset (a)		**37/F dataset (b)**	
Goodness-of-fit rank, $r_i^{(\Delta)}$	PDF	$\Delta_i^{(\mathrm{AIC})}$	PDF	$\Delta_i^{(\mathrm{AIC})}$
1	T2	0	T2	0
2	HS	6.67	LLg	50.35
3	LLg	23.65	HS	58.79
4	Lg	35.98	Lg	76.62
5	Lp	157.82	Lp	208.77
6	IG	564.85	IG	557.19
7	nT	574.33	LN	585.81
8	LN	587.99	IGs	586.76
9	IGs	589.11	G	617.15
10	G	614.5	nT	661.37
11	Rc	673.66	Rc	683.31
12	N	673.68	N	683.32
13	LC	1239.35	Gb	987.54
14	Cy	1239.93	LC	1114.39
15	Gb	1337.17	Cy	1114.72
16	PLg	3165.33	PLg	3215.5
17	sGo	3237.64	sGo	3747.31
18	W	4084.86	W	4268.83
19	sCS	8899.52	Go	6444.92
20	L	13926.66	sCS	9030.2
21	nCS	17330.93	L	13976.75
22	Go	34565.13	nCS	16204.28

Table 5.4: $\Delta_i^{(\mathrm{AIC})}$ of 3-parameter PDFs fitted to the 37/F dataset (a) and 37/F dataset (b).

	37/F dataset (a)		**37/F dataset (b)**	
Goodness-of-fit rank, $r_i^{(\Delta)}$	PDF	$\Delta_i^{(\mathrm{AIC})}$	PDF	$\Delta_i^{(\mathrm{AIC})}$
1	symT3	0	symT3	0
2	sTK	21.8	sTK	25.73
3	gLg3	67.68	Brxii	40.74
4	Briii	72.43	gLg2	51.17
5	Dg	72.43	Briii	52.82
6	Brxii	85.19	Dg	52.82
7	sLLg	85.52	sLLg	66.67
8	gLg1	94.82	gLg1	66.72
9	gLg2	98.12	gLg3	74.12
10	gLg4	144.43	gLg4	116.12
11	XP	167.62	XG	149.42
12	sLp	202.58	XP	187.6
13	XG	300.97	sLp	221.88
14	pLg3	350.85	IG3	379.14
15	IG3	549.16	Dv	397.12
16	G3	579.71	BS	414.28
17	Dv	591.78	G3	437.44
18	sIGs	651.7	pLg3	452.29
19	BS	654.31	SN	548.68
20	F3	683.57	sIGs	608.94
21	SN	697.75	BP3	647.57
22	Rc3	736.22	GEV	690.28
23	Pii	736.34	Rc3	693.47
24	GEV	965.87	Pii	702.38
25	BP3	1003.08	sGo3	1006.32
26	W3	1206.83	sCy	1130.55
27	sCy	1263.17	W3	1552.69
28	sGo3	1399.86	Go3	4135.56
29	Go3	3613.64	F3	14757.41

Table 5.5: $\Delta_i^{(\mathrm{AIC})}$ of 4-parameter PDFs fitted to the 37/F dataset (a) and 37/F dataset (b).

	37/F dataset (a)		**37/F dataset (b)**	
Goodness-of-fit rank, $r_i^{(\Delta)}$	PDF	$\Delta_i^{(\mathrm{AIC})}$	PDF	$\Delta_i^{(\mathrm{AIC})}$
1	sT4	0	ghst4	0
2	gT4	12.29	gT4	0.72
3	Piv	15.78	gTK4	15.45
4	ghst4	27.68	sT4	21.8
5	JSu	31.79	JSu	30.82
6	gTK4	50.15	NIG	55.35
7	NIG	67.68	gBP4	63.87
8	gBP4	70.76	Piv	64.67
9	glg44	91.22	glg44	75.33
10	Hy	102.14	Hy	91.34
11	VG	126.38	VG	122.15
12	SGED	174.89	SGED	173.65
13	Pvi	580.27	Pvi	463.36
14	Pi	708.3	Pi	468.42

5.5 The best-fitting 2-, 3-, and 4-parameter PDFs are theoretically interrelated

The 2-parameter, 3-parameter, and 4-parameter PDFs with $\Delta_i^{(\mathrm{AIC})} < 2$ are related theoretically. Please see Figure 5.4. By introducing a scale parameter to T2, symT3 is obtained. Introducing skewness parameter of the generalized hyperbolic family (GH family) to symT3 [114], one gets ghsT4 (generalized hyperbolic skewed student's t-distribution). Introducing a kurtosis-controlling parameter of skewed generalized t (SGT) distribution family, symT3 is generalized to gT4 (generalized t distribution). Introducing the skewness parameter of the SGT family to symT3, one gets sT4 (skewed t distribution), which belongs to the SGT family.

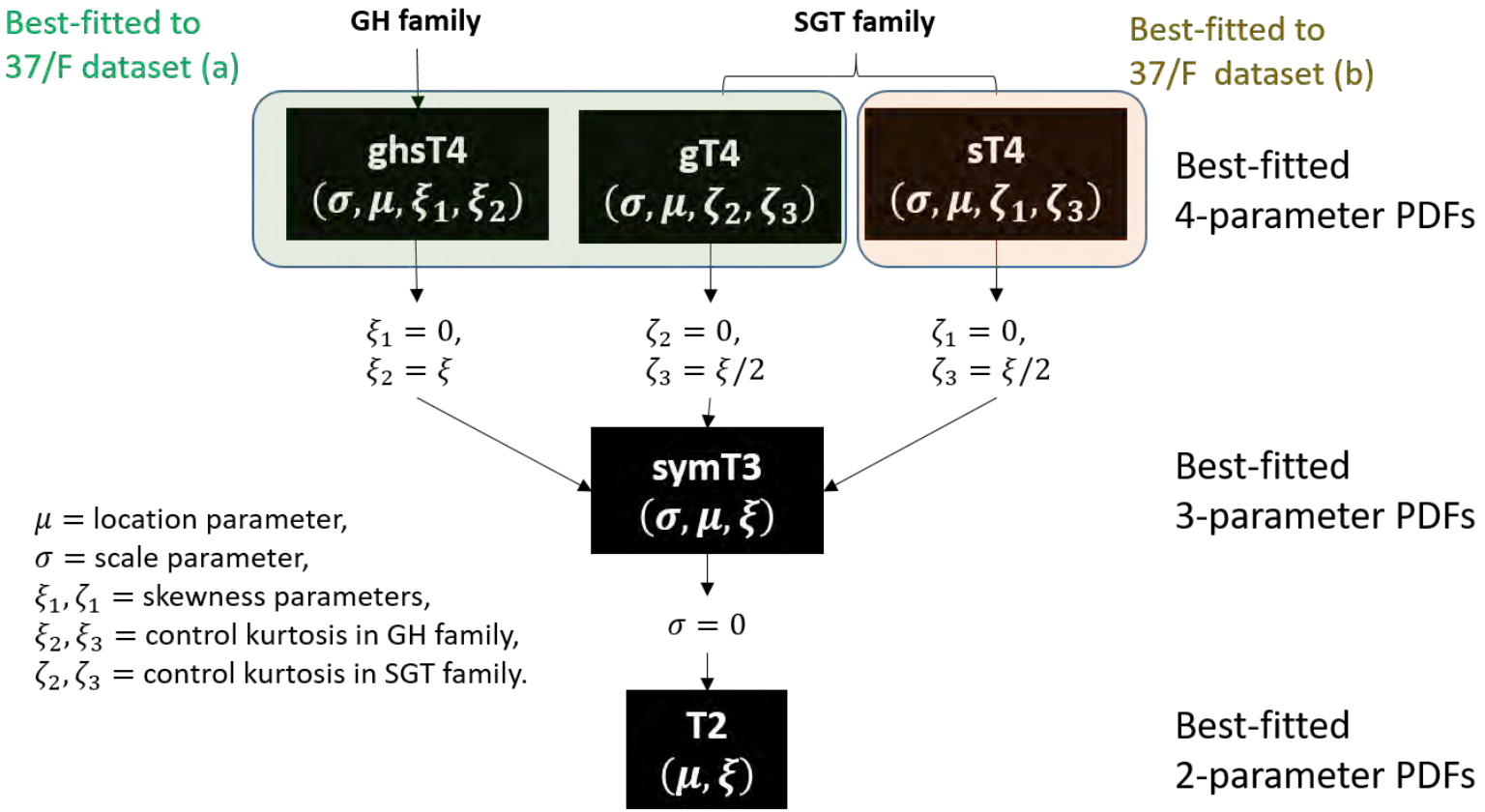

Figure 5.4: The best-fitting (according to Table 4.1) 2-, 3-, and 4-parameter PDFs to 37th-floor datasets. All generalize the standard student's t-distribution.

The 37/F dataset (b) has heavier tail on the right and higher kurtosis than the 37/F dataset (a). This is due to more occurrences of very-loud vehicular sounds in the 37/F dataset (b) than the 37/F dataset (a). ghsT4 is the only member of the GH family that has one heavy tail such that

$$f_{\text{ghsT4}} \quad \sim \quad k_1 \, |x|^{-d/2-1}, \qquad \text{when} \quad c > 0 \quad \text{and} \quad x \to +\infty, \tag{5.1}$$

and one lighter tail such that

$$f_{\text{ghsT4}} \quad \sim \quad k_1 \, |x|^{-d/2-1} \exp\left(-2 \, |c \, x|\right), \text{ when} \quad c > 0 \quad \text{and} \quad x \to -\infty, \tag{5.2}$$

where f_{ghsT4} represents the PDF of ghsT4, c is the skewness parameter, d is the kurtosis-controlling parameter, and k_1 is a constant [114, 115].

[92] introduces the skewed t distribution (sT4) of the SGT distribution family with the intention of adding a skewness parameter to symT3. sT4 indeed fits better than the generalized t distribution (gT4) of the SGT family [91] for 37/F dataset (a). However, gT4 fits the 37/F dataset (b) better than the sT4. gT4 generalizes symT3 with an extra parameter that affects the kurtosis/tailedness of symT3; hence, gT4 can model tail behaviors better than sT4 [91].

5.6 The trade-off between the goodness-of-fit and the number of parameters of PDFs

The AIC of 2-, 3-, and 4-parameter PDFs are considered together in terms of their AIC differences (Equation 4.11) in Table 5.6. Focusing on the better-fitting

PDFs, the 4-parameter PDFs rank higher than the 3-parameter PDFs; and the 3-parameter PDFs rank higher than the 2-parameter PDFs.

Table 5.6: $\Delta_i^{(\mathrm{AIC})}$ of the best-fitting PDFs from Tables 5.3, 5.4, 5.5. Despite the AIC penalty for the number of parameters, the 4-parameter PDFs' goodness-of-fit are ranked higher than the 3-parameter and 2-parameter PDFs for the 37th-floor datasets.

	37/F dataset (a)		**37/F dataset (b)**	
Goodness-of-fit rank	PDF	$\Delta_i^{(\mathrm{AIC})}$	PDF	$\Delta_i^{(\mathrm{AIC})}$
1	sT4	0	ghst4	0
2	gT4	12.29	gT4	0.72
3	Piv	15.78	gTK4	15.45
4	symT3	26.45	sT4	21.8
5	ghst4	27.68	symT3	24.24
6	JSu	31.79	JSu	30.82
7	sTK	48.26	T2	40.97
8	gTK4	50.15	sTK	49.97
9	NIG	67.68	NIG	55.35
10	gBP4	70.76	gBP4	63.87
11	T2	87.03	Piv	64.67
12	glg44	91.22	Brxii	64.98
13	HS	93.71	glg44	75.33
14	gLg3	94.14	gLg2	75.41
15	Briii	98.89	Briii	77.06
16	LLg	110.69	sLLg	90.91
17	Brxii	111.65	gLg1	90.96
18	sLLg	111.98	LLg	91.32
19	gLg1	121.27	Hy	91.34
20	Lg	123.02	gLg3	98.36

5.7 Moments and peakedness — as a PDF's sufficient statistics of goodness-of-fit?

This section investigates if a single scalar (like a moment or peakedness) instead of the entire PDF can suffice to predict a PDF's goodness-of-fit. Various PDF's scalars (listed as (1) to (14) in Section 4.5.1 and based on each candidate PDF's fitted parameter values) are plotted individually against $\Delta_i^{(\mathrm{AIC})}$ in Figures 5.5 - 5.10 and Figures H.1 - H.6. The Spearman's rank correlation coefficient assesses the monotonicity. The results of this test for 37th-floor datasets are given in Table 5.7. This table only reports the most promising candidate sufficient statistics. The scalar metrics that do not have significant monotonic trend are reported in Appendix H.

From Table 5.7, at the significance level α of 0.01,

(i) the variance and the peakedness of the 2-parameter PDFs are monotonically related to their goodness-of-fit ranks.

(ii) the 3-parameter PDFs' peakedness is monotonically related to the goodness-of-fit ranks.

(iii) the 4-parameter PDFs' excess-kurtosis is monotonically related to the goodness-of-fit ranks.

Table 5.7: $\hat{\rho}_{\Delta,y}$ and p-value of the Spearman's rank correlation significance test for 37th-floor datasets. The corresponding scatter graphs for 37/F dataset (a) are shown in Figures 5.5-5.7. The corresponding scatter graphs for 37/F dataset (b) are shown in Figures 5.8-5.10. See Section 4.5.1 for the symbols used in this table.

	Ordinate, y;	37/F dataset (a) $\hat{\rho}_{\Delta,y}$ (p-value)	37/F dataset (b) $\hat{\rho}_{\Delta,y}$ (p-value)
2-parameter PDFs	$\mu_{2_i}^{(\mathrm{ii})}$	0.701 (0.007)	0.804 (0)
	$\lvert\mu_{2_i}^{(\mathrm{ii})} - \hat{\mu}_2^{(\mathrm{data})}\rvert$	0.809 (0)	0.782 (0.001)
	$\mathcal{P}_i^{(\mathrm{ii})}$	-0.825 (0)	-0.881 (0)
	$\lvert\mathcal{P}_i^{(\mathrm{ii})} - \hat{\mathcal{P}}^{(\mathrm{data})}\rvert$	0.772 (0)	0.894 (0)
3-parameter PDFs	$\mathcal{P}_i^{(\mathrm{iii})}$	-0.727 (0)	-0.883 (0)
	$\lvert\mathcal{P}_i^{(\mathrm{iii})} - \hat{\mathcal{P}}^{(\mathrm{data})}\rvert$	0.743 (0)	0.911 (0)
4-parameter PDFs	$\gamma_{e_i}^{(\mathrm{iv})}$	-0.964 (0)	-0.855 (0.002)
	$\lvert\gamma_{e_i}^{(\mathrm{iv})} - \hat{\gamma}_e^{(\mathrm{data})}\rvert$	0.612 (0.066)	0.855 (0.002)

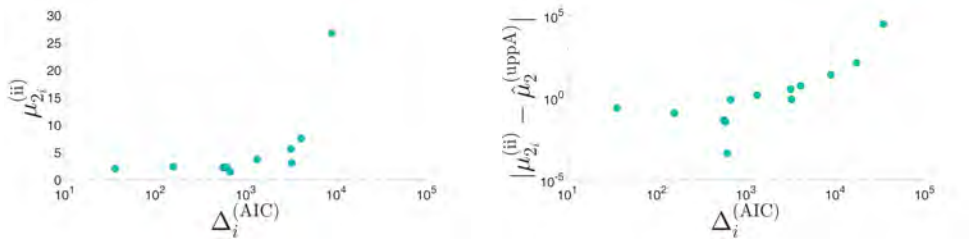

(a) $\mu_{2_i}^{(\mathrm{params})}$ (b) $|\mu_{2_i}^{(\mathrm{params})} - \hat{\mu}_2^{(\mathrm{data})}|$

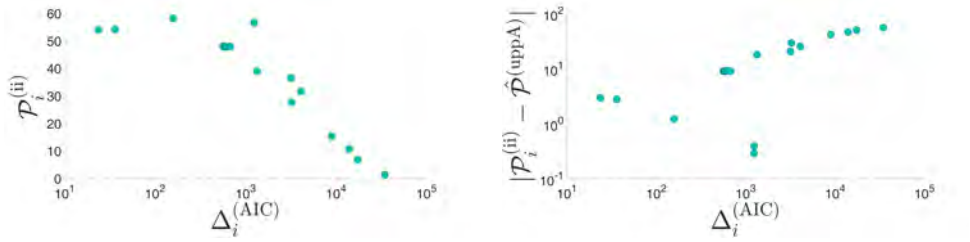

(c) $\mathcal{P}_i^{(\mathrm{params})}$ (d) $|\mathcal{P}_i^{(\mathrm{params})} - \hat{\mathcal{P}}^{(\mathrm{data})}|$

Figure 5.5: (37/F dataset (a)) The scatter plots show a monotonic trend at $\alpha = 0.01$ for the 2-parameter PDFs. Each point in the scatter plots compounds to a PDF. (a) PDFs' variance, (b) Absolute deviation of PDFs' variance from dataset's variance, (c) PDF's peakedness, (d) Absolute deviation of PDFs' peakedness from dataset's peakedness.

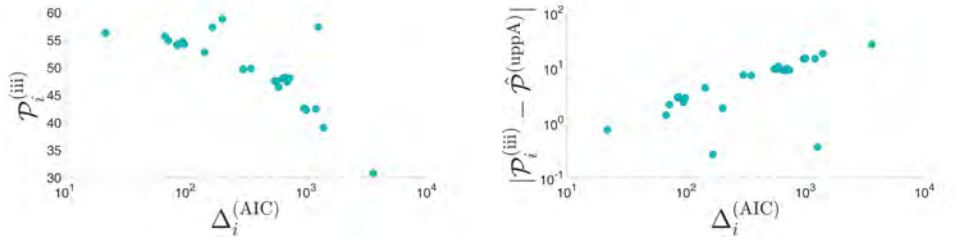

(a) $\mathcal{P}_i^{(\mathrm{params})}$ (b) $|\mathcal{P}_i^{(\mathrm{params})} - \hat{\mathcal{P}}^{(\mathrm{data})}|$

Figure 5.6: (37/F dataset (a)) The scatter plots show a monotonic trend at $\alpha = 0.01$ for the 3-parameter PDFs. Each point in the scatter plots compounds to a PDF. (a) PDF's peakedness, (b) Absolute deviation of PDFs' peakedness from dataset's peakedness.

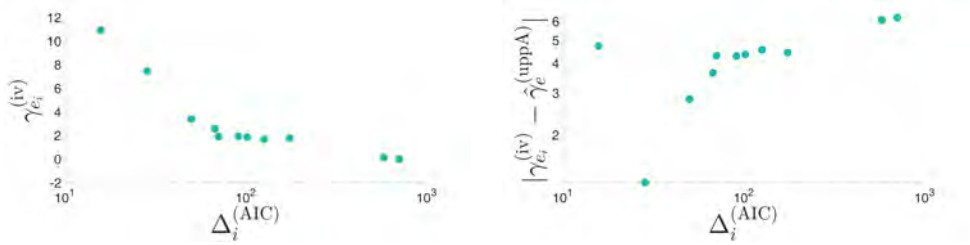

(a) $\gamma_{e_i}^{(\mathrm{params})}$ (b) $|\gamma_{e_i}^{(\mathrm{params})} - \hat{\gamma}_e^{(\mathrm{data})}|$

Figure 5.7: (37/F dataset (a)) The scatter plots show a monotonic trend at $\alpha = 0.01$ for the 4-parameter PDFs. Each point in the scatter plots compounds to a PDF. (a) PDF's excess-kurtosis, (b) Absolute deviation of PDFs' excess-kurtosis from dataset's excess-kurtosis.

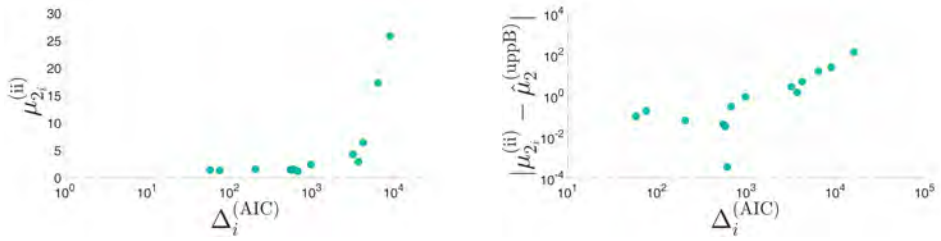

(a) $\mu_{2_i}^{(\mathrm{params})}$ (b) $|\mu_{2_i}^{(\mathrm{params})} - \hat{\mu}_2^{(\mathrm{data})}|$

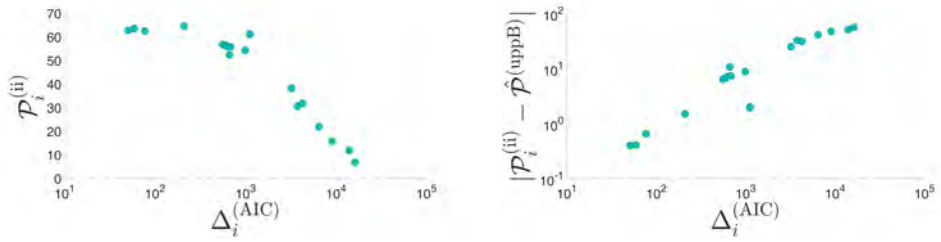

(c) $\mathcal{P}_i^{(\mathrm{params})}$ (d) $|\mathcal{P}_i^{(\mathrm{params})} - \hat{\mathcal{P}}^{(\mathrm{data})}|$

Figure 5.8: (37/F dataset (b)) The scatter plots show a monotonic trend at $\alpha = 0.01$ for the 2-parameter PDFs. (a) PDFs' variance, (b) Absolute deviation of PDFs' variance from dataset's variance, (c) PDF's peakedness, (d) Absolute deviation of PDFs' peakedness from dataset's peakedness.

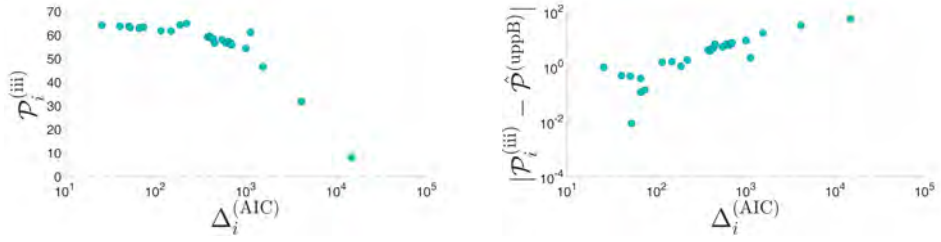

(a) $\mathcal{P}_i^{(\mathrm{params})}$ (b) $|\mathcal{P}_i^{(\mathrm{params})} - \hat{\mathcal{P}}^{(\mathrm{data})}|$

Figure 5.9: (37/F dataset (b)) The scatter plots show a monotonic trend at $\alpha = 0.01$ for the 3-parameter PDFs. (a) PDF's peakedness, (b) Absolute deviation of PDFs' peakedness from dataset's peakedness.

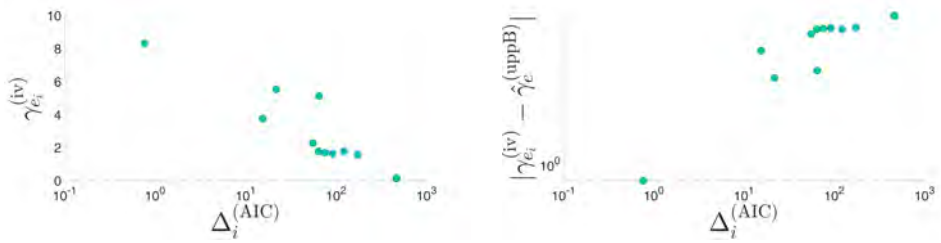

(a) $\gamma_{e_i}^{(\text{params})}$ (b) $|\gamma_{e_i}^{(\text{params})} - \hat{\gamma}_e^{(\text{data})}|$

Figure 5.10: (37/F dataset (b)) The scatter plots show a monotonic trend at $\alpha = 0.01$ for the 4-parameter PDFs. (a) PDF's excess-kurtosis, (b) Absolute deviation of PDFs' excess-kurtosis from dataset's excess-kurtosis.

Chapter 6

How the roadway sound-level distribution varies with the microphone's floor-level in the high-rise building?

This chapter will compare two datasets, collected on different floors of a same high-rise building (same as that in Chapter 5), to see how the microphone's floor level would affect the sound-level distribution.

Section 6.1 will describe the floor locations where the measurements were taken. Section 6.2 will statistically show that the datasets are leptokurtic. Section 6.3 will fit the datasets to the various PDFs in Appendices D to F. Section 6.4 analyzes the interrelationships of those 2-, 3-, and 4-parameter PDFs with best goodness-of-fit ranks. Section 6.6 investigates if a single scalar can be enough to predict the PDF's goodness-of-fit.

6.1 The floor locations

The measurement procedure and apparatus were same as described in Sections 5.1-5.2. Measurements were taken at the 19th- and 25th-floors of the same Wing Cheong Estate where Chapter 5's 37th-floor datasets were measured.

Again, the non-vehicular distinctively-heard sounds are excised (as described in Section 5.2) Table 6.1 gives the time windows of data measured at the 19th- and 25th-floor of Wing Cheong Estate. The measurements were done at rush hours. At the 19th-floor, the microphone was 57.4 meters above the roadway. At the 25th-floor, it was 73.6 meters. Please see Figure 6.1. The microphone was hanged about 1 meter outside the building façade. Note that the 19/F dataset and 37/F dataset (b) are simultaneously measured at the different vertical locations of the same high-rise building.

Table 6.1: The 19th- and 25th-floor datasets' measurement windows.

Data	**Date**	**Weekday**	**Time of the day**	**Duration**	Sample size
19/F dataset	May 27, 2014	Tuesday	18:05:31 – 19:16:20	1:10:49	4234
25/F dataset	March 28, 2014	Friday	17:51:10 – 19:26:24	1:35:14	5603

Figure 6.1: Google Earth's 3D-viewer snapshot, showing the measurement's physical environment and the microphone's 19th- and 25th-floors' location.

6.2 19/F and 25/F datasets had thinner tails than the 37th-floor datasets

Sample skewness and sample kurtosis of the datasets of 19th- and 25th-floors are given in Table 6.2, along with the Jarque-Bera test results. The test statistic JB concludes (with a confidence level of 99%) that the dataset is not a realization of Gaussian random entity. The data is slightly skewed to the left and the tails of the normalized histograms are heavier than that of the Gaussian distribution, but less heavily than the 37th-floor datasets. The normalized histograms of both the 19th- and 25th-floors datasets are shown in Figure 6.2. This confirms the findings of [39], which concludes that the PDF of its roadside L_{eq} data is leptokurtic and skewed.

Table 6.2: The sample skewness $\hat{\gamma}_1$, sample kurtosis $\hat{\gamma}_2$, JB test statistic, and p-values from the Jarque-Bera test applied on the two datasets of Table 6.1.

Data	$\hat{\gamma}_1$	$\hat{\gamma}_2$	JB	p-value
19/F dataset	-0.39	4.75	645.35	$< 2.2 \times 10^{-16}$
25/F dataset	-0.13	4.9	858.84	$< 2.2 \times 10^{-16}$

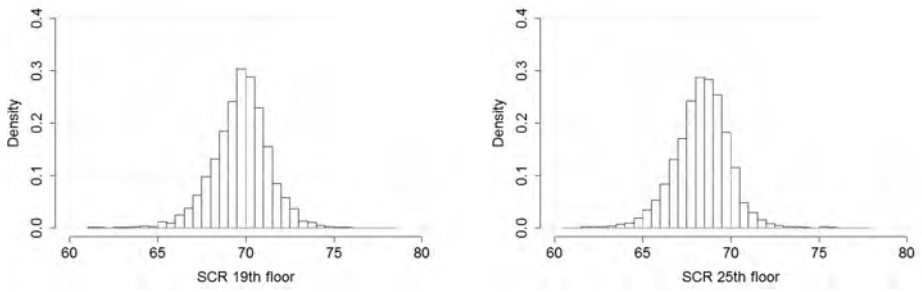

(a) 19/F dataset (b) 25/F dataset

Figure 6.2: Normalized histograms of 19th-floor and 25th-floor datasets, with skewness unequal to zero and kurtosis exceeding 3.

6.3 Ranking of PDFs by $\Delta_i^{(\mathrm{AIC})}$ for the 19/F and 25/F datasets

The 2-parameter, 3-parameter, and 4-parameter PDFs are fitted to the 19/F and 25/F datasets and are ranked by their increasing $\Delta_i^{(\mathrm{AIC})}$.

Table 6.3 reports the 2-parameter PDFs sorted according to increasing $\Delta_i^{(\mathrm{AIC})}$ values. Lg (logistic distribution a.k.a. sech-squared distribution ('sech' stands for secant-hyperbolic)) is the best-fitting PDF for both the 19th- and the 25th-floor datasets. Lg and HS (hyperbolic secant distribution) are the best-fitting PDFs for both datasets. LLg (log-logistic distribution) is the third best-fitting PDF among the 2-parameter PDFs. If a random variable X is distributed as $\mathrm{Lg}(a, b)$, then the random variable $Y = \exp(X)$ is distributed as $\mathrm{LLg}(e^a, 1/b)$.

Table 6.3: $\Delta_i^{(\mathrm{AIC})}$ of 2-parameter PDFs fitted to the 19th- and 25th-floor datasets.

	19/F dataset		**25/F dataset**	
Goodness-of-fit rank, $r_i^{(\Delta)}$	PDF	$\Delta_i^{(\mathrm{AIC})}$	PDF	$\Delta_i^{(\mathrm{AIC})}$
1	Lg	0	Lg	0
2	HS	2.32	HS	17.91
3	LLg	22.13	LLg	19.78
4	Lp	110.9	Lp	211.62
5	N	191.65	T2	236.44
6	Rc	191.66	N	265.64
7	T2	192.18	Rc	265.64
8	G	220.34	G	281.89
9	LN	236.28	LN	292.34
10	IGs	236.66	IGs	292.81
11	nT	245.78	nT	296.62
12	IG	253.74	IG	304.7
13	PLg	610.98	PLg	1312.42
14	W	763.43	LC	1477.45
15	LC	1056.43	Cy	1478.1
16	Cy	1056.91	W	1683.47
17	Gb	1850.21	Gb	1999.77
18	Go	2638.92	sGo	3175.39
19	sGo	3074.11	Go	4506.5
20	sCS	6547.94	sCS	8679.82
21	nCS	12974.84	nCS	17298.37
22	L	14543.73	L	18133.26

Table 6.4 ranks the 3-parameter PDFs. Briii (inverse Burr or Dagum distribution) is the best-fitting PDF, followed by gLg1 (skew-logistic distribution) for both the 19/F and the 25/F datasets. Briii covers wider range of skewness and kurtosis values than Brxii (Burr or Singh-Maddala distribution) [116, 117].

Table 6.5 ranks the 4-parameter PDFs. For the 19/F dataset, the fitted PDFs with $\Delta_i^{(\mathrm{AIC})} < 2$ are VG (variance gamma distribution), Hy (hyperbolic distribution), gBP4 (generalized beta prime distribution), glg44 (exponential generalized beta of the second type), and NIG (normal inverse Gaussian distribution). And sT4 (skewed t distribution) has $\Delta_i^{(\mathrm{AIC})} = 3.24$. sT4 is the only 4-parameter PDF with $\Delta_i^{(\mathrm{AIC})} < 2$ for the 25/F dataset.

Table 6.4: $\Delta_i^{(\mathrm{AIC})}$ of 3-parameter PDFs fitted to the 19th- and 25th-floor datasets.

	19/F dataset		**25/F dataset**	
Goodness-of-fit rank, $r_i^{(\Delta)}$	PDF	$\Delta_i^{(\mathrm{AIC})}$	PDF	$\Delta_i^{(\mathrm{AIC})}$
1	Briii	0	Briii	0
2	gLg1	0.26	gLg1	5.08
3	gLg2	9.72	Brxii	15.14
4	gLg4	11.83	gLg2	15.26
5	Brxii	13.08	gLg4	22.43
6	sTK	36.96	symT3	30.55
7	gLg3	37.86	sTK	35.88
8	symT3	38.21	gLg3	39.54
9	XP	51.2	sLLg	64.53
10	sLLg	67.32	XP	82.53
11	sLp	114.7	sLp	209.46
12	pLg3	160.27	pLg3	225.25
13	SN	182.55	XG	282.96
14	XG	234.36	SN	283.78
15	Pii	234.37	Rc3	307.79
16	Rc3	234.38	Pii	307.88
17	BS	246.82	BS	314.96
18	G3	258.55	IG3	336.81
19	IG3	269.43	F3	339.43
20	sIGs	281.45	sIGs	339.74
21	W3	344.9	G3	413.69
22	Dv	686.26	W3	629.36
23	GEV	719.35	Dv	708.78
24	Go3	909.65	GEV	926.14
25	sCy	1067.44	sCy	1476.67
26	BP3	1675.37	BP3	1633.07
27	sGo3	1892.95	Go3	1883.87
28	F3	15979.64	sGo3	2042.13

Table 6.5: $\Delta_i^{(\mathrm{AIC})}$ of 4-parameter PDFs fitted to the 19th- and 25th-floor datasets.

	19/F dataset		**25/F dataset**	
Goodness-of-fit rank, $r_i^{(\Delta)}$	PDF	$\Delta_i^{(\mathrm{AIC})}$	PDF	$\Delta_i^{(\mathrm{AIC})}$
1	VG	0	sT4	0
2	Hy	0.01	Piv	10.87
3	gBP4	0.9	JSu	10.93
4	glg44	1.08	gBP4	14.09
5	NIG	1.27	NIG	18.41
6	JSu	2.43	glg44	19.05
7	sT4	3.24	ghst4	20.25
8	Piv	5.18	Hy	21.62
9	gTK4	6.6	VG	28.28
10	ghst4	7.46	gTK4	32.35
11	SGED	7.78	gT4	42.73
12	gT4	37.69	SGED	57.29
13	Pvi	254.5	Pvi	337.79
14	Pi	611.27	Pi	6330.2

6.4 Theoretical interrelationship of the best-fitting 2-, 3-, and 4-parameter PDFs

This section theoretically interrelates the best-fitting 2-parameter, 3-parameter, and 4-parameter PDFs. Please see Figure 6.3. Therein, Lg (logistic distribution)

can be generalized to gLg1 (skewed logistic distribution) by an additional shape parameter that controls the skewness and kurtosis together [118]. Briii (inverse Burr distribution) covers the Lg's point on skewness-kurtosis plot [116]; [1] so, Lg's skewness and kurtosis can also be modeled by Briii by adjusting the Briii's one scale and two shape parameters. Briii is a limiting case of gBP4 (generalized beta prime distribution) and is obtained by evaluating the shape parameter of gBP4 (i.e. ς_3) to one. gLg1 can be generalized to gLg44 (generalized logisitic distribution type IV a.k.a. exponential generalized beta of the second kind) by introducing the shape parameter δ_2 of the exponential generalized beta (EGB) distribution family.

Among the three shape parameters of the GH family (Figure 6.3), one is the skewness parameter and the other two control the kurtosis. The SGT family also has one skewness parameter and two kurtosis controlling parameters. The GB family has three classes: the generalized beta of first kind (GB1), the generalized beta of second kind (also called the generalized beta prime distribution – gBP4), and the beta (B) distribution. Beta distribution is also called the Pearson type I distribution, which is in the list of 4-parameter PDFs, but is not a good fit to the datasets. The special cases of gBP4 (i.e. Briii, LLg, Brxii, etc.) have better goodness-of-fit ranks than the special cases of GB1 and B (i.e. non-central chi-squared distribution, log normal distribution, gamma distribution). The exponential generalized beta (EGB) distribution family has two special distributions: generalized exponentials (EGB1) and generalized logistics (EGB2) **??**. The generalized logistics have higher goodness-of-fit ranks.

[1] The skewness-kurtosis plot [117] is a plot of squared-skewness vs kurtosis. This plot visualizes the range of skewness and kurtosis that a PDF can fit. For instance, the Gaussian distribution is located at the coordinate (0,3) of the skewness-kurtosis plot. The student's t-distribution is represented by the line $(0,y)$, where $y > 3$.

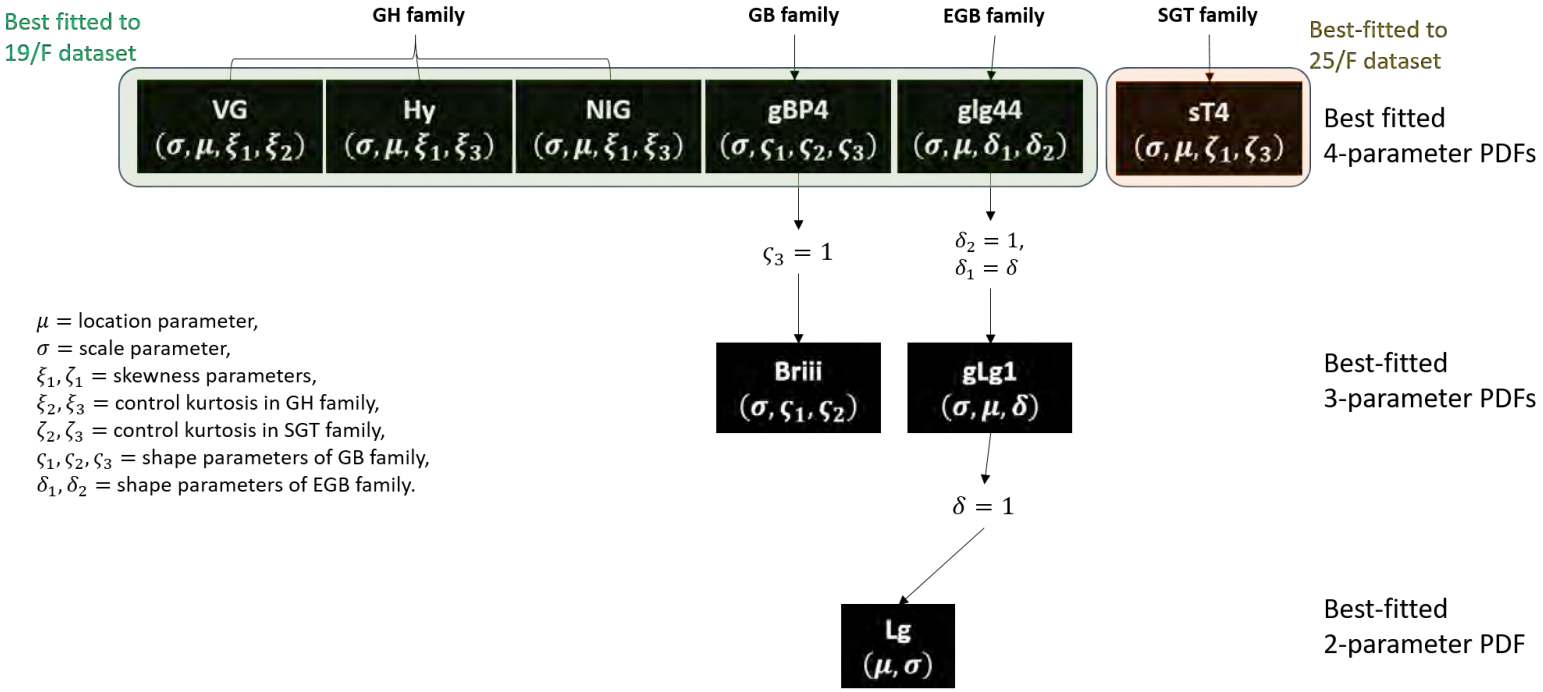

Figure 6.3: The best-fitting (according to Table 4.1) 2-, 3-, and 4-parameter PDFs to 19/F and 25/F datasets.

6.5 The trade-off between the goodness-of-fit and the number of parameters of PDFs

Table 6.6 ranks the 2-, 3-, and 4-parameter PDFs by their $\Delta_i^{(\mathrm{AIC})}$, showing 20 best-fitting 2, 3, and 4 parameter PDFs.

The 19/F dataset is better fitted (according to Table 4.1) by the 3-parameter PDFs (i.e. Briii, gLg1) and the 4-parameter PDFs (i.e. VG, Hy, gBP4, glg44, NIG). Note that the 19/F dataset is least leptokurtic among all datasets of this thesis. The 25/F dataset is best-fitted by the 4-parameter PDFs (i.e. sT4, Piv, JSu) followed by the 3-parameter Briii.

Table 6.6: $\Delta_i^{(\mathrm{AIC})}$ of the best-fitting PDFs of Tables 6.3, 6.4, 6.5.

	19/F dataset		**25/F dataset**	
Goodness-of-fit rank	PDF	$\Delta_i^{(\mathrm{AIC})}$	PDF	$\Delta_i^{(\mathrm{AIC})}$
1	Briii	0	sT4	0
2	gLg1	0.26	Piv	10.87
3	VG	0.26	JSu	10.93
4	Hy	0.27	Briii	12.81
5	gBP4	1.16	gBP4	14.09
6	glg44	1.34	gLg1	17.89
7	NIG	1.53	NIG	18.41
8	JSu	2.69	glg44	19.05
9	sT4	3.5	ghst4	20.25
10	Piv	5.44	Hy	21.62
11	gTK4	6.86	Brxii	27.95
12	ghst4	7.72	gLg2	28.07
13	SGED	8.04	VG	28.28
14	gLg2	9.72	gTK4	32.35
15	gLg4	11.83	gLg4	35.24
16	Brxii	13.08	gT4	42.73
17	sTK	36.96	symT3	43.36
18	gLg3	37.86	sTK	48.69
19	gT4	37.95	gLg3	52.36
20	symT3	38.21	Lg	52.96

6.6 Moments and peakedness — as a PDF's sufficient statistics of goodness-of-fit?

Can one scalar (i.e. a sufficient statistic) instead of the entire PDF be statistically sufficient to predict a PDF's goodness-of-fit?

To explore this issue, the following will use the Spearman's rank correlation coefficient (Section 4.5.1), which statistically decides if the ith PDF's any scalar metric is monotonically related to $\Delta_i^{(\mathrm{AIC})}$. The list of such candidate sufficient statistics have been given as (1) to (14) in Section 4.5). These are plotted individually against $\Delta_i^{(\mathrm{AIC})}$ in Figures 6.4 - 6.7 and Figures I.1 - I.6. The Spearman's rank correlation significance test results are reported in Table 6.7 for the most promising candidate sufficient statistics. The scalar metrics that do not have significant monotonic trend are stated in Appendix I.

In Table 6.7, at the significance level α of 0.01,

(i) the variance and peakedness of the 2-parameter PDFs are monotonically related to their goodness-of-fit ranks. This is the same as observed for 37th-floor datasets (Section 5.7).

(ii) the peakedness of 3-parameter PDFs are monotonically related to their goodness-of-fit ranks. This is the same as observed for 37th-floor datasets.

(iii) the fitted shapes of 4-parameter PDFs are not distinguished by any single candidate sufficient statistic. It is unlike the 37th-floor datasets where the excess-kurtosis has the monotonic relationship. The difference is that the 37th-floor datasets have heavier tails than the 19/F and 25/F datasets.

Table 6.7: $\hat{\rho}_{\Delta,y}$ and p-value of the Spearman's rank correlation significance test for 19/F and 25/F datasets. The corresponding scatter graphs for 19/F dataset are shown in Figures 6.4 and 6.5. The corresponding scatter graphs for 25/F dataset are shown in Figures 6.6 and 6.6. See Section 4.5.1 for the symbols used in this table.

	Ordinate, y	19/F dataset $\hat{\rho}_{\Delta,y}$ (p-value)	25/F dataset $\hat{\rho}_{\Delta,y}$ (p-value)
2-parameter PDFs	$\mu_{2_i}^{(\text{params})}$	0.764 (0.001)	0.746 (0.002)
	$\lvert\mu_{2_i}^{(\text{params})} - \hat{\mu}_2^{(\text{data})}\rvert$	0.703 (0.003)	0.691 (0.004)
	$\mathcal{P}_i^{(\text{params})}$	-0.754 (0)	-0.781 (0)
	$\lvert\mathcal{P}_i^{(\text{params})} - \hat{\mathcal{P}}^{(\text{data})}\rvert$	0.77 (0)	0.766 (0)
3-parameter PDFs	$\mathcal{P}_i^{(\text{params})}$	-0.777 (0)	-0.73 (0)
	$\lvert\mathcal{P}_i^{(\text{params})} - \hat{\mathcal{P}}^{(\text{data})}\rvert$	0.906 (0)	0.874 (0)
4-parameter PDFs	*None.*		

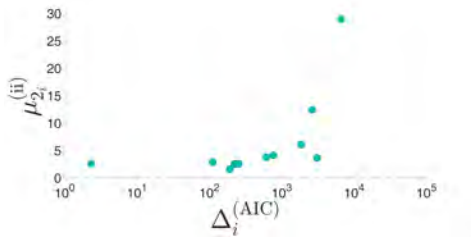

(a) $\mu_{2_i}^{(\mathrm{params})}$

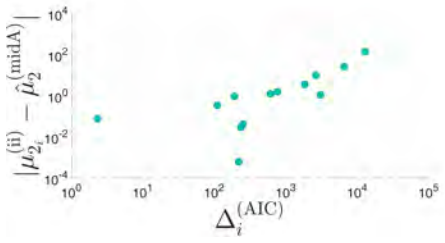

(b) $|\mu_{2_i}^{(\mathrm{params})} - \hat{\mu}_2^{(\mathrm{data})}|$

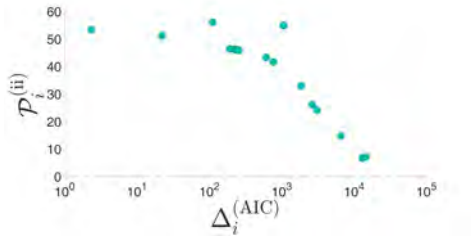

(c) $\mathcal{P}_i^{(\mathrm{params})}$

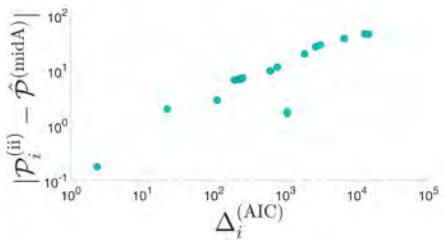

(d) $|\mathcal{P}_i^{(\mathrm{params})} - \hat{\mathcal{P}}^{(\mathrm{data})}|$

Figure 6.4: (19/F dataset) The scatter plots show a monotonic trend at $\alpha = 0.01$ for the 2-parameter PDFs. Each point in the scatter plots compounds to a PDF. (a) PDFs' variance, (b) Absolute deviation of PDFs' variance from dataset's variance, (c) PDF's peakedness, (d) Absolute deviation of PDFs' peakedness from dataset's peakedness.

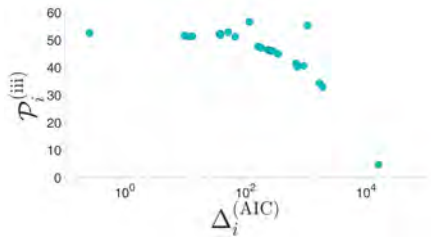

(a) $\mathcal{P}_i^{(\mathrm{params})}$

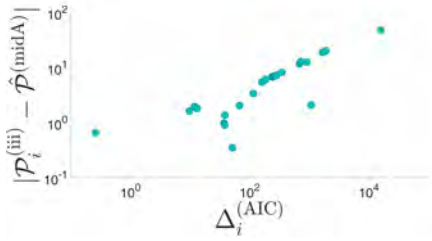

(b) $|\mathcal{P}_i^{(\mathrm{params})} - \hat{\mathcal{P}}^{(\mathrm{data})}|$

Figure 6.5: (19/F dataset) The scatter plots show a monotonic trend at $\alpha = 0.01$ for the 3-parameter PDFs. Each point in the scatter plots compounds to a PDF. (a) PDF's peakedness, (b) Absolute deviation of PDFs' peakedness from dataset's peakedness.

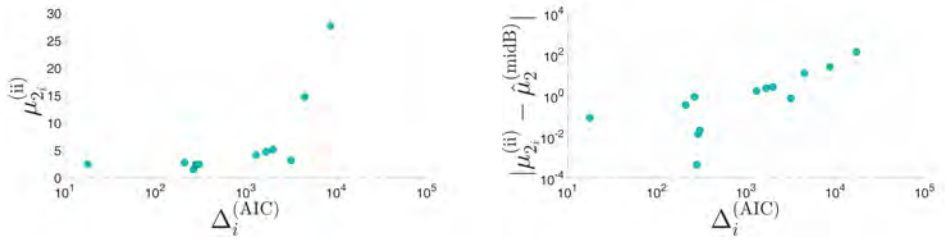

(a) $\mu_{2_i}^{(\mathrm{params})}$ (b) $|\mu_{2_i}^{(\mathrm{params})} - \hat{\mu}_2^{(\mathrm{data})}|$

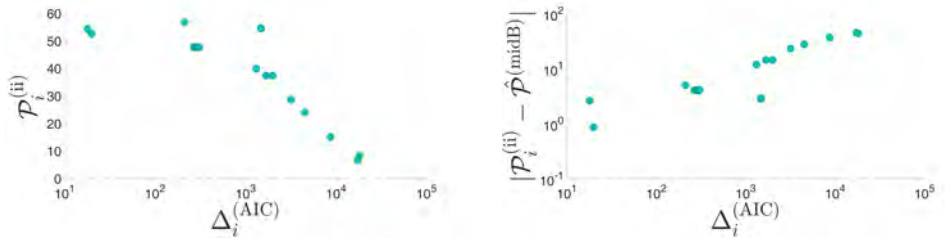

(c) $\mathcal{P}_i^{(\mathrm{params})}$ (d) $|\mathcal{P}_i^{(\mathrm{params})} - \hat{\mathcal{P}}^{(\mathrm{data})}|$

Figure 6.6: (25/F dataset) The scatter plots show a monotonic trend at $\alpha = 0.01$ for the 2-parameter PDFs. Each point in the scatter plots compounds to a PDF. (a) PDFs' variance, (b) Absolute deviation of PDFs' variance from dataset's variance, (c) PDF's peakedness, (d) Absolute deviation of PDFs' peakedness from dataset's peakedness.

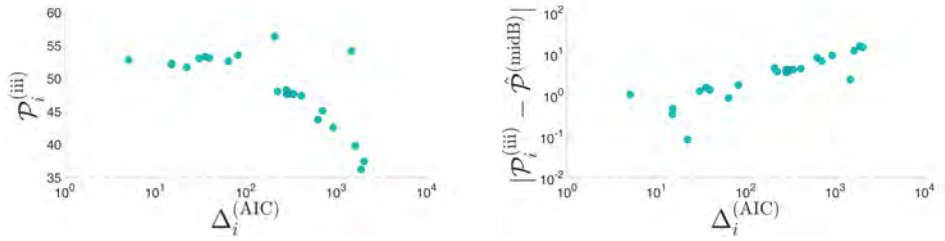

(a) $\mathcal{P}_i^{(\mathrm{params})}$ (b) $|\mathcal{P}_i^{(\mathrm{params})} - \hat{\mathcal{P}}^{(\mathrm{data})}|$

Figure 6.7: (25/F dataset) The scatter plots show a monotonic trend at $\alpha = 0.01$ for the 3-parameter PDFs. (a) PDF's peakedness, (b) Absolute deviation of PDFs' peakedness from dataset's peakedness.

Chapter 7

Conclusion

Two broad investigations have been covered in two parts of this thesis:

7.1 Part I

New eigen-based direction-finding signal-processing algorithms are advanced in closed form in Part I (Chapters 1 and 2) of this thesis. These algorithms, developed here for a single generalized p-u pair, could be used for a multiple-pair array, thereby relaxing the support-region restrictions. Deterministic Cramér-Rao bound analysis compares these various configurations by their relative precision for direction finding, at various orders of sensor directivity. Comparing between the customary p-u probe and the high-order generalization here: the latter's array manifold has a power of k, which fundamentally changes the obtainable Cramér-Rao bound, in ways that are analyzed in Section 2.3.3's observations 1) to 6): If azimuthal resolution is *somewhat* (but not categorically) more (less) important

than the elevational resolution, use a high-order figure-8 sensor in a horizontal (vertical) orientation but in vertical (horizontal) displacement from the omnidirectional pressure-sensor. If the azimuthal resolution is *categorically* more important than the elevational resolution, use Configurations (b) and (d). Besides the figure-8 sensor, other directional sensors could be investigated by the interested reader, e.g. the "cardioids" [119] or the "hypioids" [120].

7.2 Part II

New insights into the roadway sound-level distribution are explored by ranking various 2-, 3-, and 4-parameter leptokurtic probability density functions in terms of their goodness-of-fit to the roadway sound-level datasets measured on different days and at vertically different floors of a high-rise building. Chapter 4 explains the parameter estimation algorithm of the candidate PDFs and the goodness-of-fit ranking with respect to the Akaike information criterion (AIC) differences.

Chapter 5 discusses how the two datasets measured at the same location (37th-floor of a high-rise building) on two different days were different: The skewness and kurtosis of one dataset is smaller than the other dataset because less number of the occasionally-very-loud-vehicular sounds occurred during the measurement of the former dataset (see Table 5.2). However, for both of these heavy-tailed datasets,

1. the 4-parameter PDFs are more suitable to fit the distributions as they have better goodness-of-fit ranks than the 3- and 2-parameter PDFs. And

2. the generalizations of the student's t distribution (i.e. the skewed generalized t distribution family and the generalized-hyperbolic skewed student t distribution) are preferable over the other leptokurtic PDFs because of their best-fitting ranks.

Chapter 6 analyzes how the roadway sound level distribution of the datasets measured at vertically different floors (i.e. 19th- and 25th-floors) of the same high-rise building (as that in Chapter 5) were different: The 19/F dataset and 37/F dataset (b) are measured simultaneously but 19/F dataset has thinner tails (see Tables 6.2 and 5.2). The 3- and 4-parameter PDFs of generalized hyperbolic distribution, generalized beta of the second kind, and generalized logistic distributions have best-fitted the thinner-tailed 19/F dataset.

For all the heavy- and thinner-tailed datasets discussed in Chapters 5 and 6, a promising sufficient statistic to predict the goodness-of-fit (at 99% confidence level) of a 2-parameter or 3-parameter PDF is the peakedness (Section 4.5) of PDF. The excess-kurtosis is a promising sufficient statistic for a 4-parameter PDF in case of heavy-tailed (i.e. 37th-floor) datasets but not for the thinner-tailed (19/F and 25/F) datasets.

7.3 Future extension

7.3.1 Part I

The methodology of Part I can be used for other sensor arrays: The p-u probe has a figure-8 sensor that can be changed to a sensor with different gain pattern such as the uni-axial cardioid sensor. The unidirectional cardioid sensor of sec-

ond order (implemented using a pressure gradient) is commercially available i.e. Sankens CSR-2, CMS-10, CS-3E, and RCA Type BK-10A. An advantage of using the unidirectional sensor instead of the bidirectional figure-8 sensor would be in the reduction of the unambiguous region. Furthermore, to ensure unambiguity from the second hemisphere, a half-cardioid sensor is also commercially available i.e. Shure BETA 91A.

7.3.2 Part II

The methodology of Part II may be used for instantaneous sound pressure data. The advantage of finding a probabilistic model for sound pressure data is in employing a more appropriate model for Monte Carlo simulations of direction finding in Part I. The analysis of leptokurtic distribution modeling can readily be extended to other environments and a more comprehensive analysis can be performed by collecting data from multiple environments with high-rise buildings. The impact of occasionally very-loud vehicles in an environment prone to it can be further explored by using different generalizations of Student's t distribution especially the generalized hyperbolic skewed Student t. This may be achieved by deriving the close-form expressions of the percentile levels of L_{Aeq} data, such as performed in [76].

Appendix A

The closed-form estimators' equations of the nine spatial configurations of the higher-order p-v probe

This appendix lists the derived closed-form equations of the estimators proposed in Chapter 2.

Table A.1: Closed-form estimates $(\hat{\theta},\ \hat{\phi})$ of the azimuth-elevation bivariate direction-of-arrival, for configurations (a)-(c).

#	figure-8 sensor's location	figure-8 sensor's orientation	$(\hat{\theta},\hat{\phi})$
(a)	$(\Delta_x,0,0)$	x-axis	$\hat{\theta},\hat{\phi}$ underivable.
(b)	$(0,\Delta_y,0)$	x-axis	$\hat{\theta} = \begin{cases} \arcsin\left(\frac{\mathrm{sgn}(u)}{\cos(\hat{\phi})}\left\lvert\frac{\left[\hat{\mathbf{a}}^{(y)}_{P,V_x}\right]_2}{\left[\hat{\mathbf{a}}^{(y)}_{P,V_x}\right]_1}\right\rvert^{1/k}\right), & \text{if } \theta\in[0,\frac{\pi}{2}); \\ \pi-\arcsin\left(\frac{\mathrm{sgn}(u)}{\cos(\hat{\phi})}\left\lvert\frac{\left[\hat{\mathbf{a}}^{(y)}_{P,V_x}\right]_2}{\left[\hat{\mathbf{a}}^{(y)}_{P,V_x}\right]_1}\right\rvert^{1/k}\right), & \text{if } \theta\in[\frac{\pi}{2},\pi). \end{cases}$ $\hat{\phi} = \begin{cases} \arctan\left(\frac{1}{2\pi}\frac{\lambda}{\Delta_y}\angle\left(\mathrm{sgn}(u)\ \frac{\left[\hat{\mathbf{a}}^{(y)}_{P,V_x}\right]_2}{\left[\hat{\mathbf{a}}^{(y)}_{P,V_x}\right]_1}\right)\left\lvert\frac{\left[\hat{\mathbf{a}}^{(y)}_{P,V_x}\right]_1}{\left[\hat{\mathbf{a}}^{(y)}_{P,V_x}\right]_2}\right\rvert^{1/k}\right) \\ +\frac{\pi}{2}\left[\lvert\mathrm{sgn}\,(u)\rvert-\mathrm{sgn}\,(u)\right]. \end{cases}$
(c)	$(0,0,\Delta_z)$	x-axis	$\hat{\theta} = \arccos\left(\frac{1}{2\pi}\frac{\lambda}{\Delta_z}\angle\left(\mathrm{sgn}(u)\ \frac{\left[\hat{\mathbf{a}}^{(z)}_{P,V_x}\right]_2}{\left[\hat{\mathbf{a}}^{(z)}_{P,V_x}\right]_1}\right)\right).$ $\hat{\phi} = \begin{cases} \arccos\left(\frac{1}{\sin(\hat{\theta})}\left\lvert\frac{\left[\hat{\mathbf{a}}^{(z)}_{P,V_x}\right]_2}{\left[\hat{\mathbf{a}}^{(z)}_{P,V_x}\right]_1}\right\rvert^{1/k}\mathrm{sgn}(u)\right), & \text{if } \phi\in[0,\pi); \\ 2\pi-\arccos\left(\frac{1}{\sin(\hat{\theta})}\left\lvert\frac{\left[\hat{\mathbf{a}}^{(z)}_{P,V_x}\right]_2}{\left[\hat{\mathbf{a}}^{(z)}_{P,V_x}\right]_1}\right\rvert^{1/k}\mathrm{sgn}(u)\right), & \text{if } \phi\in[\pi,2\pi). \end{cases}$

Table A.2: Closed-form estimates $(\hat{\theta},\ \hat{\phi})$ of the azimuth-elevation bivariate direction-of-arrival, for configurations (d)-(f).

#	figure-8 sensor's location	figure-8 sensor's orientation	$(\hat{\theta},\hat{\phi})$
(d)	$(\Delta_x,0,0)$	y-axis	$\hat{\theta}=\begin{cases}\arcsin\left(\frac{\mathrm{sgn}(v)}{\sin(\hat{\phi})}\left\lvert\frac{\left[\hat{\mathbf{a}}^{(x)}_{P,V_y}\right]_2}{\left[\hat{\mathbf{a}}^{(x)}_{P,V_y}\right]_1}\right\rvert^{1/k}\right), & \text{if } \theta\in[0,\frac{\pi}{2});\\ \pi-\arcsin\left(\frac{\mathrm{sgn}(v)}{\sin(\hat{\phi})}\left\lvert\frac{\left[\hat{\mathbf{a}}^{(x)}_{P,V_y}\right]_2}{\left[\hat{\mathbf{a}}^{(x)}_{P,V_y}\right]_1}\right\rvert^{1/k}\right), & \text{if } \theta\in[\frac{\pi}{2},\pi).\end{cases}$ $\hat{\phi}=\begin{cases}\arctan\left[2\pi\frac{\Delta_x}{\lambda}\left\{\angle\left(\mathrm{sgn}(v)\ \frac{\left[\hat{\mathbf{a}}^{(x)}_{P,V_y}\right]_2}{\left[\hat{\mathbf{a}}^{(x)}_{P,V_y}\right]_1}\right)\right\}^{-1}\left\lvert\frac{\left[\hat{\mathbf{a}}^{(x)}_{P,V_y}\right]_2}{\left[\hat{\mathbf{a}}^{(x)}_{P,V_y}\right]_1}\right\rvert^{1/k}\right]\\ +\frac{\pi}{2}\left[\lvert\mathrm{sgn}\left(u\right)\rvert-\mathrm{sgn}\left(u\right)\right].\end{cases}$
(e)	$(0,\Delta_y,0)$	y-axis	$\hat{\theta},\hat{\phi}$ underivable.
(f)	$(0,0,\Delta_z)$	y-axis	$\hat{\theta}=\arccos\left(\frac{1}{2\pi}\frac{\lambda}{\Delta_z}\angle\left(\mathrm{sgn}(v)\ \frac{\left[\hat{\mathbf{a}}^{(z)}_{P,V_y}\right]_2}{\left[\hat{\mathbf{a}}^{(z)}_{P,V_y}\right]_1}\right)\right).$ $\hat{\phi}=\begin{cases}\arcsin\left(\frac{1}{\sin(\hat{\theta})}\left\lvert\frac{\left[\hat{\mathbf{a}}^{(z)}_{P,V_y}\right]_2}{\left[\hat{\mathbf{a}}^{(z)}_{P,V_y}\right]_1}\right\rvert^{1/k}\mathrm{sgn}(v)\right)\\ +\pi\left(\lvert\mathrm{sgn}(v)\rvert-\mathrm{sgn}(v)\right), & \text{if } \phi\in[-\frac{\pi}{2},\frac{\pi}{2});\\ \pi-\arcsin\left(\frac{1}{\sin(\hat{\theta})}\left\lvert\frac{\left[\hat{\mathbf{a}}^{(z)}_{P,V_y}\right]_2}{\left[\hat{\mathbf{a}}^{(z)}_{P,V_y}\right]_1}\right\rvert^{1/k}\mathrm{sgn}(v)\right), & \text{if } \phi\in[\frac{\pi}{2},\frac{3\pi}{2}).\end{cases}$

Table A.3: Closed-form estimates $(\hat{\theta},\ \hat{\phi})$ of the azimuth-elevation bivariate direction-of-arrival, for configurations (g)-(i).

#	figure-8 sensor's location	figure-8 sensor's orientation	$(\hat{\theta},\hat{\phi})$
(g)	$(\Delta_x,0,0)$	z-axis	$\hat{\theta}=\arccos\left(\operatorname{sgn}(w)\left\lvert\frac{\left[\hat{\mathbf{a}}^{(x)}_{P,Vz}\right]_2}{\left[\hat{\mathbf{a}}^{(x)}_{P,Vz}\right]_1}\right\rvert^{1/k}\right)$. $\hat{\phi}=\begin{cases}\arccos\left(\frac{1}{2\pi}\frac{\lambda}{\Delta_x}\frac{1}{\sin(\hat{\theta})}\angle\left(\operatorname{sgn}(w)\frac{\left[\hat{\mathbf{a}}^{(x)}_{P,Vz}\right]_2}{\left[\hat{\mathbf{a}}^{(x)}_{P,Vz}\right]_1}\right)\right), & \text{if } \phi\in[0,\pi);\\ 2\pi-\arccos\left(\frac{1}{2\pi}\frac{\lambda}{\Delta_x}\frac{1}{\sin(\hat{\theta})}\angle\left(\operatorname{sgn}(w)\frac{\left[\hat{\mathbf{a}}^{(x)}_{P,Vz}\right]_2}{\left[\hat{\mathbf{a}}^{(x)}_{P,Vz}\right]_1}\right)\right), & \text{if } \phi\in[\pi,2\pi).\end{cases}$
(h)	$(0,\Delta_y,0)$	z-axis	$\hat{\phi}=\begin{cases}\arcsin\left(\frac{1}{2\pi}\frac{\lambda}{\Delta_y}\frac{1}{\sin(\hat{\theta})}\angle\left(\operatorname{sgn}(w)\frac{\left[\hat{\mathbf{a}}^{(y)}_{P,Vz}\right]_2}{\left[\hat{\mathbf{a}}^{(y)}_{P,Vz}\right]_1}\right)\right), & \text{if } \phi\in[-\frac{\pi}{2},\frac{\pi}{2});\\ 2\pi-\arcsin\left(\frac{1}{2\pi}\frac{\lambda}{\Delta_y}\frac{1}{\sin(\hat{\theta})}\angle\left(\operatorname{sgn}(w)\frac{\left[\hat{\mathbf{a}}^{(y)}_{P,Vz}\right]_2}{\left[\hat{\mathbf{a}}^{(y)}_{P,Vz}\right]_1}\right)\right), & \text{if } \phi\in[\frac{\pi}{2},\frac{3\pi}{2}).\end{cases}$ $\hat{\theta}=\arccos\left(\left\lvert\frac{\left[\hat{\mathbf{a}}^{(y)}_{P,Vz}\right]_2}{\left[\hat{\mathbf{a}}^{(y)}_{P,Vz}\right]_1}\right\rvert^{1/k}\operatorname{sgn}(w)\right)$.
(i)	$(0,0,\Delta_z)$	z-axis	$\hat{\theta}=\begin{cases}\arccos\left(\lvert t\rvert^{1/k}\right), & \\ \quad\text{when } \left\lvert\lvert t\rvert^{1/k}-\frac{1}{2\pi}\frac{\lambda}{\Delta_z}\angle(t)\right\rvert < \left\lvert-\lvert t\rvert^{1/k}-\frac{1}{2\pi}\frac{\lambda}{\Delta_z}\angle(-t)\right\rvert;\\ \arccos\left(-\lvert t\rvert^{1/k}\right), & \\ \quad\text{when } \left\lvert\lvert t\rvert^{1/k}-\frac{1}{2\pi}\frac{\lambda}{\Delta_z}\angle(t)\right\rvert > \left\lvert-\lvert t\rvert^{1/k}-\frac{1}{2\pi}\frac{\lambda}{\Delta_z}\angle(-t)\right\rvert.\end{cases}$ $\hat{\phi}$ underivable

In Table A.3, $t=\frac{\left[\hat{\mathbf{a}}^{(z)}_{P,Vz}\right]_2}{\left[\hat{\mathbf{a}}^{(z)}_{P,Vz}\right]_1}$.

Appendix B

Closed-form Cramèr-Rao bound expressions for higher-order p-v probe direction-finding

This appendix lists the Cramèr-Rao bound expressions of the estimators proposed in Chapter 2.

Table B.1: Cramér-Rao bounds for the generalized p-u probe's nine configurations. Here, $\tilde{\Delta} := 2\pi\frac{\Delta_\varepsilon}{\lambda}$.

Configuration	$2M\frac{P_s}{P_n}\ \mathrm{CRB}_\theta^{(\cdot)}(\theta,\phi)$	$2M\frac{P_s}{P_n}\ \mathrm{CRB}_\phi^{(\cdot)}(\theta,\phi)$
(a) V_x at $(\Delta_x,0,0)$	∞	∞
(b) V_x at $(0,\Delta_y,0)$	$\frac{\left[\cos^{2\,k}(\phi)\sin^{2\,k}(\theta)+1\right]\left[\tilde{\Delta}^2\cos^4(\phi)\sin^2(\theta)+k^2\sin^2(\phi)\right]}{\tilde{\Delta}^2\,k^2\cos^{2\,k}(\phi)\cos^2(\theta)\sin^{2\,k}(\theta)}$	$\frac{\cos^{2-2\,k}(\phi)\left[\cos^{2\,k}(\phi)\sin^{2\,k}(\theta)+1\right]\left[\tilde{\Delta}^2\ \sin^2(\theta)\ \sin^2(\phi)+k^2\right]}{\tilde{\Delta}^2\,k^2\sin^{2\,k+2}(\theta)}$
(c) V_x at $(0,0,\Delta_z)$	$\frac{1+\cos^{2\,k}(\phi)\sin^{2\,k}(\theta)}{\tilde{\Delta}^2\cos^{2\,k}(\phi)\sin^{2\,k+2}(\theta)}$	$\frac{\cos^{2-2\,k}(\phi)\left[\cos^{2\,k}(\phi)\sin^{2\,k}(\theta)+1\right]\left[\tilde{\Delta}^2\sin^4(\theta)+k^2\cos^2(\theta)\right]}{\tilde{\Delta}^2\,k^2\sin^{2\,k+4}(\theta)\ \sin^2(\phi)}$
(d) V_y at $(\Delta_x,0,0)$	$\frac{\left[\sin^{2\,k}(\phi)\sin^{2\,k}(\theta)+1\right]\left[\tilde{\Delta}^2\sin^4(\phi)\sin^2(\theta)+k^2\cos^2(\phi)\right]}{\tilde{\Delta}^2\,k^2\sin^{2\,k}(\phi)\sin^{2\,k}(\theta)\ \cos^2(\theta)}$	$\frac{\sin^{2-2\,k}(\phi)\left[\sin^{2\,k}(\phi)\sin^{2\,k}(\theta)+1\right]\left[\tilde{\Delta}^2\ \sin^2(\theta)\ \cos^2(\phi)+k^2\right]}{\tilde{\Delta}^2\,k^2\sin^{2\,k+2}(\theta)}$
(e) V_y at $(0,\Delta_y,0)$	∞	∞
(f) V_y at $(0,0,\Delta_z)$	$\frac{1+\sin^{2\,k}(\phi)\sin^{2\,k}(\theta)}{\tilde{\Delta}^2\sin^{2\,k}(\phi)\sin^{2\,k+2}(\theta)}$	$\frac{\sin^{2-2\,k}(\phi)\left[\sin^{2\,k}(\phi)\sin^{2\,k}(\theta)+1\right]\left[\tilde{\Delta}^2\sin^4(\theta)+k^2\cos^2(\theta)\right]}{\tilde{\Delta}^2\,k^2\sin^{2\,k+4}(\theta)\ \cos^2(\phi)}$
(g) V_z at $(\Delta_x,0,0)$	$\frac{\cos^{2-2\,k}(\theta)\left[\cos^{2\,k}(\theta)+1\right]}{k^2\ \cos^2(\theta)}$	$\frac{\left[\cos^{2\,k}(\theta)+1\right]\left[\tilde{\Delta}^2\cos^2(\phi)\cos^4(\theta)+k^2\sin^2(\theta)\right]}{\tilde{\Delta}^2\,k^2\cos^{2\,k}(\theta)\ \sin^2(\phi)\ \sin^4(\theta)}$
(h) V_z at $(0,\Delta_y,0)$	$\frac{\cos^{2-2\,k}(\theta)\left[\cos^{2\,k}(\theta)+1\right]}{k^2\ \cos^2(\theta)}$	$\frac{\left[\cos^{2\,k}(\theta)+1\right]\left[\tilde{\Delta}^2\sin^2(\phi)\cos^4(\theta)+k^2\sin^2(\theta)\right]}{\tilde{\Delta}^2\,k^2\cos^2(\phi)\cos^{2\,k}(\theta)\ \sin^4(\theta)}$
(i) V_z at $(0,0,\Delta_z)$	$\frac{\cos^{2-2\,k}(\theta)\left[\cos^{2\,k}(\theta)+1\right]}{\sin^2(\theta)\left[\tilde{\Delta}^2\cos^2(\theta)+k^2\right]}$	∞

Appendix C

Non-empirical but theoretically conjectured distribution models of roadway sound-level

This appendix surveys the open literature for those probability density models of roadway sound-level that are based on theoretical conjectures. Please see Table C.1.

Table C.1: Earlier probability distribution models of roadway sound.

Ref.	**Verification by Empirical data?**	**Traffic flow**	**CDF or PDF?**	**Comments**
[72]*	No	NA	Both	PDF looks non-Gaussian & asymmetric.
[121]	No	Freely flowing	PDF	PDF is based on normalized sound intensity data.
[74]*	No	Freely flowing	Neither	PDF is "nearly" Gaussian.
[75]*	No	Freely flowing	PDF	PDF is not symmetric.
[122]	No	Interrupted	Both	Used Gram-Charlier series type A for sound intensity ratio.
[123]	Yes (roadside)	Freely flowing	Both	Conclusion: Roadway sound-level intensity ratio is gamma distributed.
[73]*	Yes (roadside)	Freely flowing	CDF	Conclusion: CDF is Gaussian but skewed.
[59]*	Yes (roadside)	Interrupted	CDF	Used Gaussian CDF.
[124]*	Yes (roadside)	Freely flowing	PDF	Used Poisson distribution on the number of passing-by vehicles.
[125]*	Yes (roadside)	Interrupted	Both	
[60]	Yes (roadside)	Any	Both	Used Gram-Charlier series type A for sound energy data.
[39]*	Yes (roadside)	Any	Both	Conclusion: PDF = leptokurtic.
[76]*	Yes (roadside)	Interrupted	Both	Used a weighted sum of two Gaussian PDFs.

* used equivalent sound pressure level data L_{eq}.

** used A-weighted equivalent sound pressure level data L_{Aeq}.

Appendix D

List of 2-parameter PDFs fitted to the empirical data

Table D.1 lists PDFs with two parameters (a, b) fitted to the empirical data.

Table D.1: The 2-parameter PDFs fitted to the empirical data.

PDF	**PDF Expression**	**Reference**
Gaussian distribution (N)	$\frac{1}{\sqrt{2\pi b^2}} e^{-\frac{(x-a)^2}{2b^2}}$, $b^2 > 0.$	Equation (13.1) of [85]
Logistic distribution a.k.a. sech-square(d) distribution (Lg)	$\frac{\exp\left(-\frac{x-a}{b}\right)}{b\left(1+\exp\left(-\frac{x-a}{b}\right)\right)^2} = \frac{1}{4b}\text{sech}^2\left(\frac{x-a}{2b}\right)$, $b > 0.$	Chapter 22, Equation (2) of [126]
Hyperbolic secant distribution (HS)	$\frac{1}{2b} \cdot \frac{1}{\cosh\left(\pi \frac{x-a}{2b}\right)}$, $b > 0.$	Equation (1.12) of [127]
Log-logistic distribution (LLg)	$\frac{(b/a)(x/a)^{b-1}}{\left\{1+(x/a)^b\right\}^2}$, $a > 0, b > 0.$	Equation (1.1) of [128]

Table D.1 continues on the next page.

Continuation of Table D.1.

Non-central t distribution (nT)	$\frac{b^{\frac{b}{2}}\exp\left(-\frac{ba^2}{2(x^2+b)}\right)}{\sqrt{\pi}\Gamma(\frac{b}{2})2^{\frac{b-1}{2}}(x^2+b)^{\frac{b+1}{2}}}\int_0^\infty x^b\exp\left(-\frac{1}{2}\left(x-\frac{ax}{\sqrt{x^2+b}}\right)^2\right)dx,$ $b>0.$	Page 77 of [129]
Location family with standard student's t distribution (T2)	$\frac{\Gamma(\frac{b+1}{2})}{\Gamma(\frac{b}{2})\sqrt{\pi b}}\left(1+\frac{1}{b}(x-a)^2\right)^{-\frac{b+1}{2}},\quad b>0.$	Page 507 of [130] with $\sigma=1$.
Log normal distribution (LN)	$\frac{1}{x}\cdot\frac{1}{b\sqrt{2\pi}}\exp\left(-\frac{(\ln x-a)^2}{2b^2}\right),\quad b>0.$	Equation (14.3) of [126]
Laplace distribution (Lp)	$\frac{1}{2b}\exp\left(-\frac{\lvert x-a\rvert}{b}\right),\quad b>0.$	Chapter 23, Equation (1) of [126]
Rice distribution (Rc)	$\frac{x}{b^2}\exp\left(\frac{-(x^2+a^2)}{2b^2}\right)I_0\left(\frac{xa}{b^2}\right),\quad a\geq 0, b\geq 0.$	First equation of [131]
Gamma distribution (G)	$\frac{b^a x^{a-1}e^{-bx}}{\Gamma(a)},\quad x>0, a>0, b>0.$	Equation (17.23) of [85]
Inverse gamma distribution (IG)	$\frac{b^a}{\Gamma(a)}x^{-a-1}\exp\left(-\frac{b}{x}\right),\quad x>0, a>0, b>0.$	Equation (11) of [132]
Inverse Gaussian distribution (IGs)	$\left[\frac{b}{2\pi x^3}\right]^{1/2}\exp\left\{\frac{-b(x-a)^2}{2a^2x}\right\},\quad x>0, a>0, b>0.$	Equation (15.4a) of [85]
Paralogistic distribution (PLg)	$\frac{a^2(x/b)^a}{x[1+(x/b)^a]^{a+1}},\quad x>0, a>0, b>0$	Section A.2.3.4 of [133]
Weibull distribution (W)	$\begin{cases}\frac{a}{b}\left(\frac{x}{b}\right)^{a-1}e^{-(x/b)^a} & x\geq 0,\\ 0 & x<0,\end{cases}, \quad a>0, b>0.$	Equation (4-43) of [134]
Cauchy distribution (Cy)	$\frac{1}{\pi b}\left[\frac{b^2}{(x-a)^2+b^2}\right],\quad b>0.$	Chapter 16, Equation (16.1)of [85]
Log Cauchy distribution (LCy)	$\frac{1}{x\pi}\left[\frac{b}{(\ln x-a)^2+b^2}\right],\quad b>0.$	Page 86 of [135]
Gumbel distribution (Gb)	$\exp\left[-\left\{\frac{x-a}{b}+\exp\left(-\frac{x-a}{b}\right)\right\}\right],\quad b>0.$	Equation (6.21) of [136]
Gompertz distribution (Go)	$bae^a e^{bx}\exp\left(-ae^{bx}\right),\quad b>0.$	Equation (2) of [137]
Shifted Gompertz distribution (sGo)	$be^{-bx}e^{-ae^{-bx}}\left[1+a\left(1-e^{-bx}\right)\right],\quad x\geq 0, a\geq 0, b\geq 0.$	Equation (2) of [138]
Non-central chi-squared distribution (nCS)	$\frac{1}{2}e^{-(x+a)/2}\left(\frac{x}{a}\right)^{b/4-1/2}I_{b/2-1}(\sqrt{ax}),\quad x\geq 0, a>0, b>0.$	Chapter 28 of [85]
Scaled inverse chi-squared distribution (sCS)	$\frac{(ba/2)^{a/2}}{\Gamma(a/2)}\frac{\exp\left[\frac{-ab}{2x}\right]}{x^{1+a/2}},\quad x>0, a>0, b>0.$	Page 480 of [139]
Levy distribution (L)	$\sqrt{\frac{b}{2\pi}}\frac{e^{-\frac{b}{2(x-a)}}}{(x-a)^{3/2}},\quad x\geq a, b>0.$	Page 5 of [140]

In Table D.1, $\Gamma(.)$ = gamma function, and $I_\times(.)$ = modified Bessel function of the first kind with $\times$ order.

Appendix E

List of 3-parameter PDFs fitted to the empirical data

Table E.1 lists PDFs with three parameters (a, b, c) fitted to the empirical data.

Table E.1: The 3-parameter PDFs fitted to the empirical data. If any 2-parameter PDF represents a special case of a 3-parameter PDF, it is linked by an arrow in Figure G.1 of Appendix G.

PDF	**PDF Expression**	**Reference**
Skew normal distribution (SN)	$\frac{2}{b\sqrt{2\pi}} e^{-\frac{(x-a)^2}{2b^2}} \int_{-\infty}^{c\left(\frac{x-a}{b}\right)} e^{-\frac{t^2}{2}}\, dt,$ $b > 0.$	Equation (4.2) of [141]
Non-standardized Student's t-distribution (symT3)	$\frac{\Gamma\left(\frac{c+1}{2}\right)}{\Gamma\left(\frac{c}{2}\right)\sqrt{\pi c}b} \left(1 + \frac{1}{c}\left(\frac{x-a}{b}\right)^2\right)^{-\frac{c+1}{2}},$ $b > 0, c > 0.$	Page 507 of [130]

Table E.1 continues on the next page.

Continuation of Table E.1.

Birnbaum–Saunders distribution (BS)	$\frac{\sqrt{\frac{x-a}{b}}+\sqrt{\frac{b}{x-a}}}{2c(x-a)}\phi\left(\frac{\sqrt{\frac{x-a}{b}}-\sqrt{\frac{b}{x-a}}}{c}\right)$, $x > a; c, b > 0$.	Equation (2.2) of [142]
Burr distribution a.k.a. Singh-Maddala distribution (Brxii)	$\frac{ca}{b}\left(\frac{x}{b}\right)^{c-1}\left[1+\left(\frac{x}{b}\right)^{c}\right]^{-a-1}$, $x, a, b, c > 0$.	Equation (4) of [116]
Generalized logistic distribution type-I a.k.a. skewed logistic distribution (gLg1)	$\frac{c\ e^{-\left(\frac{x-a}{b}\right)}}{b\left(1+e^{-\left(\frac{x-a}{b}\right)}\right)^{c+1}}$, $b, c > 0$.	Table 9.1.1 of [143]
Generalized logistic distribution type II (gLg2)	$\frac{ce^{-c\left(\frac{x-a}{b}\right)}}{(1+e^{-\left(\frac{x-a}{b}\right)})^{c+1}}$, $b, c > 0$.	Table 9.1.1 of [143]
Generalized logistic distribution type III (gLg3)	$\frac{1}{\beta(c,c)}\frac{e^{-c\left(\frac{x-a}{b}\right)}}{(1+e^{-\left(\frac{x-a}{b}\right)})^{2\alpha}}$, $b, c > 0$.	Table 9.1.1 of [143]
Location family with standard generalized logistic distribution type IV (gLg4)	$\frac{1}{\beta(b,c)}\frac{e^{-c(x-a)}}{(1+e^{-(x-a)})^{b+c}}$, $b, c > 0$.	Table 9.1.1 of [143]
Shifted log-logistic distribution (sLLg)	$\frac{\left(1+\frac{c(x-a)}{b}\right)^{-(1/c+1)}}{b\left[1+\left(1+\frac{c(x-a)}{b}\right)^{-1/c}\right]^2}$, $1 + c(x-a)/b \geqslant 0$.	[144]
Pearson type V (IG3)	$\frac{\lvert b\rvert^c}{\Gamma(c)}\lvert x-a\rvert^{-c-1}e^{-(b/(x-a))}$, $\frac{b}{x-a} > 0,\ b \neq 0, c > 0$.	Page 21 of [145]
Exponential Gaussian distribution (XG)	$\frac{c}{2}e^{\frac{c}{2}(2a+cb^2-2x)}\operatorname{erfc}\left(\frac{a+cb^2-x}{\sqrt{2}b}\right)$, $b, c > 0$.	Equation (1) of [146]
Exponential power distribution (XP)	$\frac{c}{2b\Gamma(1/c)}\ e^{-(\lvert x-a\rvert/b)^c}$, $b, c > 0$.	Equation (2) of [147]

Table E.1 continues on the next page.

Continuation of Table E.1.

Generalized extreme value distribution (GEV)	$\frac{1}{b}\,t(x)^{c+1}e^{-t(x)},\ \ b>0$ where $t(x)=\begin{cases}(1+c(\frac{x-a}{b}))^{-1/c} & \text{if } c\neq 0\\ e^{-(x-a)/b} & \text{if } c=0\end{cases}$.	Equation (2) of [148]
Davis distribution (Dv)	$\frac{b^c(x-a)^{-1-c}}{\left(e^{\frac{b}{x-a}}-1\right)\Gamma(c)\zeta(c)}$, $x>a; a,b,c>0$.	Equation (7.10) of [149]
Symmetric Tukey lambda distribution (sTK)	Closed-form does not exist. [1] The quantile function is: $Q(x)=a+\frac{1}{b}\left[\frac{x^c-1}{c}-\frac{(1-x)^c-1}{c}\right],\ \ b>0.$	Equation (1.6) of [150]
Location family with standard Beta prime distribution (BP3)	$\frac{(x-b)^{a-1}(1+(x-b))^{-a-c}}{\beta(a,c)},\ \ x,a,b,c>0.$	Chapter 24, Equation (28) of [126]
Location family with standard Gompertz distribution (Go3)	$bae^a e^{b(x-c)}\exp\left(-ae^{b(x-c)}\right),\quad b>0.$	Equation (2) of [137]
Non-central F-distribution (F3)	$\sum_{k=0}^{\infty}\frac{e^{-a/2}(a/2)^k}{\beta\left(\frac{c}{2},\frac{b}{2}+k\right)k!}\left(\frac{b}{c}\right)^{\frac{b}{2}+k}\left(\frac{c}{c+bx}\right)^{\frac{b+c}{2}+k}x^{b/2-1+k}$, $x,b,c>0.$	Equation (2.19) of [151]
Pearson type III distribution a.k.a. location family with standard gamma distribution (G3)	$\frac{1}{\lvert b\rvert^c\Gamma(c)}\lvert x-a\rvert^{c-1}e^{-(x-a)/b}$, $a>0, b\neq 0,\ \frac{x-a}{b}\geq 0.$	Page 14 of [145]

Table E.1 continues on the next page.

[1] The package *gld* (version 2.4.1 of the R software) numerically solves PDF from the quantile function of the symmetric Tukey lambda distribution.

Continuation of Table E.1.

Location family with standard Rice distribution (Rc3)	$\frac{(x-c)}{b^2}\exp\left(\frac{-((x-c)^2+a^2)}{2b^2}\right)I_0\left(\frac{xa}{b^2}\right)$, $a\geq 0, b\geq 0$.	First equation of [131]
Location family with standard shifted Gompertz distribution (sGo3)	$be^{-bx}e^{-ae^{-bx}}\left[1+a\left(1-e^{-bx}\right)\right]$, $x\geq 0, a\geq 0, b\geq 0$.	Equation (2) of [138]
Location family with standard Weibull distribution (W3)	$\begin{cases}\frac{a}{b}\left(\frac{x-c}{b}\right)^{a-1}e^{-((x-c)/b)^a} & x\geq c,\\ 0 & x<c,\end{cases}$, $a>0, b>0$.	Equation (4-43) of [134]
Location family with standard paralogistic distribution (pLg3)	$\frac{a^2((x-c)/b)^a}{(x-c)[1+((x-c)/b)^a]^{a+1}}$, $x>c, a>0, b>0$.	Section A.2.3.4 of [133]
Skewed Cauchy distribution (sCy)	$\frac{1}{b\pi(\frac{\lvert x-a\rvert^2}{b^2(c\ \mathrm{sign}(x-a)+1)^2}+1)}$, $b>0, -1<c<1$	Page 22 of [152]
Skewed Laplace distribution (sLp3)	$\frac{e^{\frac{-\lvert x-a+m\rvert}{vb(1+c\ \mathrm{sign}(x-a+m))}}}{2vb}$, $b>0, -1<c<1$. For values of m,v, see page 14 of [152]	Page 14 of [152].
Pearson type II distribution (Pii)	$\frac{\Gamma(2c)}{\Gamma(c)^2}\left(\left(\frac{x-a}{b}\right)\left(1-\frac{x-a}{b}\right)\right)^{c-1}$, $\frac{x-a}{b}>0$; $b, c>0$.	Section 17 of [86]
Scale family with standard inverse Gaussian distribution (sIGs)	$\left[\frac{bc}{2\pi x^3}\right]^{1/2}\exp\left\{\frac{-b(\frac{x}{c}-a)^2}{2a^2\frac{x}{c}}\right\}$, $x>0, a>0, b>0$.	Equation (15.4a) of [85]
Inverse Burr distribution a.k.a. Dagum distribution (Briii)	$\frac{ac}{x}\left(\frac{(\frac{x}{b})^{ac}}{((\frac{x}{b})^a+1)^{c+1}}\right)$, $x, a, b, c>0$.	Equation (22) of [116]

In Table E.1, $\beta(.)$ = beta function, $\Gamma(.)$ = gamma function, $\zeta(.)$ = Reimann zeta function, $I_\times(.)$ = modified Bessel function of the first kind of order $\times$, and sign(.) = signum function.

Appendix F

List of 4-parameter PDFs fitted to the empirical data

Table F.1 lists PDFs with four parameters (a, b, c, d) fitted to the empirical data.

Table F.1: The 4-parameter PDFs fitted to the empirical data. If any 3-parameter PDF represents a special case of a 4-parameter PDF, it is linked by an arrow in Figure G.1 of Appendix G.

PDF	**PDF Expression**	**Reference**
Exponential generalized beta of the second kind a.k.a. location-scale family with standard generalized logistic distribution type IV (glg44)	$\frac{1}{d\ \beta(b,c)} \frac{e^{-c\left(\left(\frac{x-a}{d}\right)\right)}}{\left(1+e^{-\left(\left(\frac{x-a}{d}\right)\right)}\right)^{b+c}}, \quad b,c,d>0.$	Table 9.1.1 of [143]
Generalized hyperbolic skewed student t (ghsT4)	$\frac{2^{\frac{1-d}{2}} b^d \lvert c\rvert^{\frac{d+1}{2}} K_{\frac{d+1}{2}}\left(\sqrt{c^2\left(b^2+(x-a)^2\right)}\right) \exp(c(x-a))}{\Gamma\left(\frac{d}{2}\right)\sqrt{\pi}\left(b^2+(x-a)^2\right)^{\frac{d+1}{2}}},$ $b>0, d>2$	Equation (8) of [115]
Variance gamma distribution (VG)	$\frac{\left(\sqrt{d^2-b^2}\right)^{2c} \lvert x-a\rvert^{c-1/2} K_{c-1/2}(d\lvert x-a\rvert)}{\sqrt{\pi}\Gamma(c)(2d)^{c-1/2}} e^{b(x-a)},$ $c>0.$	Equation (1.14) of [114]
Hyperbolic distribution (Hy)	$\frac{\left(\sqrt{d^2-c^2}\right)}{2bdK_1\left(b\left(\sqrt{d^2-c^2}\right)\right)} e^{-d\sqrt{b^2+(x-a)^2}+c(x-a)},$ $b>0, \lvert c\rvert< d$	Page 14 of [114]
Normal Inverse Gaussian distribution (NIG)	$\frac{bdK_1\left(d\sqrt{b^2+(x-a)^2}\right)}{\pi\sqrt{b^2+(x-a)^2}} e^{b\left(\sqrt{d^2-c^2}\right)+c(x-a)},$ $b>0, \lvert c\rvert< d.$	Page 14 of [114]
Pearson distribution type I (Pi)	$\frac{\Gamma(c+d)}{\Gamma(c)\Gamma(d)} \left(\frac{x-a}{b}\right)^{c-1} \left(1-\frac{x-a}{b}\right)^{d-1},$ $c,d>0,\ 0<\frac{x-a}{b}<1.$	Page 11 of [145]
Pearson distribution type IV (Piv)	$\frac{\left\lvert\frac{\Gamma(c+d/2i)}{\Gamma(c)}\right\rvert^2}{b\ \beta(c-1/2,1/2)} \left[1+\left(\frac{x-a}{b}\right)^2\right]^{-c} e^{-d\ \tan^{-1}\left(\frac{x-a}{b}\right)},$ $b>0, c>1/2, d\neq 0.$	Page 16 of [145]
Pearson distribution type VI (Pvi)	$\frac{\Gamma(c+d)}{\lvert b\rvert\Gamma(c)\Gamma(d)} \left(\frac{x-a}{b}\right)^{c-1} \left(1+\frac{x-a}{b}\right)^{-c-d},$ $b\neq 0,\ c,d>0,\ \frac{x-a}{b}>0.$	Page 23 of [145]
Skewed generalized error distribution (SGED)	$\frac{de^{-\left(\frac{\lvert x-a+m\rvert}{vb(1+c\ \mathrm{sign}(x-a+m))}\right)^d}}{2vb\Gamma(1/d)}, \quad b,d>0; \quad -1<c<1.$ For values of m, v, see page 8 of [152]	Page 8 of [152]
Generalized t distribution (gT4)	$\frac{c}{2vbd^{1/c}\beta\left(\frac{1}{c},d\right)\left(\frac{\lvert x-a\rvert^c}{d(vb)^c}+1\right)^{\frac{1}{c}+d}}, \quad b,c,d>0.$ For value of v, see page 10 of [152]	Page 10 of [152].

Table F.1 continues on the next page.

Continuation of Table F.1.

Skewed t distribution (sT4)	$\frac{\Gamma(\frac{1}{2}+d)}{vb(\pi d)^{1/2}\Gamma(d)(\frac{\lvert x-a+m\rvert^2}{d(vb)^2(c\ \mathrm{sign}(x-a+m)+1)^2}+1)^{\frac{1}{2}+d}}$, $b, d > 0; -1 < c < 1.$ For values of m, v, see page 12 of [152]	Page 12 of [152]
Generalized beta prime distribution a.k.a. generalized beta distribution of second kind (gBP4)	$\frac{\lvert a\rvert y^{ac-1}}{b^{ap}\beta(c,d)(1+(y/b)^a)^{c+d}}$, $b, c, d > 0.$	Equation (2.12) of [89]
Generalized lambda distribution a.k.a. Tukey-Lambda distribution a.k.a. asymmetric lambda distribution (gTK4)	Closed-form does not exist. [1] The quantile function is: $Q(x) = a + \frac{1}{b}\left[\frac{x^c-1}{c} - \frac{(1-x)^d-1}{d}\right]$, $b > 0.$	Equation (1.6) of [150]
Johnson's S_U distribution (JSu)	$\frac{d}{b\sqrt{2\pi}}\frac{1}{\sqrt{1+\left(\frac{x-a}{b}\right)^2}}e^{-\frac{1}{2}\left(c+d\sinh^{-1}\left(\frac{x-a}{b}\right)\right)^2}$, $b, d > 0.$	Equation (33) of [153]

In Table F.1, $\beta(.)$ = beta function, $\Gamma(.)$ = gamma function, $K_\times(.)$ = modified Bessel function of the second kind of order $\times$, sign(.) = signum function.

[1] The package *gld* (version 2.4.1 of the R software) numerically solves PDF from the quantile function of the symmetric Tukey lambda distribution.

Appendix G

The interrelationships of 2-parameter, 3-parameter, and 4-parameter PDFs

Generalizations of the 2-parameter PDFs to the 3-parameter PDFs and generalization of the 3-parameter PDFs to the 4-parameter PDFs are shown in Figure G.1. The 4-parameter PDFs possess all parameters of the 3-parameter PDFs, connected by the arrow, plus one additional parameter. And the 3-parameter PDFs contain all parameters of the 2-parameter PDFs, connected by the arrow, plus one additional parameter.

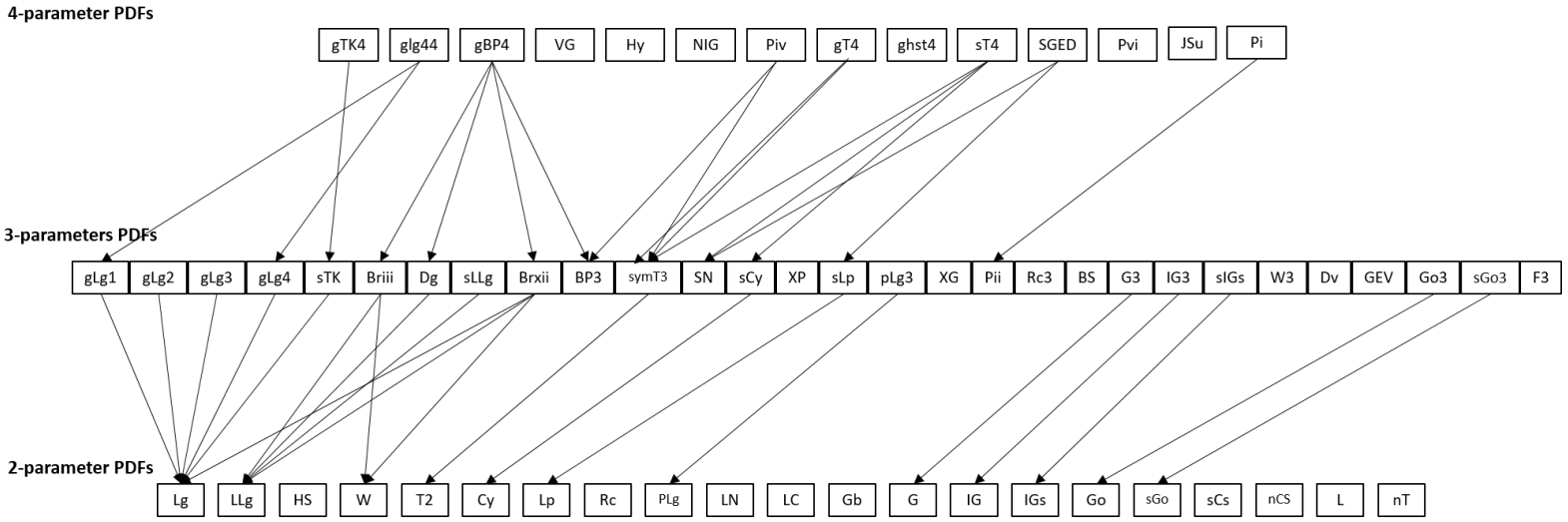

Figure G.1: The interrelationship tree diagram of the 2-, 3-, and 4-parameter PDFs.

Appendix H

(37th-floor datasets) Scatter-plots of $\Delta_i^{(\mathrm{AIC})}$ vs y (Section 4.5.1) with no monotonic trend

This appendix shows the results of Spearman's rank correlation significance test of $\Delta_i^{(\mathrm{AIC})}$ vs y (Section 4.5.1) with no significant monotonic trend at $\alpha = 0.01$: Section H.1 for 2-parameter PDFs, Section H.2 for 3-parameter PDFs, and Section H.3 for 4-parameter PDFs.

H.1 For 2-parameter PDFs

Table H.1: $\hat{\rho}_{\Delta,y}$ and p-value of the Spearman's rank correlation significance test. The corresponding scatter graphs for 37/F dataset (a) are shown in Figure H.1. The corresponding scatter graphs for 37/F dataset (b) are shown in Figure H.2. See Section 4.5.1 for the symbols used in this table.

Ordinate, y	37/F dataset (a) $\hat{\rho}_{\Delta,y}$ (p-value)	37/F dataset (b) $\hat{\rho}_{\Delta,y}$ (p-value)
$\gamma_{1_i}^{(\text{params})}$	0.481 (0.059)	0.475 (0.063)
$\lvert\gamma_{1_i}^{(\text{params})} - \hat{\gamma}_1^{(\text{data})}\rvert$	-0.397 (0.128)	-0.418 (0.107)
$\gamma_{e_i}^{(\text{params})}$	0.095 (0.75)	-0.171 (0.541)
$\lvert\gamma_{e_i}^{(\text{params})} - \hat{\gamma}_e^{(\text{data})}\rvert$	-0.095 (0.75)	0.171 (0.541)
$\mu_{3_i}^{(\text{params})}$	0.232 (0.426)	0.389 (0.152)
$\lvert\mu_{3_i}^{(\text{params})} - \hat{\mu}_3^{(\text{data})}\rvert$	0.714 (0.002)	0.731 (0.001)
$\mu_{4_i}^{(\text{params})}$	0.127 (0.733)	0.055 (0.881)
$\lvert\mu_{4_i}^{(\text{params})} - \hat{\mu}_4^{(\text{data})}\rvert$	0.629 (0.014)	0.718 (0.002)
$\kappa_{4_i}^{(\text{params})}$	0.018 (0.973)	-0.036 (0.924)
$\lvert\kappa_{4_i}^{(\text{params})} - \hat{\kappa}_4^{(\text{data})}\rvert$	0.532 (0.044)	0.491 (0.056)

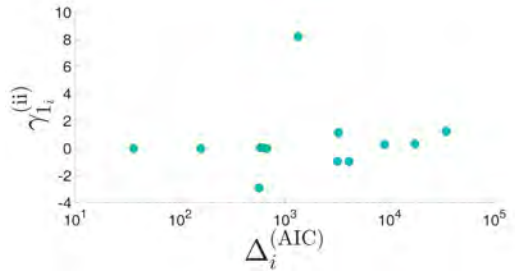

(a) $\gamma_{1_i}^{(\mathrm{params})}$

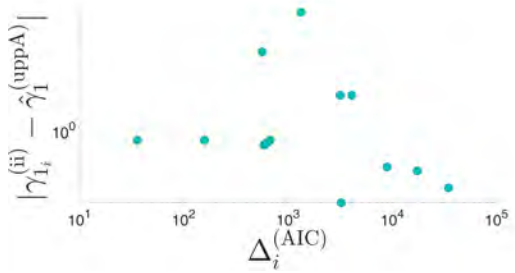

(b) $|\gamma_{1_i}^{(\mathrm{params})} - \hat{\gamma}_1^{(\mathrm{data})}|$

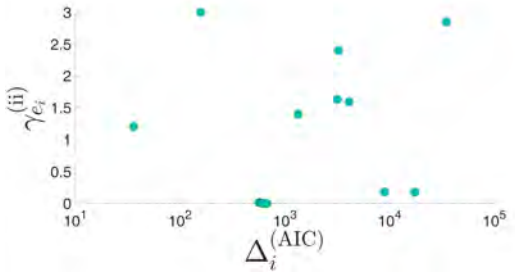

(c) $\gamma_{e_i}^{(\mathrm{params})}$

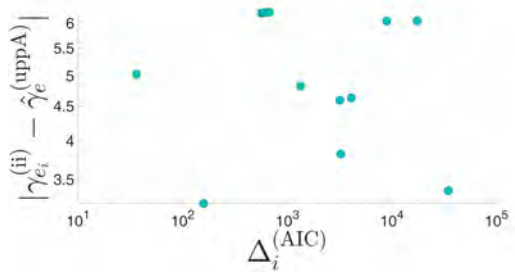

(d) $|\gamma_{e_i}^{(\mathrm{params})} - \hat{\gamma}_e^{(\mathrm{data})}|$

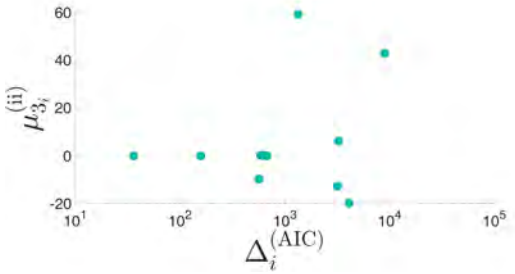

(e) $\mu_{3_i}^{(\mathrm{params})}$

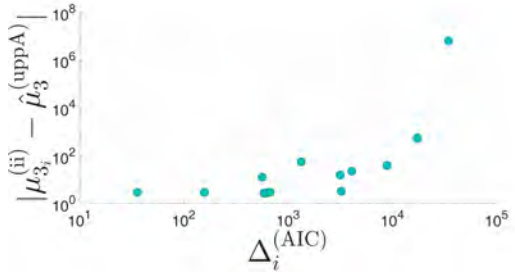

(f) $|\mu_{3_i}^{(\mathrm{params})} - \hat{\mu}_3^{(\mathrm{data})}|$

Sub-figures continue on the next page.

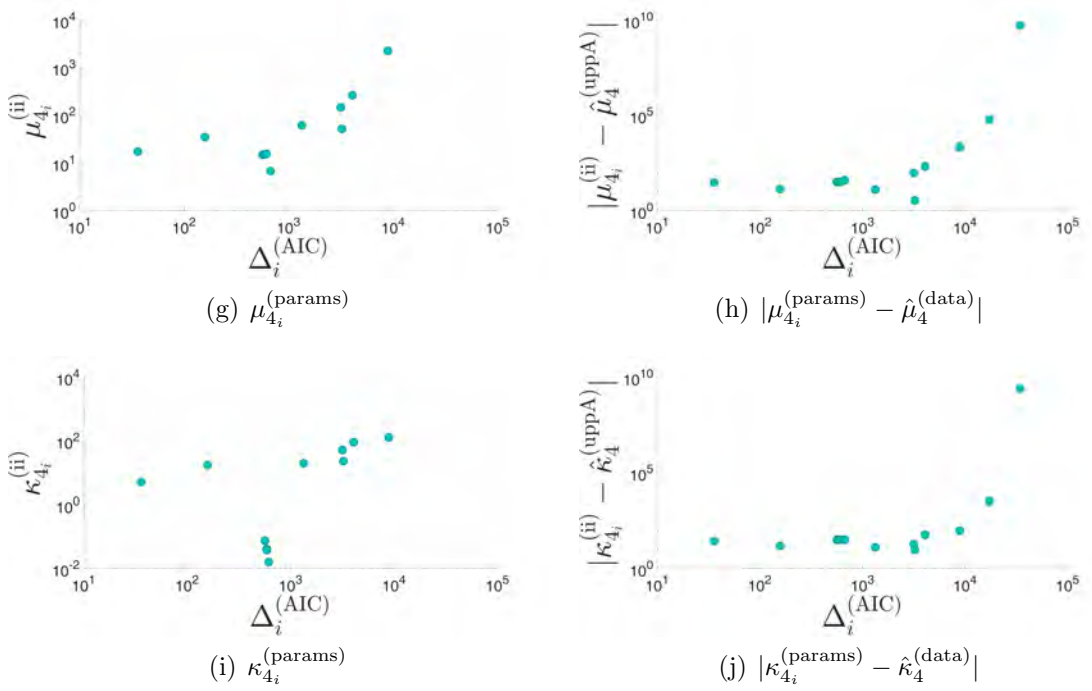

(g) $\mu_{4_i}^{(\mathrm{params})}$ (h) $|\mu_{4_i}^{(\mathrm{params})} - \hat{\mu}_4^{(\mathrm{data})}|$

(i) $\kappa_{4_i}^{(\mathrm{params})}$ (j) $|\kappa_{4_i}^{(\mathrm{params})} - \hat{\kappa}_4^{(\mathrm{data})}|$

Figure H.1: (37/F dataset (a)) The scatter plots with no monotonic trend at $\alpha = 0.01$. (a) PDFs' skewness, (b) Absolute deviation of PDFs' skewness from dataset's skewness, (c) PDF's excess-kurtosis, (d) Absolute deviation of PDFs' excess-kurtosis from dataset's excess-kurtosis. (e) PDFs' third central-moment, (f) Absolute deviation of PDFs' third central-moment from dataset's third central-moment, (g) PDFs' fourth central-moment, (h) Absolute deviation of PDFs' fourth central-moment from dataset's fourth central-moment, (i) PDFs' fourth cumulant, (j) Absolute deviation of PDFs' fourth cumulant from dataset's fourth cumulant.

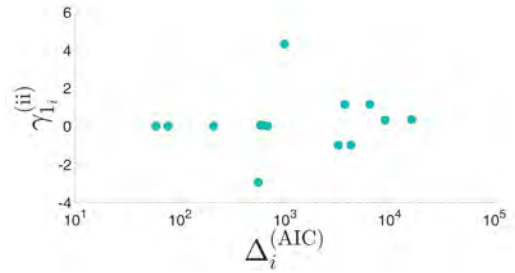

(a) $\gamma_{1_i}^{(\mathrm{params})}$

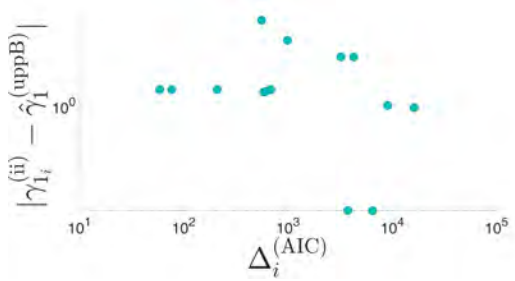

(b) $|\gamma_{1_i}^{(\mathrm{params})} - \hat{\gamma}_1^{(\mathrm{data})}|$

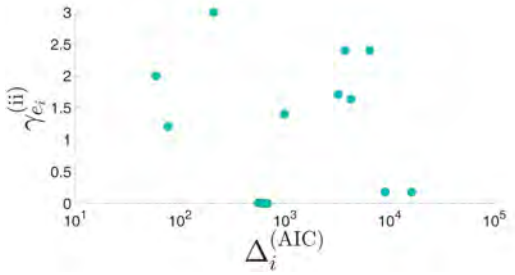

(c) $\gamma_{e_i}^{(\mathrm{params})}$

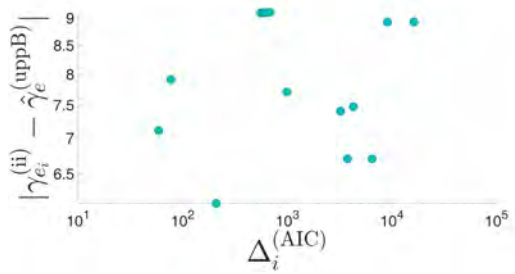

(d) $|\gamma_{e_i}^{(\mathrm{params})} - \hat{\gamma}_e^{(\mathrm{data})}|$

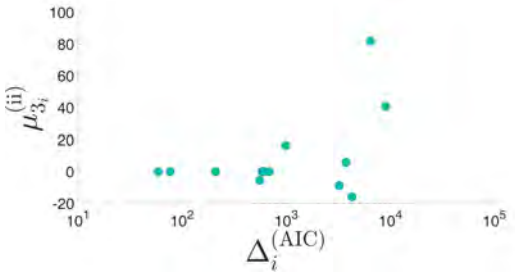

(e) $\mu_{3_i}^{(\mathrm{params})}$

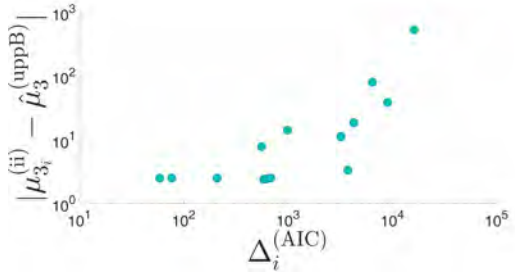

(f) $|\mu_{3_i}^{(\mathrm{params})} - \hat{\mu}_3^{(\mathrm{data})}|$

Sub-figures continue on the next page.

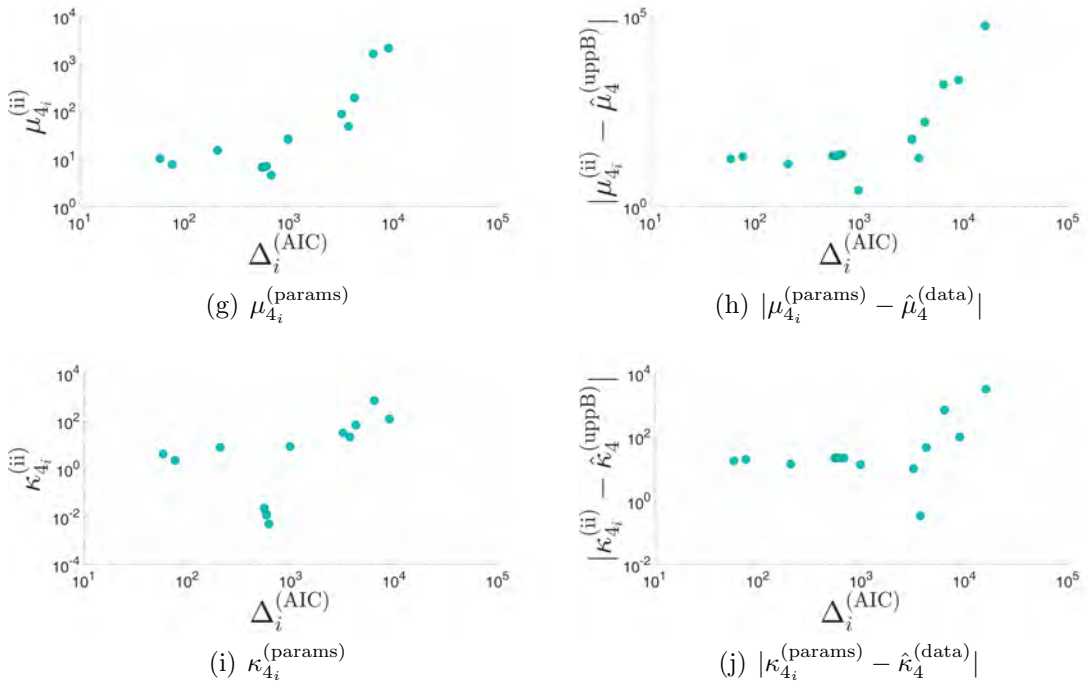

(g) $\mu_{4_i}^{(\mathrm{params})}$ (h) $|\mu_{4_i}^{(\mathrm{params})} - \hat{\mu}_4^{(\mathrm{data})}|$

(i) $\kappa_{4_i}^{(\mathrm{params})}$ (j) $|\kappa_{4_i}^{(\mathrm{params})} - \hat{\kappa}_4^{(\mathrm{data})}|$

Figure H.2: (37/F dataset (b)) The scatter plots with no monotonic trend at $\alpha = 0.01$. (a) PDFs' skewness, (b) Absolute deviation of PDFs' skewness from dataset's skewness, (c) PDF's excess-kurtosis, (d) Absolute deviation of PDFs' excess-kurtosis from dataset's excess-kurtosis. (e) PDFs' third central-moment, (f) Absolute deviation of PDFs' third central-moment from dataset's third central-moment, (g) PDFs' fourth central-moment, (h) Absolute deviation of PDFs' fourth central-moment from dataset's fourth central-moment, (i) PDFs' fourth cumulant, (j) Absolute deviation of PDFs' fourth cumulant from dataset's fourth cumulant.

H.2 For 3-parameter PDFs

Table H.2: $\hat{\rho}_{\Delta,y}$ and p-value of the Spearman's rank correlation significance test. The corresponding scatter graphs for 37/F dataset (a) are shown in Figure H.3. The corresponding scatter graphs for 37/F dataset (b) are shown in Figure H.4. See Section 4.5.1 for the symbols used in this table.

Ordinate, y	37/F dataset (a) $\hat{\rho}_{\Delta,y}$ (p-value)	37/F dataset (b) $\hat{\rho}_{\Delta,y}$ (p-value)
$\mu_{2_i}^{(\text{iii})}$	0.339 (0.098)	0.38 (0.056)
$\lvert\mu_{2_i}^{(\text{iii})} - \hat{\mu}_2^{(\text{data})}\rvert$	0.119 (0.578)	-0.018 (0.933)
$\gamma_{1_i}^{(\text{params})}$	0.67 (0)	0.228 (0.283)
$\lvert\gamma_{1_i}^{(\text{params})} - \hat{\gamma}_1^{(\text{data})}\rvert$	-0.637 (0.001)	-0.228 (0.283)
$\gamma_{e_i}^{(\text{params})}$	-0.341 (0.141)	-0.392 (0.08)
$\lvert\gamma_{e_i}^{(\text{params})} - \hat{\gamma}_e^{(\text{data})}\rvert$	0.321 (0.156)	0.405 (0.07)
$\mu_{3_i}^{(\text{params})}$	0.679 (0)	0.2 (0.337)
$\lvert\mu_{3_i}^{(\text{params})} - \hat{\mu}_3^{(\text{data})}\rvert$	-0.437 (0.033)	0.012 (0.956)
$\mu_{4_i}^{(\text{params})}$	-0.116 (0.607)	-0.217 (0.306)
$\lvert\mu_{4_i}^{(\text{params})} - \hat{\mu}_4^{(\text{data})}\rvert$	0.106 (0.621)	0.208 (0.316)
$\kappa_{4_i}^{(\text{params})}$	-0.358 (0.111)	-0.505 (0.015)
$\lvert\kappa_{4_i}^{(\text{params})} - \hat{\kappa}_4^{(\text{data})}\rvert$	0.347 (0.097)	0.452 (0.025)

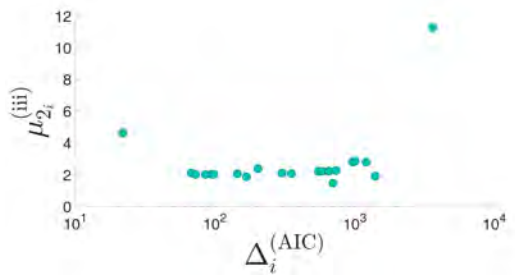

(a) $\mu_{2_i}^{(\text{params})}$

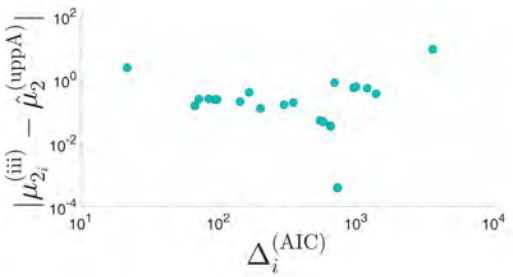

(b) $|\mu_{2_i}^{(\text{params})} - \hat{\mu}_2^{(\text{data})}|$

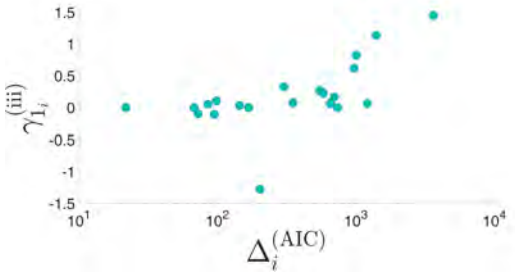

(c) $\gamma_{1_i}^{(\text{params})}$

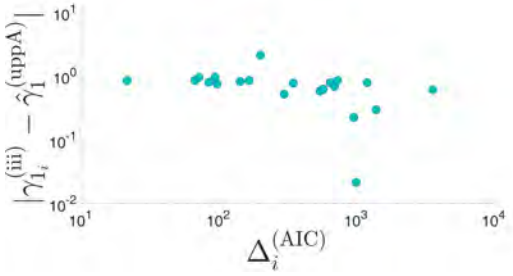

(d) $|\gamma_{1_i}^{(\text{params})} - \hat{\gamma}_1^{(\text{data})}|$

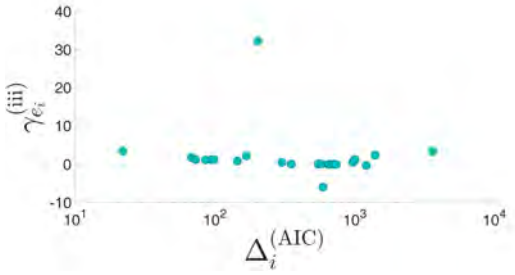

(e) $\gamma_{e_i}^{(\text{params})}$

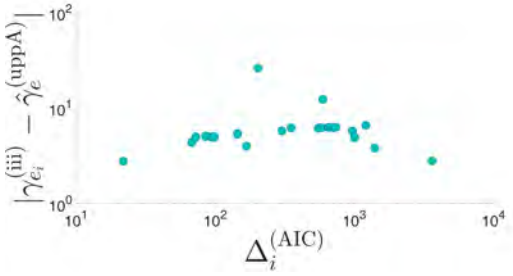

(f) $|\gamma_{e_i}^{(\text{params})} - \hat{\gamma}_e^{(\text{data})}|$

Sub-figures continue on the next page.

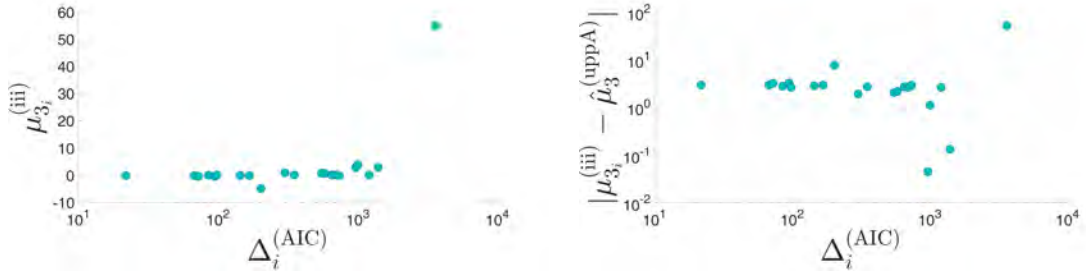

(g) $\mu_{3_i}^{(\mathrm{params})}$ (h) $|\mu_{3_i}^{(\mathrm{params})} - \hat{\mu}_3^{(\mathrm{data})}|$

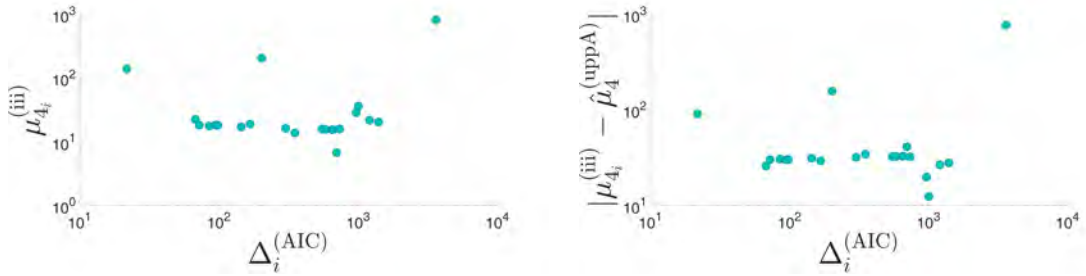

(i) $\mu_{4_i}^{(\mathrm{params})}$ (j) $|\mu_{4_i}^{(\mathrm{params})} - \hat{\mu}_4^{(\mathrm{data})}|$

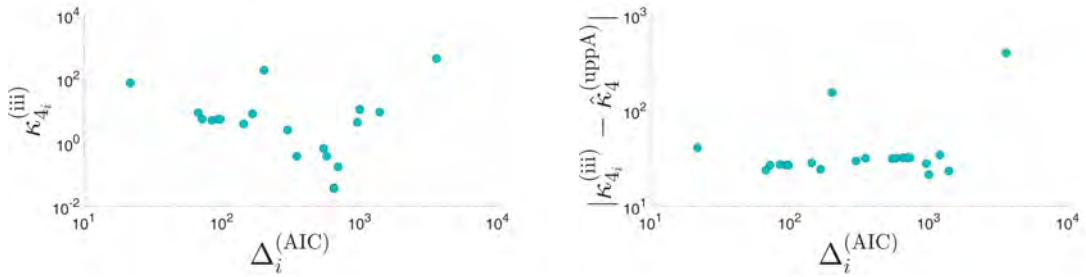

(k) $\kappa_{4_i}^{(\mathrm{params})}$ (l) $|\kappa_{4_i}^{(\mathrm{params})} - \hat{\kappa}_4^{(\mathrm{data})}|$

Figure H.3: (37/F dataset (a)) The scatter plots with no monotonic trend at $\alpha = 0.01$. (a) PDFs' variance, (b) Absolute deviation of PDFs' variance from dataset's variance, (c) PDFs' skewness, (d) Absolute deviation of PDFs' skewness from dataset's skewness, (e) PDF's excess-kurtosis, (f) Absolute deviation of PDFs' excess-kurtosis from dataset's excess-kurtosis. (g) PDFs' third central-moment, (h) Absolute deviation of PDFs' third central-moment from dataset's third central-moment, (i) PDFs' fourth central-moment, (j) Absolute deviation of PDFs' fourth central-moment from dataset's fourth central-moment, (k) PDFs' fourth cumulant, (l) Absolute deviation of PDFs' fourth cumulant from dataset's fourth cumulant.

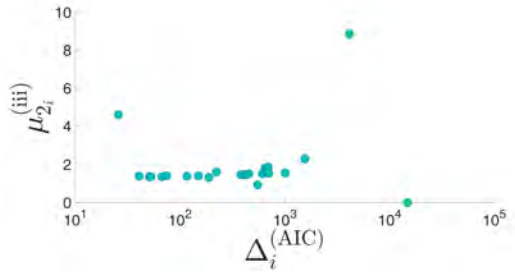

(a) $\mu_{2_i}^{(\mathrm{params})}$

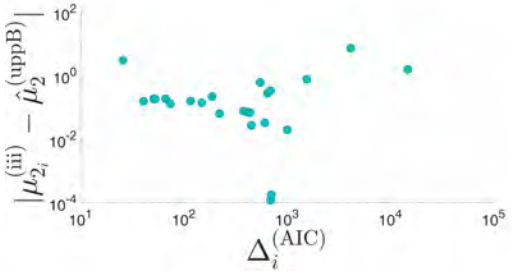

(b) $|\mu_{2_i}^{(\mathrm{params})} - \hat{\mu}_2^{(\mathrm{data})}|$

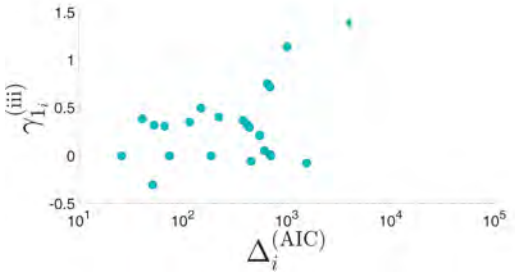

(c) $\gamma_{1_i}^{(\mathrm{params})}$

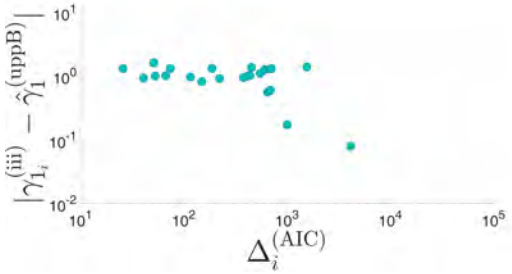

(d) $|\gamma_{1_i}^{(\mathrm{params})} - \hat{\gamma}_1^{(\mathrm{data})}|$

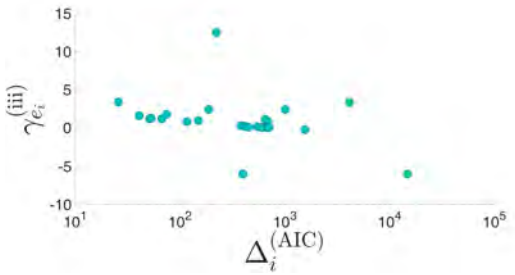

(e) $\gamma_{e_i}^{(\mathrm{params})}$

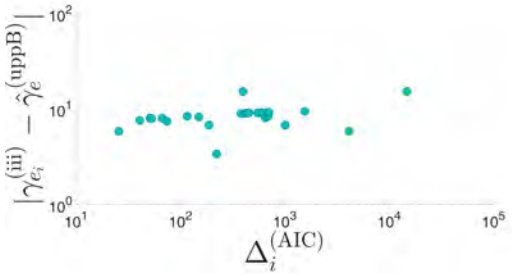

(f) $|\gamma_{e_i}^{(\mathrm{params})} - \hat{\gamma}_e^{(\mathrm{data})}|$

Sub-figures continue on the next page.

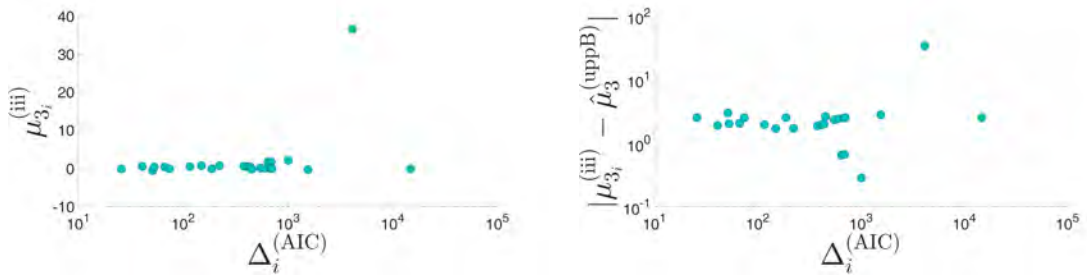

(g) $\mu_{3_i}^{(\mathrm{params})}$

(h) $|\mu_{3_i}^{(\mathrm{params})} - \hat{\mu}_3^{(\mathrm{data})}|$

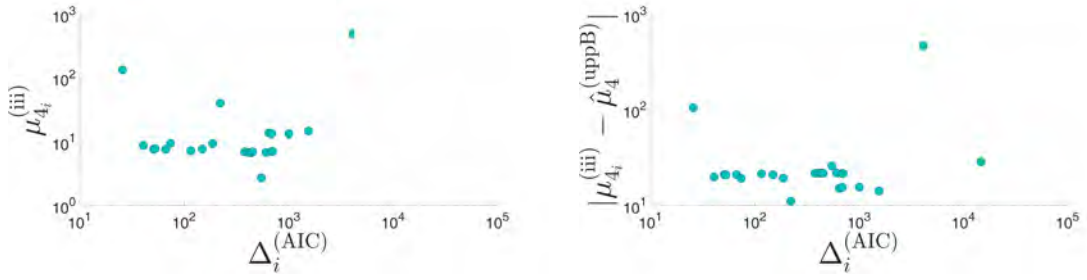

(i) $\mu_{4_i}^{(\mathrm{params})}$

(j) $|\mu_{4_i}^{(\mathrm{params})} - \hat{\mu}_4^{(\mathrm{data})}|$

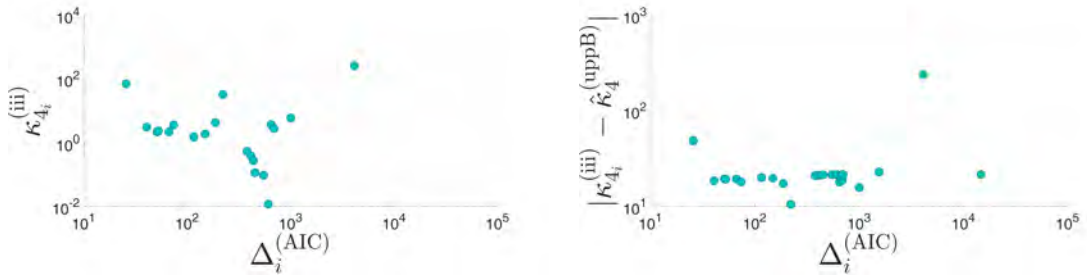

(k) $\kappa_{4_i}^{(\mathrm{params})}$

(l) $|\kappa_{4_i}^{(\mathrm{params})} - \hat{\kappa}_4^{(\mathrm{data})}|$

Figure H.4: (37/F dataset (b)) The scatter plots with no monotonic trend at $\alpha = 0.01$. (a) PDFs' variance, (b) Absolute deviation of PDFs' variance from dataset's variance, (c) PDFs' skewness, (d) Absolute deviation of PDFs' skewness from dataset's skewness, (e) PDF's excess-kurtosis, (f) Absolute deviation of PDFs' excess-kurtosis from dataset's excess-kurtosis. (g) PDFs' third central-moment, (h) Absolute deviation of PDFs' third central-moment from dataset's third central-moment, (i) PDFs' fourth central-moment, (j) Absolute deviation of PDFs' fourth central-moment from dataset's fourth central-moment, (k) PDFs' fourth cumulant, (l) Absolute deviation of PDFs' fourth cumulant from dataset's fourth cumulant.

H.3 For 4-parameter PDFs

Table H.3: $\hat{\rho}_{\Delta,y}$ and p-value of the Spearman's rank correlation significance test. The corresponding scatter graphs for 37/F dataset (a) are shown in Figure H.5. The corresponding scatter graphs for 37/F dataset (b) are shown in Figure H.6. See Section 4.5.1 for the symbols used in this table.

Ordinate, y	37/F dataset (a) $\hat{\rho}_{\Delta,y}$ (p-value)	37/F dataset (b) $\hat{\rho}_{\Delta,y}$ (p-value)
$\mu_{2_i}^{(\text{iv})}$	-0.077 (0.807)	0.055 (0.863)
$\lvert\mu_{2_i}^{(\text{iv})} - \hat{\mu}_2^{(\text{data})}\rvert$	0.363 (0.224)	0.231 (0.448)
$\gamma_{1_i}^{(\text{params})}$	0.505 (0.081)	-0.242 (0.426)
$\lvert\gamma_{1_i}^{(\text{params})} - \hat{\gamma}_1^{(\text{data})}\rvert$	-0.505 (0.081)	-0.187 (0.541)
$\mu_{3_i}^{(\text{params})}$	0.478 (0.101)	-0.121 (0.696)
$\lvert\mu_{3_i}^{(\text{params})} - \hat{\mu}_3^{(\text{data})}\rvert$	-0.478 (0.101)	-0.308 (0.306)
$\mu_{4_i}^{(\text{params})}$	-0.624 (0.06)	-0.252 (0.43)
$\lvert\mu_{4_i}^{(\text{params})} - \hat{\mu}_4^{(\text{data})}\rvert$	0.469 (0.127)	0.252 (0.43)
$\kappa_{4_i}^{(\text{params})}$	-0.633 (0.076)	-0.308 (0.331)
$\lvert\kappa_{4_i}^{(\text{params})} - \hat{\kappa}_4^{(\text{data})}\rvert$	0.357 (0.256)	0.308 (0.331)
$\mathcal{P}_i^{(\text{iv})}$	-0.2 (0.492)	-0.662 (0.012)
$\lvert\mathcal{P}_i^{(\text{iv})} - \hat{\mathcal{P}}^{(\text{data})}\rvert$	0.2 (0.492)	-0.147 (0.616)

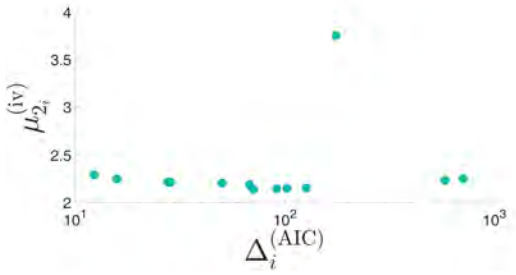

(a) $\mu_{2_i}^{(\mathrm{params})}$

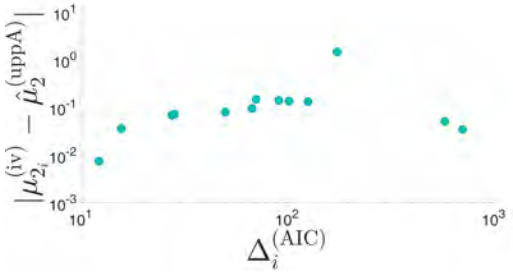

(b) $|\mu_{2_i}^{(\mathrm{params})} - \hat{\mu}_2^{(\mathrm{data})}|$

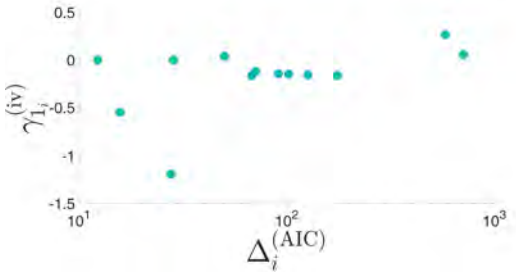

(c) $\gamma_{1_i}^{(\mathrm{params})}$

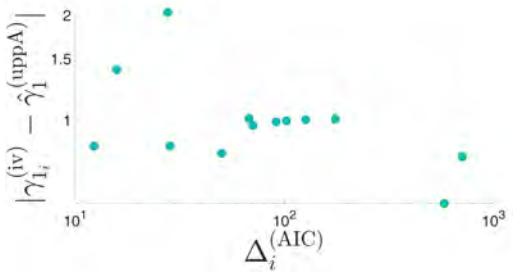

(d) $|\gamma_{1_i}^{(\mathrm{params})} - \hat{\gamma}_1^{(\mathrm{data})}|$

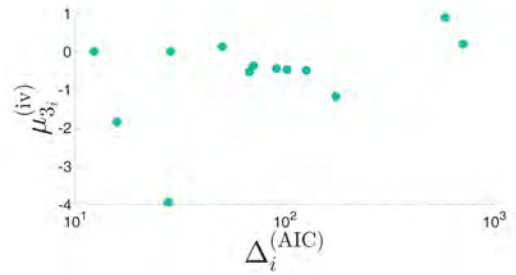

(e) $\mu_{3_i}^{(\mathrm{params})}$

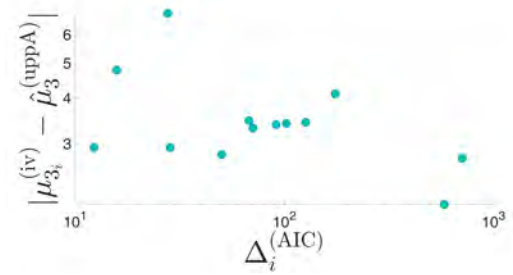

(f) $|\mu_{3_i}^{(\mathrm{params})} - \hat{\mu}_3^{(\mathrm{data})}|$

Sub-figures continue on the next page.

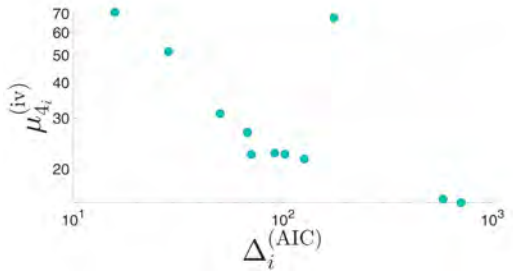

(g) $\mu_{4_i}^{(\mathrm{params})}$

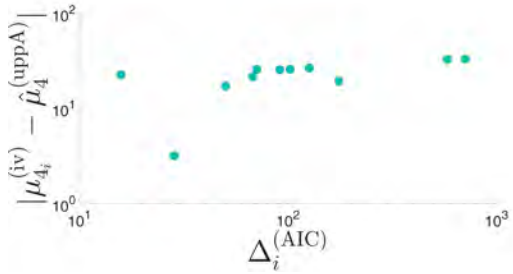

(h) $|\mu_{4_i}^{(\mathrm{params})} - \hat{\mu}_4^{(\mathrm{data})}|$

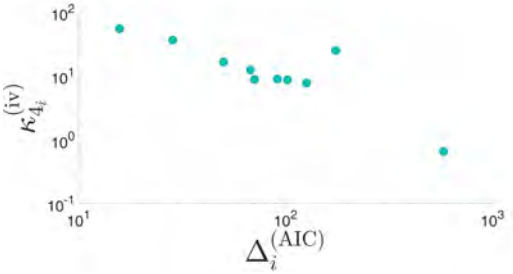

(i) $\kappa_{4_i}^{(\mathrm{params})}$

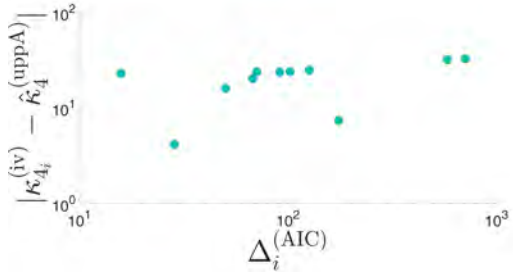

(j) $|\kappa_{4_i}^{(\mathrm{params})} - \hat{\kappa}_4^{(\mathrm{data})}|$

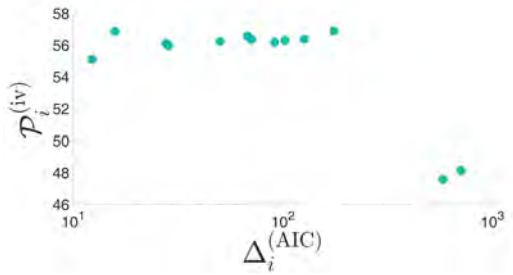

(k) $\mathcal{P}_i^{(\mathrm{params})}$

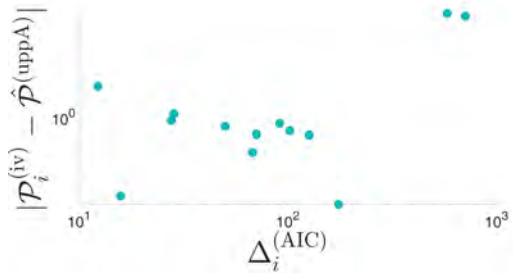

(l) $|\mathcal{P}_i^{(\mathrm{params})} - \hat{\mathcal{P}}^{(\mathrm{data})}|$

Figure H.5: (37/F dataset (a)) The scatter plots with no monotonic trend at $\alpha = 0.01$. (a) PDFs' variance, (b) Absolute deviation of PDFs' variance from dataset's variance, (c) PDFs' skewness, (d) Absolute deviation of PDFs' skewness from dataset's skewness, (e) PDFs' third central-moment, (f) Absolute deviation of PDFs' third central-moment from dataset's third central-moment, (g) PDFs' fourth central-moment, (h) Absolute deviation of PDFs' fourth central-moment from dataset's fourth central-moment, (i) PDFs' fourth cumulant, (j) Absolute deviation of PDFs' fourth cumulant from dataset's fourth cumulant. (k) PDFs' peakedness, (l) Absolute deviation of PDFs' peakedness from dataset's peakedness.

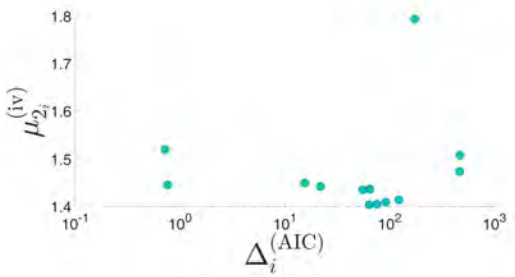

(a) $\mu_{2_i}^{(\mathrm{params})}$

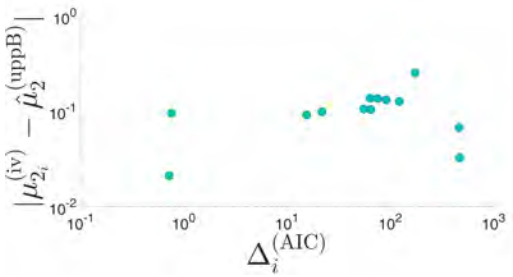

(b) $|\mu_{2_i}^{(\mathrm{params})} - \hat{\mu}_2^{(\mathrm{data})}|$

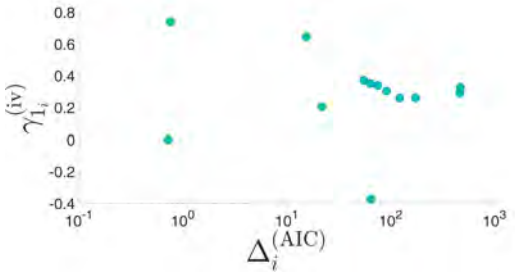

(c) $\gamma_{1_i}^{(\mathrm{params})}$

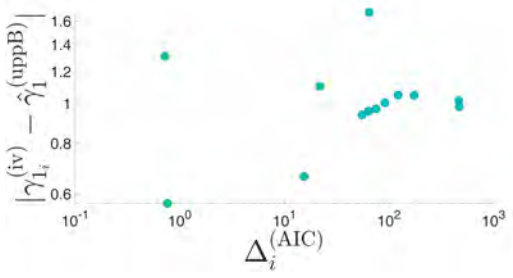

(d) $|\gamma_{1_i}^{(\mathrm{params})} - \hat{\gamma}_1^{(\mathrm{data})}|$

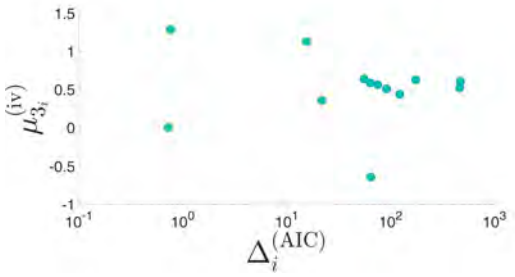

(e) $\mu_{3_i}^{(\mathrm{params})}$

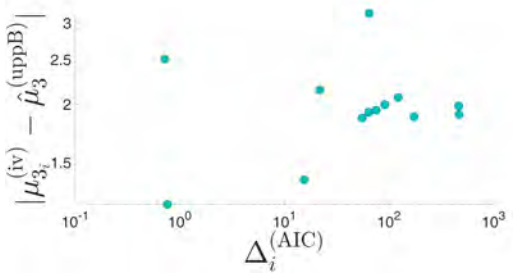

(f) $|\mu_{3_i}^{(\mathrm{params})} - \hat{\mu}_3^{(\mathrm{data})}|$

Sub-figures continue on the next page.

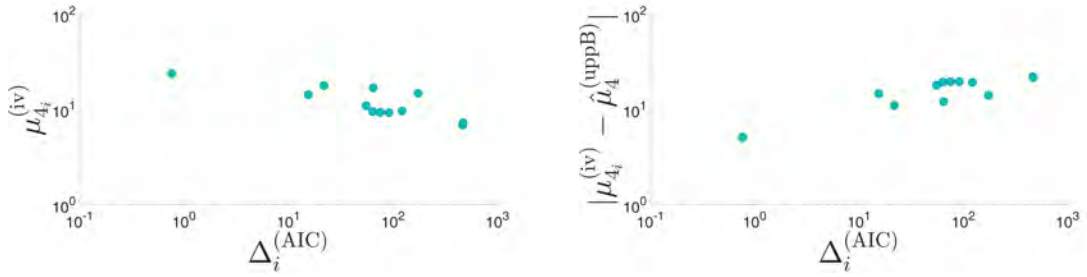

(g) $\mu_{4_i}^{(\mathrm{params})}$ (h) $|\mu_{4_i}^{(\mathrm{params})} - \hat{\mu}_4^{(\mathrm{data})}|$

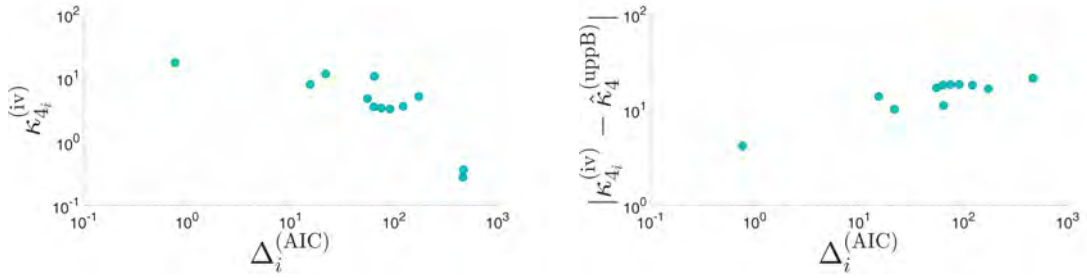

(i) $\kappa_{4_i}^{(\mathrm{params})}$ (j) $|\kappa_{4_i}^{(\mathrm{params})} - \hat{\kappa}_4^{(\mathrm{data})}|$

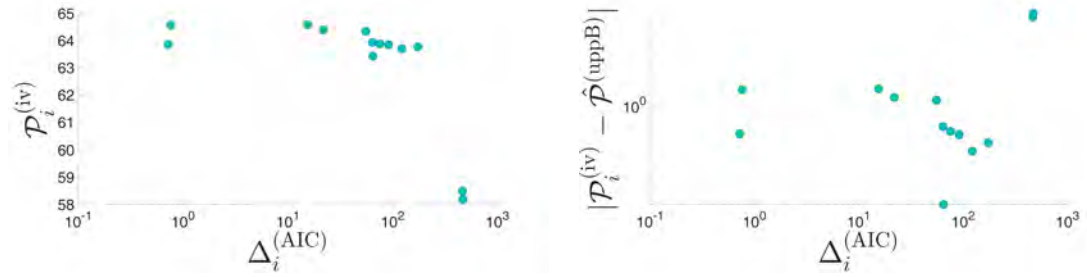

(k) $\mathcal{P}_i^{(\mathrm{params})}$ (l) $|\mathcal{P}_i^{(\mathrm{params})} - \hat{\mathcal{P}}^{(\mathrm{data})}|$

Figure H.6: (37/F dataset (b)) The scatter plots with no monotonic trend at $\alpha = 0.01$. (a) PDFs' variance, (b) Absolute deviation of PDFs' variance from dataset's variance, (c) PDFs' skewness, (d) Absolute deviation of PDFs' skewness from dataset's skewness, (e) PDFs' third central-moment, (f) Absolute deviation of PDFs' third central-moment from dataset's third central-moment, (g) PDFs' fourth central-moment, (h) Absolute deviation of PDFs' fourth central-moment from dataset's fourth central-moment, (i) PDFs' fourth cumulant, (j) Absolute deviation of PDFs' fourth cumulant from dataset's fourth cumulant. (k) PDFs' peakedness, (l) Absolute deviation of PDFs' peakedness from dataset's peakedness.

Appendix I

(19/F and 25/F datasets) Scatter-plots of $\Delta_i^{(\mathrm{AIC})}$ vs y (Section 4.5.1) with no monotonic trend

This appendix shows the results of Spearman's rank correlation significance test of $\Delta_i^{(\mathrm{AIC})}$ vs y (Section 4.5.1) with no significant monotonic trend at $\alpha = 0.01$: Section I.1 for 2-parameter PDFs, Section I.2 for 3-parameter PDFs, and Section I.3 for 4-parameter PDFs.

I.1 For 2-parameter PDFs

Table I.1: $\hat{\rho}_{\Delta,y}$ and p-value of the Spearman's rank correlation significance test. The corresponding scatter graphs for 19/F dataset are shown in Figure I.1. The corresponding scatter graphs for 25/F dataset are shown in Figure I.2. See Section 4.5.1 for the symbols used in this table.

Ordinate, y	19/F dataset $\hat{\rho}_{\Delta,y}$ (p-value)	25/F dataset $\hat{\rho}_{\Delta,y}$ (p-value)
$\gamma_{1_i}^{(\text{params})}$	0.537 (0.039)	0.531 (0.034)
$\lvert\gamma_{1_i}^{(\text{params})} - \hat{\gamma}_1^{(\text{data})}\rvert$	0.829 (0)	0.794 (0)
$\gamma_{e_i}^{(\text{params})}$	0.09 (0.762)	0.086 (0.773)
$\lvert\gamma_{e_i}^{(\text{params})} - \hat{\gamma}_e^{(\text{data})}\rvert$	-0.037 (0.904)	-0.081 (0.785)
$\mu_{3_i}^{(\text{params})}$	0.373 (0.209)	0.371 (0.192)
$\lvert\mu_{3_i}^{(\text{params})} - \hat{\mu}_3^{(\text{data})}\rvert$	0.926 (0)	0.925 (0)
$\mu_{4_i}^{(\text{params})}$	-0.017 (0.982)	-0.017 (0.982)
$\lvert\mu_{4_i}^{(\text{params})} - \hat{\mu}_4^{(\text{data})}\rvert$	0.857 (0)	0.857 (0)
$\kappa_{4_i}^{(\text{params})}$	-0.017 (0.982)	0.248 (0.492)
$\lvert\kappa_{4_i}^{(\text{params})} - \hat{\kappa}_4^{(\text{data})}\rvert$	0.857 (0)	0.846 (0)

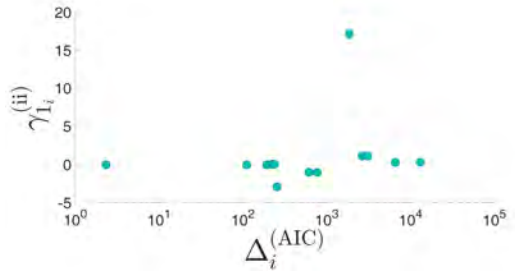

(a) $\gamma_{1_i}^{(\mathrm{params})}$

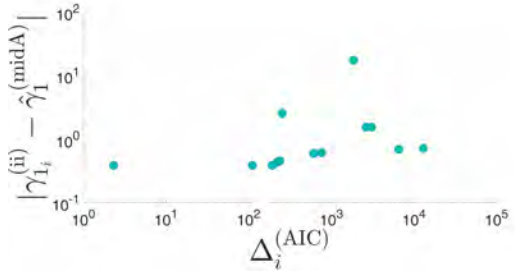

(b) $|\gamma_{1_i}^{(\mathrm{params})} - \hat{\gamma}_1^{(\mathrm{data})}|$

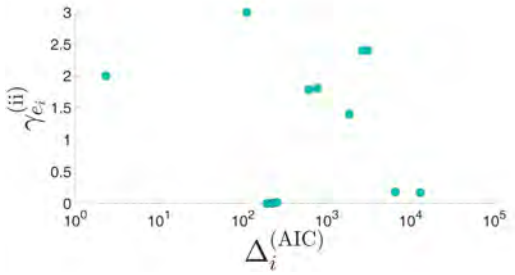

(c) $\gamma_{e_i}^{(\mathrm{params})}$

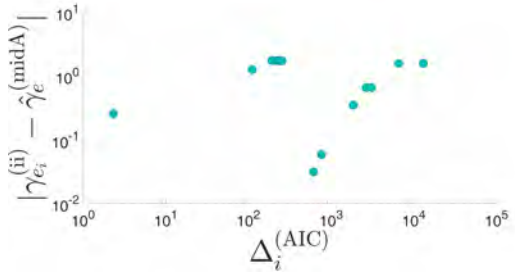

(d) $|\gamma_{e_i}^{(\mathrm{params})} - \hat{\gamma}_e^{(\mathrm{data})}|$

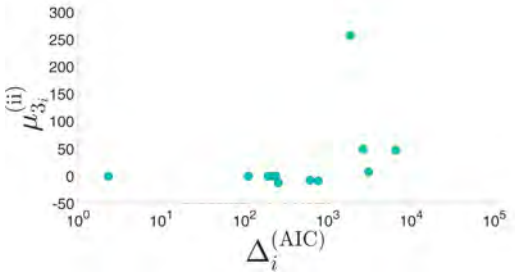

(e) $\mu_{3_i}^{(\mathrm{params})}$

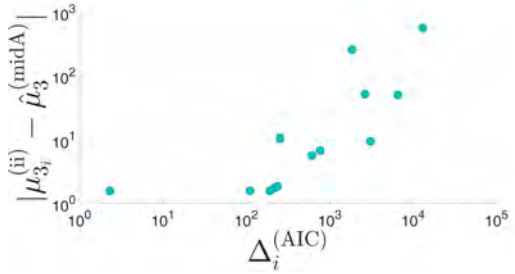

(f) $|\mu_{3_i}^{(\mathrm{params})} - \hat{\mu}_3^{(\mathrm{data})}|$

Sub-figures continue on the next page.

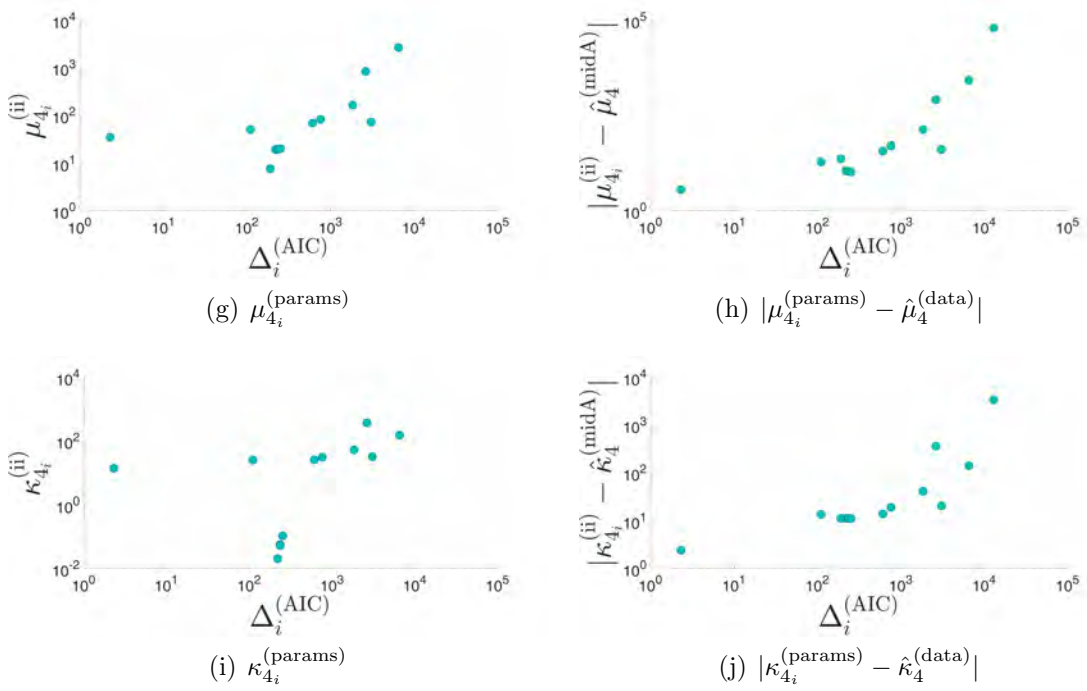

(g) $\mu_{4_i}^{(\mathrm{params})}$ (h) $|\mu_{4_i}^{(\mathrm{params})} - \hat{\mu}_4^{(\mathrm{data})}|$

(i) $\kappa_{4_i}^{(\mathrm{params})}$ (j) $|\kappa_{4_i}^{(\mathrm{params})} - \hat{\kappa}_4^{(\mathrm{data})}|$

Figure I.1: (19/F dataset) The scatter plots with no monotonic trend at $\alpha = 0.01$. (a) PDFs' skewness, (b) Absolute deviation of PDFs' skewness from dataset's skewness, (c) PDF's excess-kurtosis, (d) Absolute deviation of PDFs' excess-kurtosis from dataset's excess-kurtosis. (e) PDFs' third central-moment, (f) Absolute deviation of PDFs' third central-moment from dataset's third central-moment, (g) PDFs' fourth central-moment, (h) Absolute deviation of PDFs' fourth central-moment from dataset's fourth central-moment, (i) PDFs' fourth cumulant, (j) Absolute deviation of PDFs' fourth cumulant from dataset's fourth cumulant.

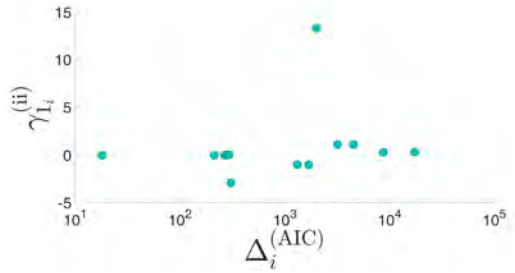

(a) $\gamma_{1_i}^{(\mathrm{params})}$

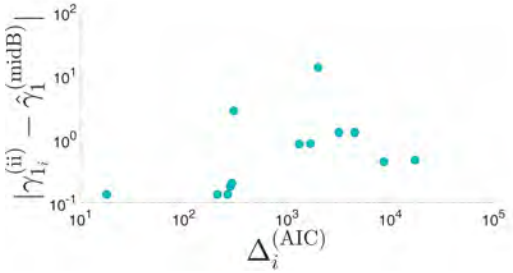

(b) $|\gamma_{1_i}^{(\mathrm{params})} - \hat{\gamma}_1^{(\mathrm{data})}|$

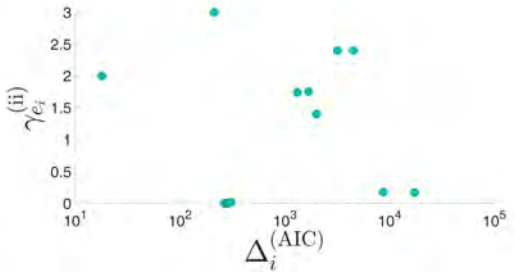

(c) $\gamma_{e_i}^{(\mathrm{params})}$

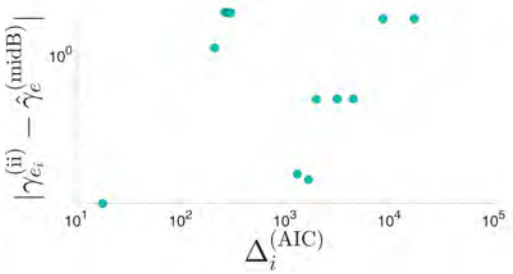

(d) $|\gamma_{e_i}^{(\mathrm{params})} - \hat{\gamma}_e^{(\mathrm{data})}|$

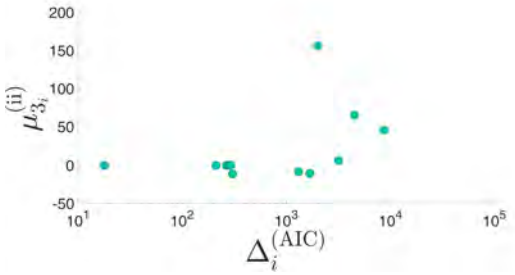

(e) $\mu_{3_i}^{(\mathrm{params})}$

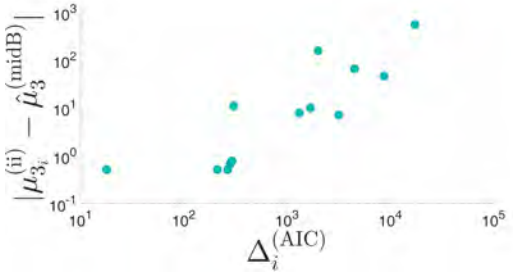

(f) $|\mu_{3_i}^{(\mathrm{params})} - \hat{\mu}_3^{(\mathrm{data})}|$

Sub-figures continue on the next page.

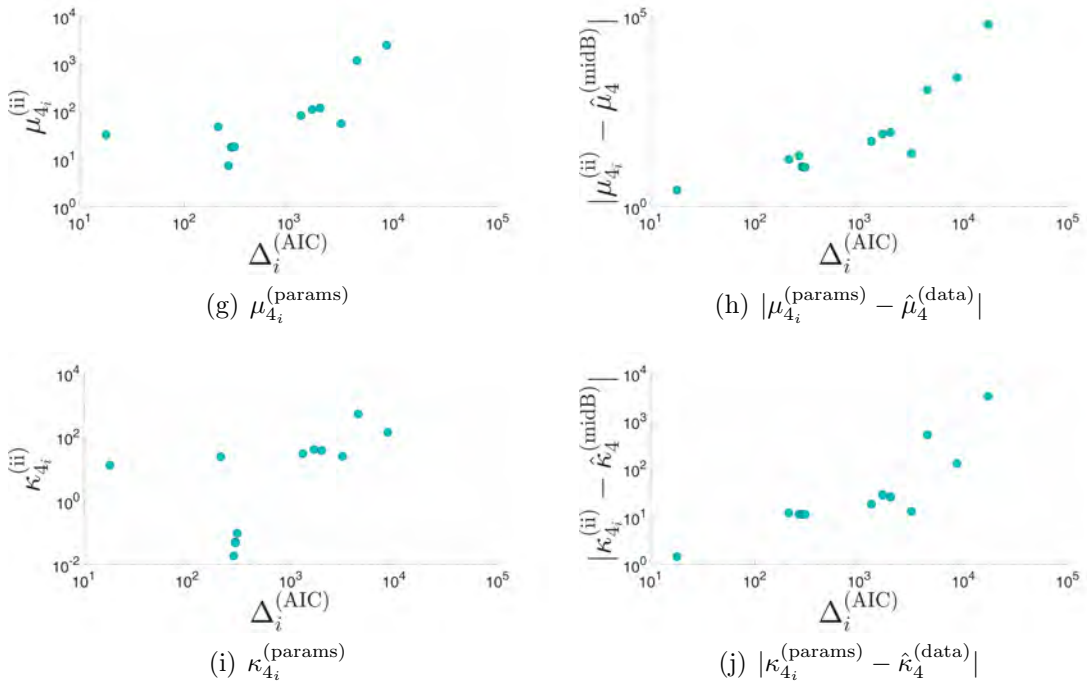

(g) $\mu_{4_i}^{(\mathrm{params})}$ (h) $|\mu_{4_i}^{(\mathrm{params})} - \hat{\mu}_4^{(\mathrm{data})}|$

(i) $\kappa_{4_i}^{(\mathrm{params})}$ (j) $|\kappa_{4_i}^{(\mathrm{params})} - \hat{\kappa}_4^{(\mathrm{data})}|$

Figure I.2: (25/F dataset) The scatter plots with no monotonic trend at $\alpha = 0.01$. (a) PDFs' skewness, (b) Absolute deviation of PDFs' skewness from dataset's skewness, (c) PDF's excess-kurtosis, (d) Absolute deviation of PDFs' excess-kurtosis from dataset's excess-kurtosis. (e) PDFs' third central-moment, (f) Absolute deviation of PDFs' third central-moment from dataset's third central-moment, (g) PDFs' fourth central-moment, (h) Absolute deviation of PDFs' fourth central-moment from dataset's fourth central-moment, (i) PDFs' fourth cumulant, (j) Absolute deviation of PDFs' fourth cumulant from dataset's fourth cumulant.

I.2 For 3-parameter PDFs

Table I.2: $\hat{\rho}_{\Delta,y}$ and p-value of the Spearman's rank correlation significance test. The corresponding scatter graphs for 19/F dataset are shown in Figure I.3. The corresponding scatter graphs for 25/F dataset are shown in Figure I.4. See Section 4.5.1 for the symbols used in this table.

Ordinate, y	19/F dataset $\hat{\rho}_{\Delta,y}$ (p-value)	25/F dataset $\hat{\rho}_{\Delta,y}$ (p-value)
$\mu_{2_i}^{(\text{iii})}$	0.234 (0.25)	0.393 (0.053)
$\lvert\mu_{2_i}^{(\text{iii})} - \hat{\mu}_2^{(\text{data})}\rvert$	0.359 (0.078)	0.208 (0.328)
$\gamma_{1_i}^{(\text{params})}$	0.608 (0.002)	0.66 (0)
$\lvert\gamma_{1_i}^{(\text{params})} - \hat{\gamma}_1^{(\text{data})}\rvert$	0.589 (0.002)	0.531 (0.008)
$\gamma_{e_i}^{(\text{params})}$	-0.188 (0.426)	-0.203 (0.389)
$\lvert\gamma_{e_i}^{(\text{params})} - \hat{\gamma}_e^{(\text{data})}\rvert$	0.47 (0.033)	0.401 (0.072)
$\mu_{3_i}^{(\text{params})}$	0.647 (0)	0.633 (0.001)
$\lvert\mu_{3_i}^{(\text{params})} - \hat{\mu}_3^{(\text{data})}\rvert$	0.657 (0)	0.601 (0.002)
$\mu_{4_i}^{(\text{params})}$	-0.362 (0.089)	-0.292 (0.187)
$\lvert\mu_{4_i}^{(\text{params})} - \hat{\mu}_4^{(\text{data})}\rvert$	0.338 (0.098)	0.233 (0.272)
$\kappa_{4_i}^{(\text{params})}$	-0.654 (0.001)	-0.401 (0.059)
$\lvert\kappa_{4_i}^{(\text{params})} - \hat{\kappa}_4^{(\text{data})}\rvert$	0.582 (0.003)	0.503 (0.013)

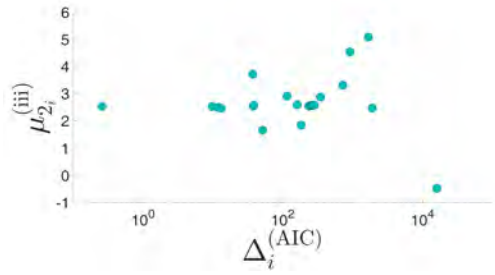

(a) $\mu_{2_i}^{(\text{params})}$

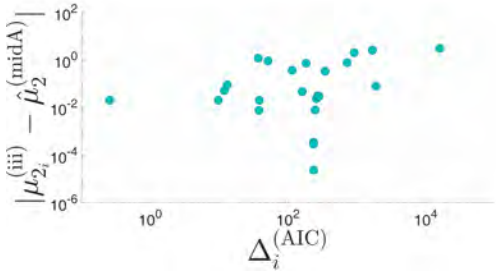

(b) $|\mu_{2_i}^{(\text{params})} - \hat{\mu}_2^{(\text{data})}|$

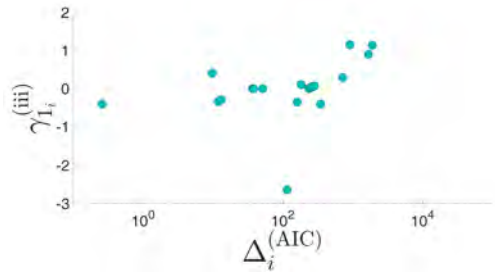

(c) $\gamma_{1_i}^{(\text{params})}$

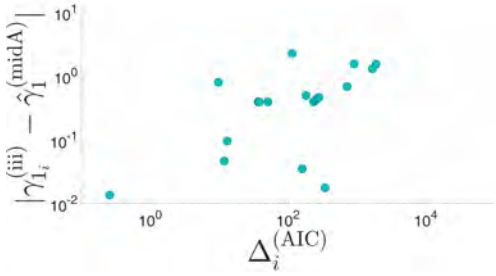

(d) $|\gamma_{1_i}^{(\text{params})} - \hat{\gamma}_1^{(\text{data})}|$

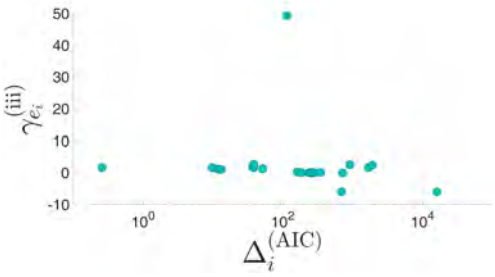

(e) $\gamma_{e_i}^{(\text{params})}$

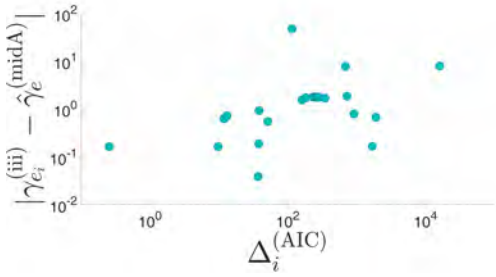

(f) $|\gamma_{e_i}^{(\text{params})} - \hat{\gamma}_e^{(\text{data})}|$

Sub-figures continue on the next page.

(g) $\mu_{3_i}^{(\mathrm{params})}$ (h) $|\mu_{3_i}^{(\mathrm{params})} - \hat{\mu}_3^{(\mathrm{data})}|$

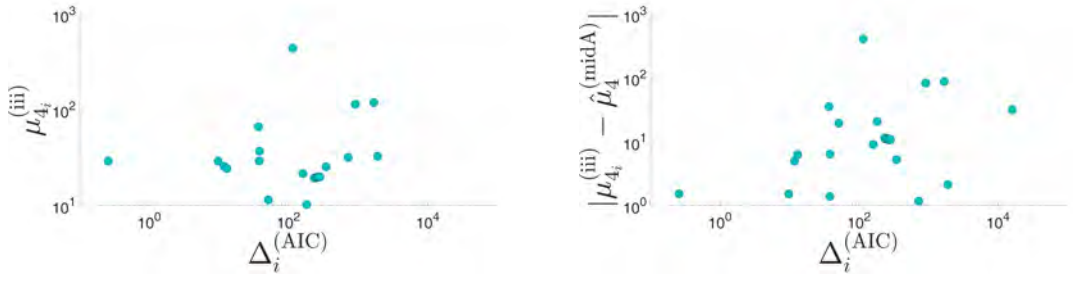

(i) $\mu_{4_i}^{(\mathrm{params})}$ (j) $|\mu_{4_i}^{(\mathrm{params})} - \hat{\mu}_4^{(\mathrm{data})}|$

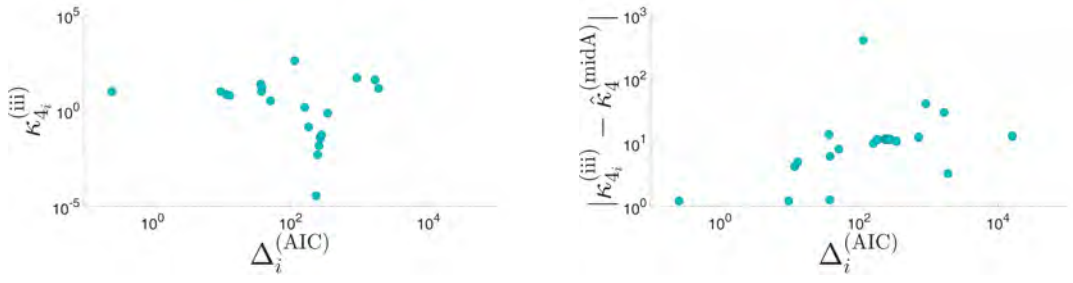

(k) $\kappa_{4_i}^{(\mathrm{params})}$ (l) $|\kappa_{4_i}^{(\mathrm{params})} - \hat{\kappa}_4^{(\mathrm{data})}|$

Figure I.3: (19/F dataset) The scatter plots with no monotonic trend at $\alpha = 0.01$. (a) PDFs' variance, (b) Absolute deviation of PDFs' variance from dataset's variance, (c) PDFs' skewness, (d) Absolute deviation of PDFs' skewness from dataset's skewness, (e) PDF's excess-kurtosis, (f) Absolute deviation of PDFs' excess-kurtosis from dataset's excess-kurtosis. (g) PDFs' third central-moment, (h) Absolute deviation of PDFs' third central-moment from dataset's third central-moment, (i) PDFs' fourth central-moment, (j) Absolute deviation of PDFs' fourth central-moment from dataset's fourth central-moment, (k) PDFs' fourth cumulant, (l) Absolute deviation of PDFs' fourth cumulant from dataset's fourth cumulant.

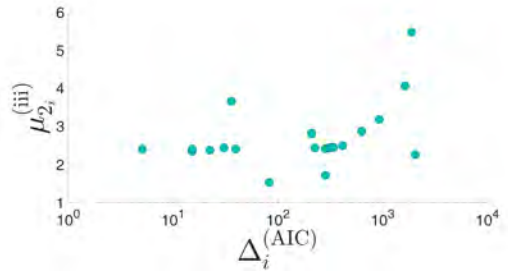

(a) $\mu_{2_i}^{(\mathrm{params})}$

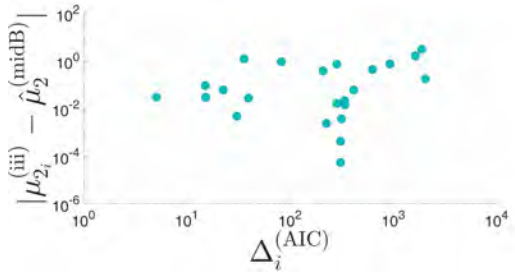

(b) $|\mu_{2_i}^{(\mathrm{params})} - \hat{\mu}_2^{(\mathrm{data})}|$

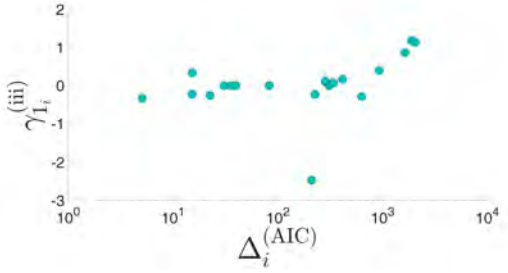

(c) $\gamma_{1_i}^{(\mathrm{params})}$

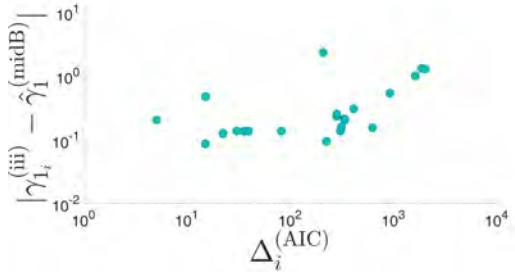

(d) $|\gamma_{1_i}^{(\mathrm{params})} - \hat{\gamma}_1^{(\mathrm{data})}|$

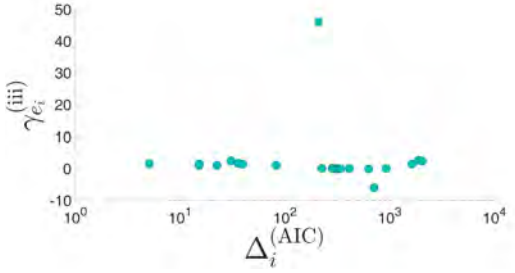

(e) $\gamma_{e_i}^{(\mathrm{params})}$

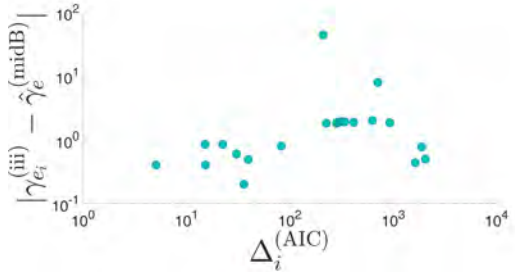

(f) $|\gamma_{e_i}^{(\mathrm{params})} - \hat{\gamma}_e^{(\mathrm{data})}|$

Sub-figures continue on the next page.

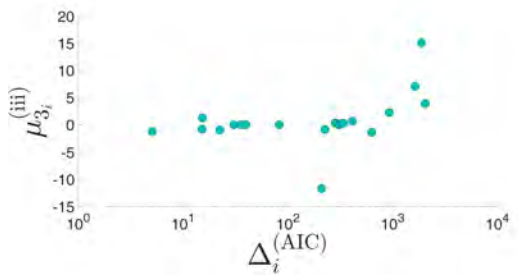

(g) $\mu_{3_i}^{(\mathrm{params})}$

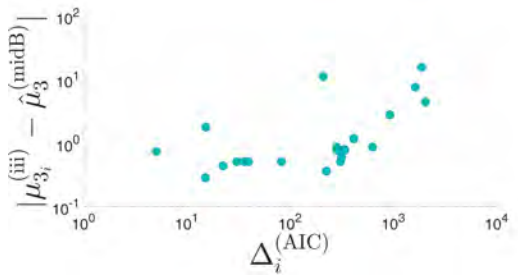

(h) $|\mu_{3_i}^{(\mathrm{params})} - \hat{\mu}_3^{(\mathrm{data})}|$

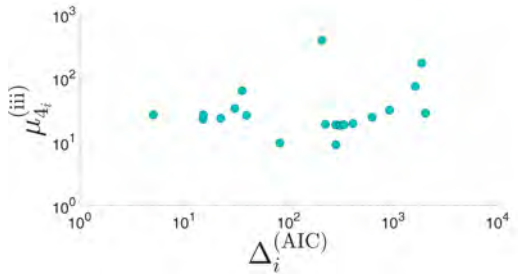

(i) $\mu_{4_i}^{(\mathrm{params})}$

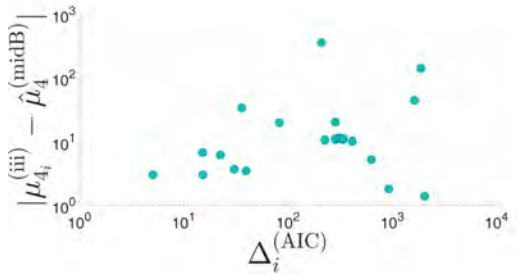

(j) $|\mu_{4_i}^{(\mathrm{params})} - \hat{\mu}_4^{(\mathrm{data})}|$

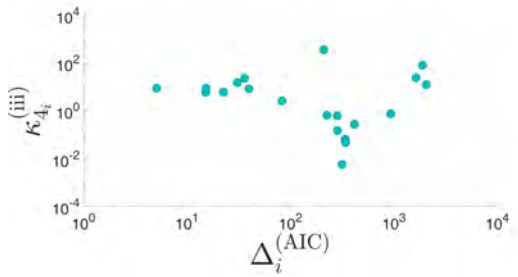

(k) $\kappa_{4_i}^{(\mathrm{params})}$

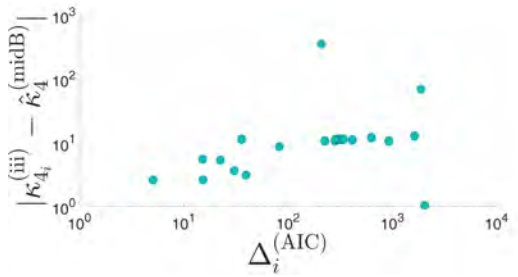

(l) $|\kappa_{4_i}^{(\mathrm{params})} - \hat{\kappa}_4^{(\mathrm{data})}|$

Figure I.4: (25/F dataset) The scatter plots with no monotonic trend at $\alpha = 0.01$. (a) PDFs' variance, (b) Absolute deviation of PDFs' variance from dataset's variance, (c) PDFs' skewness, (d) Absolute deviation of PDFs' skewness from dataset's skewness, (e) PDF's excess-kurtosis, (f) Absolute deviation of PDFs' excess-kurtosis from dataset's excess-kurtosis. (g) PDFs' third central-moment, (h) Absolute deviation of PDFs' third central-moment from dataset's third central-moment, (i) PDFs' fourth central-moment, (j) Absolute deviation of PDFs' fourth central-moment from dataset's fourth central-moment, (k) PDFs' fourth cumulant, (l) Absolute deviation of PDFs' fourth cumulant from dataset's fourth cumulant.

I.3 For 4-parameter PDFs

Table I.3: $\hat{\rho}_{\Delta,y}$ and p-value of the Spearman's rank correlation significance test. The corresponding scatter graphs for 19/F dataset are shown in Figure I.5. The corresponding scatter graphs for 25/F dataset are shown in Figure I.6. See Section 4.5.1 for the symbols used in this table.

Ordinate, y	19/F dataset $\hat{\rho}_{\Delta,y}$ (p-value)	25/F dataset $\hat{\rho}_{\Delta,y}$ (p-value)
$\mu_{2_i}^{(\text{iii})}$	0.489 (0.093)	0 (1)
$\lvert\mu_{2_i}^{(\text{iii})} - \hat{\mu}_2^{(\text{data})}\rvert$	0.588 (0.038)	0.341 (0.255)
$\gamma_{1_i}^{(\text{params})}$	0.363 (0.224)	0.83 (0.001)
$\lvert\gamma_{1_i}^{(\text{params})} - \hat{\gamma}_1^{(\text{data})}\rvert$	0.945 (0)	-0.385 (0.196)
$\gamma_{e_i}^{(\text{params})}$	-0.035 (0.921)	-0.396 (0.182)
$\lvert\gamma_{e_i}^{(\text{params})} - \hat{\gamma}_e^{(\text{data})}\rvert$	0.58 (0.052)	0.022 (0.949)
$\mu_{3_i}^{(\text{params})}$	0.352 (0.239)	0.819 (0.001)
$\lvert\mu_{3_i}^{(\text{params})} - \hat{\mu}_3^{(\text{data})}\rvert$	0.962 (0)	-0.357 (0.232)
$\mu_{4_i}^{(\text{params})}$	-0.209 (0.493)	-0.448 (0.147)
$\lvert\mu_{4_i}^{(\text{params})} - \hat{\mu}_4^{(\text{data})}\rvert$	0.643 (0.021)	0.511 (0.078)
$\kappa_{4_i}^{(\text{params})}$	-0.242 (0.426)	-0.455 (0.14)
$\lvert\kappa_{4_i}^{(\text{params})} - \hat{\kappa}_4^{(\text{data})}\rvert$	0.681 (0.013)	0.484 (0.097)
$\mathcal{P}_i^{(\text{iv})}$	-0.6 (0.026)	-0.068 (0.82)
$\lvert\mathcal{P}_i^{(\text{iv})} - \hat{\mathcal{P}}^{(\text{data})}\rvert$	0.6 (0.026)	0.305 (0.288)

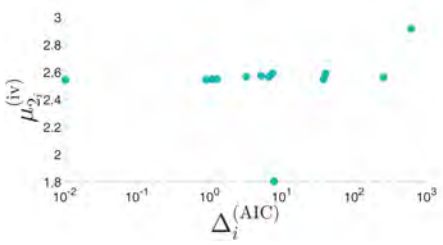

(a) $\mu_{2_i}^{(\mathrm{params})}$

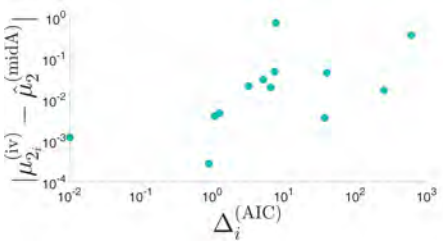

(b) $|\mu_{2_i}^{(\mathrm{params})} - \hat{\mu}_2^{(\mathrm{data})}|$

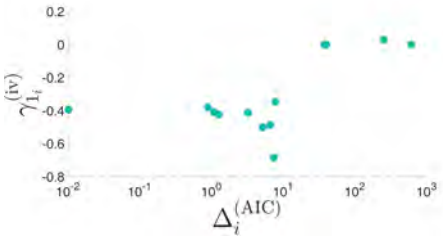

(c) $\gamma_{1_i}^{(\mathrm{params})}$

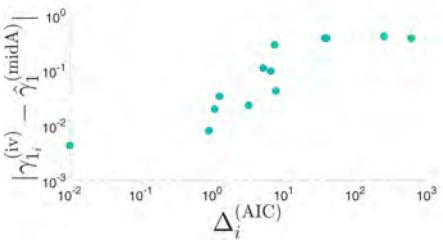

(d) $|\gamma_{1_i}^{(\mathrm{params})} - \hat{\gamma}_1^{(\mathrm{data})}|$

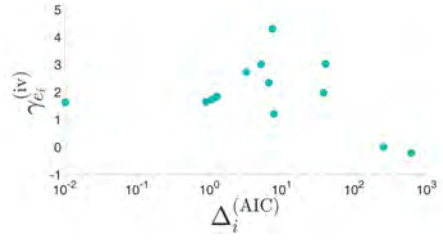

(e) $\gamma_{e_i}^{(\mathrm{params})}$

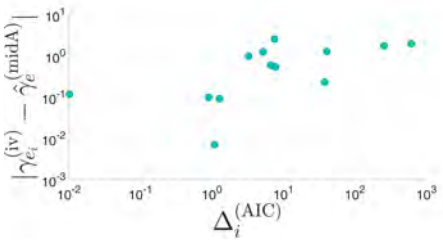

(f) $|\gamma_{e_i}^{(\mathrm{params})} - \hat{\gamma}_e^{(\mathrm{data})}|$

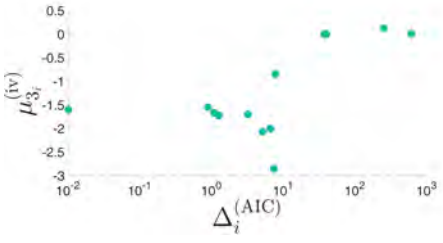

(g) $\mu_{3_i}^{(\mathrm{params})}$

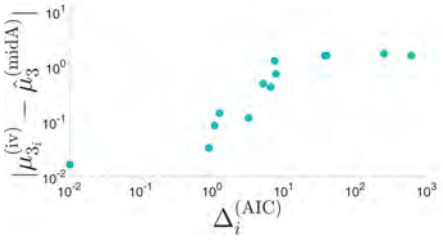

(h) $|\mu_{3_i}^{(\mathrm{params})} - \hat{\mu}_3^{(\mathrm{data})}|$

Sub-figures continue on the next page.

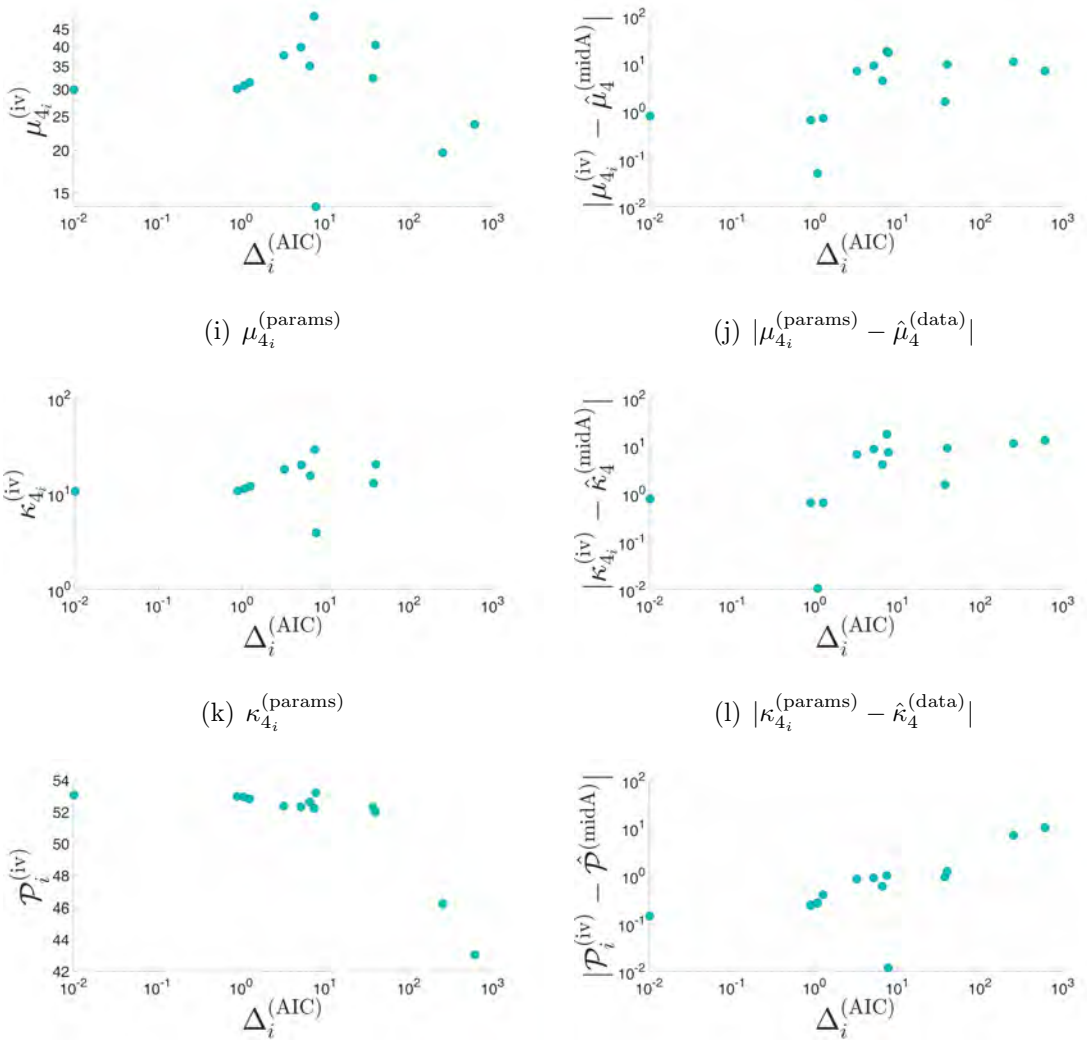

(i) $\mu_{4_i}^{(\mathrm{params})}$

(j) $|\mu_{4_i}^{(\mathrm{params})} - \hat{\mu}_4^{(\mathrm{data})}|$

(k) $\kappa_{4_i}^{(\mathrm{params})}$

(l) $|\kappa_{4_i}^{(\mathrm{params})} - \hat{\kappa}_4^{(\mathrm{data})}|$

(m) $\mathcal{P}_i^{(\mathrm{params})}$

(n) $|\mathcal{P}_i^{(\mathrm{params})} - \hat{\mathcal{P}}^{(\mathrm{data})}|$

Figure I.5: (19/F dataset) The scatter plots with no monotonic trend at $\alpha = 0.01$. (a) PDFs' variance, (b) Absolute deviation of PDFs' variance from dataset's variance, (c) PDFs' skewness, (d) Absolute deviation of PDFs' skewness from dataset's skewness, (e) PDFs' excess-kurtosis, (f) Absolute deviation of PDFs' excess-kurtosis from dataset's excess-kurtosis, (g) PDFs' third central-moment, (h) Absolute deviation of PDFs' third central-moment from dataset's third central-moment, (i) PDFs' fourth central-moment, (j) Absolute deviation of PDFs' fourth central-moment from dataset's fourth central-moment, (k) PDFs' fourth cumulant, (l) Absolute deviation of PDFs' fourth cumulant from dataset's fourth cumulant. (m) PDFs' peakedness, (n) Absolute deviation of PDFs' peakedness from dataset's peakedness.

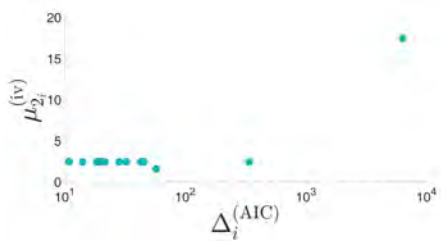

(a) $\mu_{2_i}^{(\mathrm{params})}$

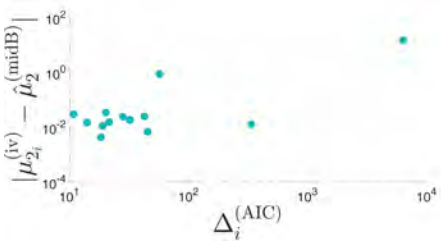

(b) $|\mu_{2_i}^{(\mathrm{params})} - \hat{\mu}_2^{(\mathrm{data})}|$

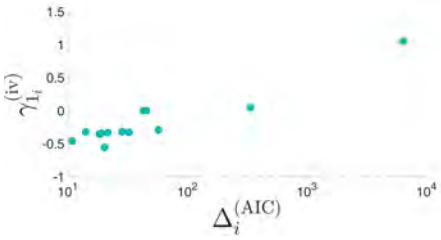

(c) $\gamma_{1_i}^{(\mathrm{params})}$

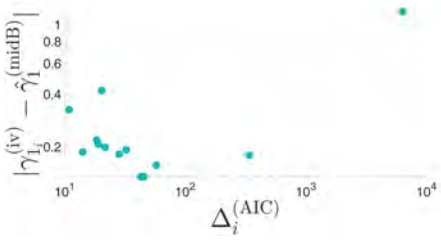

(d) $|\gamma_{1_i}^{(\mathrm{params})} - \hat{\gamma}_1^{(\mathrm{data})}|$

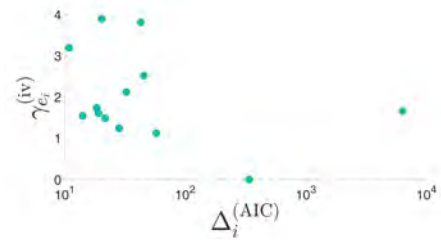

(e) $\gamma_{e_i}^{(\mathrm{params})}$

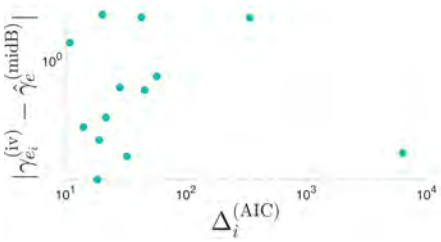

(f) $|\gamma_{e_i}^{(\mathrm{params})} - \hat{\gamma}_e^{(\mathrm{data})}|$

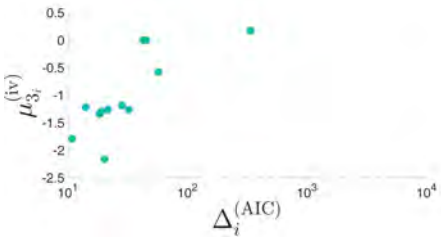

(g) $\mu_{3_i}^{(\mathrm{params})}$

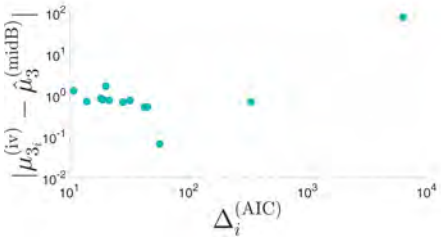

(h) $|\mu_{3_i}^{(\mathrm{params})} - \hat{\mu}_3^{(\mathrm{data})}|$

Sub-figures continue on the next page.

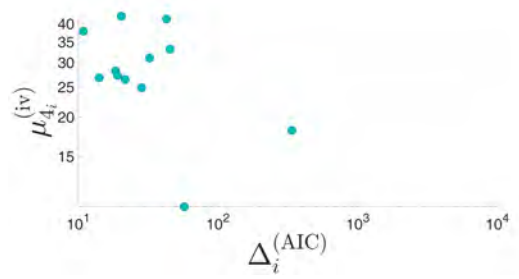

(i) $\mu_{4_i}^{(\mathrm{params})}$

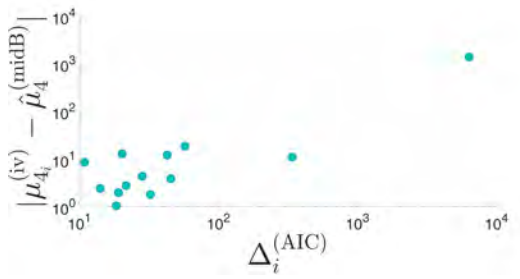

(j) $|\mu_{4_i}^{(\mathrm{params})} - \hat{\mu}_4^{(\mathrm{data})}|$

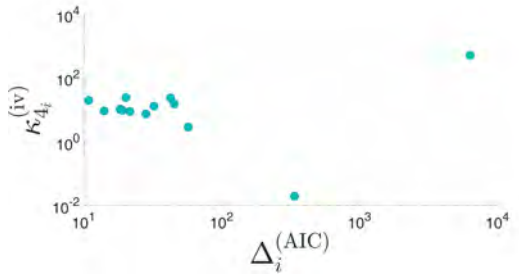

(k) $\kappa_{4_i}^{(\mathrm{params})}$

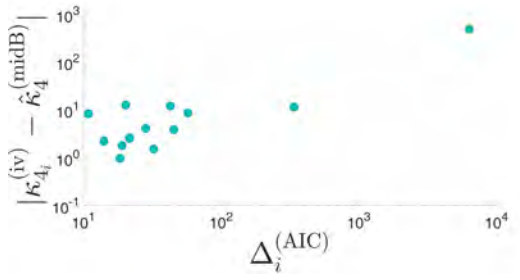

(l) $|\kappa_{4_i}^{(\mathrm{params})} - \hat{\kappa}_4^{(\mathrm{data})}|$

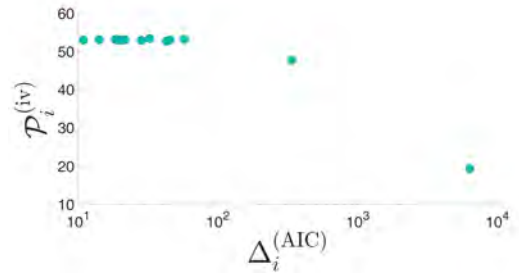

(m) $\mathcal{P}_i^{(\mathrm{params})}$

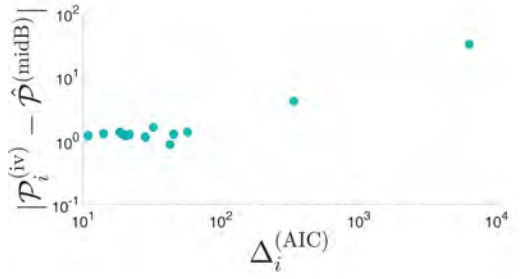

(n) $|\mathcal{P}_i^{(\mathrm{params})} - \hat{\mathcal{P}}^{(\mathrm{data})}|$

Figure I.6: (25/F dataset) The scatter plots with no monotonic trend at $\alpha = 0.01$. (a) PDFs' variance, (b) Absolute deviation of PDFs' variance from dataset's variance, (c) PDFs' skewness, (d) Absolute deviation of PDFs' skewness from dataset's skewness, (e) PDFs' excess-kurtosis, (f) Absolute deviation of PDFs' excess-kurtosis from dataset's excess-kurtosis, (g) PDFs' third central-moment, (h) Absolute deviation of PDFs' third central-moment from dataset's third central-moment, (i) PDFs' fourth central-moment, (j) Absolute deviation of PDFs' fourth central-moment from dataset's fourth central-moment, (k) PDFs' fourth cumulant, (l) Absolute deviation of PDFs' fourth cumulant from dataset's fourth cumulant. (m) PDFs' peakedness, (n) Absolute deviation of PDFs' peakedness from dataset's peakedness.

Appendix J

Mathematical expressions of each PDFs' each scalar

This appendix provides the mathematical expressions of each PDFs' each scalar (listed as (1) to (6) in Section 4.5.1). These scalar metrics are mathematically interrelated [154]:

$$\gamma_1 = \frac{\mu_3}{(\mu_2)^{3/2}}; \tag{J.1}$$

$$\gamma_e = \frac{\mu_4}{(\mu_2)^2} - 3; \tag{J.2}$$

$$\kappa_4 = \mu_4 - 3\mu_2^2. \tag{J.3}$$

The central moments are related to the "raw moments" ("moments taken about zero"), $\mu'_j, j = 1, 2, 3, 4$, as below [154]:

$$\mu_2 = \mu'_2 - {\mu'_1}^2; \tag{J.4}$$

$$\mu_3 = \mu'_3 - 3\mu'_1\mu'_2 + 2{\mu'_1}^3; \tag{J.5}$$

$$\mu_4 = \mu'_4 - 4\mu'_1\mu'_3 + 6{\mu'_1}^2\mu'_2 - 3{\mu'_1}^4. \tag{J.6}$$

Equations (J.1) – (J.6) can be used to calculate all candidate scalar metrics if

(A) the first four raw moments, $\mu'_j, j = 1, 2, 3, 4$, are given only.

(B) the variance (second central-moment) μ_2, the skewness γ_1, and the excess-kurtosis γ_e are given only.

(C) the variance, the third central-moment μ_3, and the fourth central-moment μ_4 are given only.

For calculating peakedness of all candidate PDFs, see Equation 4.15.

(2-parameter PDFs)

Gaussian distribution (N)

$$\mu_2 = b^2; \quad \mu_3 = 0; \quad \mu_4 = 3b^4; \tag{J.7}$$

$$\gamma_1 = \gamma_e = 0; \quad \kappa_4 = 0. \tag{J.8}$$

Logistic distribution (Lg) [126, Chapter 22, Section 4]

$$\mu_2 = \frac{b^2\pi^2}{3}; \qquad \mu_3 = 0; \qquad \mu_4 = 0.467\ b^4\pi^4; \tag{J.9}$$

$$\gamma_1 = 0; \qquad \gamma_e = 1.2; \qquad \kappa_4 = 0.134\ b^4\pi^4. \tag{J.10}$$

Hyperbolic secant distribution (HS) [127, Section 1.3]

$$\mu_2 = \frac{b^2\pi^2}{4}; \qquad \mu_3 = 0; \qquad \mu_4 = 0.3125\ b^4\pi^4; \tag{J.11}$$

$$\gamma_1 = 0; \qquad \gamma_e = 2; \qquad \kappa_4 = 0.1245\ b^4\pi^4. \tag{J.12}$$

Log-logistic distribution (LLg) [133, Section A.2.3.3]

$$\mu_2 = \frac{2\pi a^2}{b}\csc\left(\frac{2\pi}{b}\right) - \frac{\pi^2 a^2}{b^2}\csc\left(\frac{\pi}{b}\right)^2, \quad b > 2; \tag{J.13}$$

$$\mu_3 = \frac{2\pi^3 a^3}{b^3}\csc\left(\frac{\pi}{b}\right)^3 - \frac{6\pi^2 a^3}{b^2}\csc\left(\frac{\pi}{b}\right)\csc\left(\frac{2\pi}{b}\right) + \frac{3\pi a^3}{b}\csc\left(\frac{3\pi}{b}\right), \quad b > 3; \tag{J.14}$$

$$\mu_4 = -\frac{3\pi^4 a^4}{b^4}\csc\left(\frac{\pi}{b}\right)^4 + \frac{12\pi^3 a^4}{b^3}\csc\left(\frac{\pi}{b}\right)^2\csc\left(\frac{2\pi}{b}\right) - \frac{12\pi^2 a^4}{b^2}\csc\left(\frac{\pi}{b}\right)\csc\left(\frac{3\pi}{b}\right) + \frac{4\pi a^4}{b}\csc\left(\frac{4\pi}{b}\right), \quad b > 4. \tag{J.15}$$

Non-central t distribution (nT) [155, Page 466]

$$\mu'_k = \begin{cases} \left(\frac{b}{2}\right)^{\frac{k}{2}} \frac{\Gamma\left(\frac{b-k}{2}\right)}{\Gamma\left(\frac{b}{2}\right)} \exp\left(-\frac{a^2}{2}\right) \frac{d^k}{da^k} \exp\left(\frac{a^2}{2}\right), & \text{if } b > k; \\ \text{does not exist}, & \text{if } b \leq k. \end{cases} \tag{J.16}$$

Location family with standard student's t distribution (T2) [156]

$$\mu_2 = \begin{cases} \frac{b}{b-2}, & \text{if } b > 2; \\ \infty, & \text{if } 1 < b \leq 2; \\ \text{undefined}, & \text{if } b \leq 1. \end{cases} \tag{J.17}$$

$$\mu_3 = 0, \quad \text{if } b > 3. \tag{J.18}$$

$$\mu_4 = \frac{b^2 \left(\frac{6}{b-4} + 3\right)}{(b-2)^2}, \quad \text{if } b > 4. \tag{J.19}$$

$$\gamma_1 = \begin{cases} 0, & \text{if } b > 3; \\ \text{undefined}, & \text{if } b \leq 3. \end{cases} \tag{J.20}$$

$$\gamma_e = \begin{cases} \frac{6}{b-4}, & \text{if } b > 4; \\ \infty, & \text{if } 2 < b \leq 4; \\ \text{undefined}, & \text{if } b \leq 2. \end{cases} \tag{J.21}$$

$$\kappa_4 = \frac{6\, b^2}{(b-2)^2\, (b-4)}, \text{ if } b > 4. \tag{J.22}$$

Log-normal distribution (LN) [133, Section A.5.1.1]

$$\mu_2 = \mathrm{e}^{b^2} - \mathrm{e}^{b^2+2\,a}. \tag{J.23}$$

$$\gamma_1 = \sqrt{\mathrm{e}^{b^2-1}}\left(\mathrm{e}^{b^2}+2\right). \tag{J.24}$$

$$\gamma_e = 3\,\mathrm{e}^{2\,b^2} + 2\,\mathrm{e}^{3\,b^2} + \mathrm{e}^{4\,b^2} - 6. \tag{J.25}$$

$$\mu_3 = \sqrt{\mathrm{e}^{b^2-1}}\left(\mathrm{e}^{b^2} - \mathrm{e}^{b^2+2\,a}\right)^{\frac{3}{2}}\left(\mathrm{e}^{b^2}+2\right). \tag{J.26}$$

$$\mu_4 = \left(\mathrm{e}^{b^2} - \mathrm{e}^{b^2+2\,a}\right)^2\left(3\,\mathrm{e}^{2\,b^2} + 2\,\mathrm{e}^{3\,b^2} + \mathrm{e}^{4\,b^2} - 3\right). \tag{J.27}$$

$$\kappa_4 = \left(\mathrm{e}^{b^2} - \mathrm{e}^{b^2+2\,a}\right)^2\left(3\,\mathrm{e}^{2\,b^2} + 2\,\mathrm{e}^{3\,b^2} + \mathrm{e}^{4\,b^2} - 3\right) - 3\left(\mathrm{e}^{b^2} - \mathrm{e}^{b^2+2\,a}\right)^2. \tag{J.28}$$

Laplace distribution (Lp) [157]

$$\mu_2 = 2\,b^2; \qquad \mu_3 = 0; \qquad \mu_4 = 12\,b^2; \tag{J.29}$$

$$\gamma_1 = 0; \qquad \gamma_e = 3; \qquad \kappa_4 = 6\,b^2. \tag{J.30}$$

Rice distribution (Rc) [158]

$$\mu_k^{'} = b^k 2^{k/2}\,\Gamma(1+k/2)\;{}_1F_1(-k/2;1;-a^2/2b^2). \tag{J.31}$$

where

$${}_1F_1(-k/2;1;-a^2/2b^2) = \sum_{n=0}^{\infty}\frac{(-k/2)^{(n)}\,(-a^2/2b^2)^n}{1^{(n)}n!} \tag{J.32}$$

is the confluent hypergeometric function a.k.a. the Kummer function (of the first kind) [159, Eq. 13.2.2]. In Equation (J.32), $\times^{(n)}$ is the "rising factorial":

$$\times^{(n)} = \times(\times+1)(\times+2)\cdots(\times+n-1)\,.$$

Gamma distribution (G) [160]

$$\mu_2 = \frac{a}{b^2}; \qquad \mu_3 = \frac{2\left(\frac{a}{b^2}\right)^{\frac{3}{2}}}{\sqrt{a}}; \qquad \mu_4 = \frac{3\,a\,(a+2)}{b^4}; \tag{J.33}$$

$$\gamma_1 = \frac{2}{\sqrt{a}}; \qquad \gamma_e = \frac{6}{a}; \qquad \kappa_4 = \frac{6\,a}{b^4}. \tag{J.34}$$

Inverse gamma distribution (IG) [133, Section A.3.2.2]

$$\mu_2 = \frac{b^2}{(a-1)^2(a-2)}\,, \quad \text{for } a>2. \tag{J.35}$$

$$\mu_3 = \frac{4\sqrt{a-2}\left(\frac{b^2}{\left((a-1)^2\,(a-2)\right)}\right)^{\frac{3}{2}}}{a-3}\,, \quad \text{for } a>3. \tag{J.36}$$

$$\mu_4 = \frac{b^4\left(\frac{30\,a-66}{(a-3)\,(a-4)}+3\right)}{(a-1)^4\,(a-2)^2}\,, \quad \text{for } a>4. \tag{J.37}$$

$$\gamma_1 = \frac{4\sqrt{a-2}}{a-3}\,, \quad \text{for } a>3. \tag{J.38}$$

$$\gamma_e = \frac{30\,a-66}{(a-3)(a-4)}\,, \quad \text{for } a>4. \tag{J.39}$$

$$\kappa_4 = \frac{6\,b^4\,(5\,a-11)}{(a-1)^4\,(a-2)^2\,(a^2-7\,a+12)}\,, \quad \text{for } a>4. \tag{J.40}$$

Inverse Gaussian distribution (IGs) [161]

$$\mu_2 = \frac{a^3}{b}. \tag{J.41}$$

$$\mu_3 = 3\sqrt{\frac{a}{b}}\left(\frac{a^3}{b}\right)^{\frac{3}{2}}. \tag{J.42}$$

$$\mu_4 = \frac{3\,a^6\,(5\,a+b)}{b^3}. \tag{J.43}$$

$$\gamma_1 = 3\left(\frac{a}{b}\right)^{1/2}. \tag{J.44}$$

$$\gamma_e = \frac{15a}{b}. \tag{J.45}$$

$$\kappa_4 = \frac{15\,a^7}{b^3}. \tag{J.46}$$

Paralogistic distribution (PLg) [133, Appendix A.2.3.4]

$$\mu'_k = \frac{b^k\Gamma\left(1+k/a\right)\Gamma\left(a-k/a\right)}{\Gamma\left(a\right)}\,, \quad -a<k<a^2. \tag{J.47}$$

Weibull distribution (W) [133, Section A.3.2.3]

$$\mu_2 = b^2\left[\Gamma\left(1+\frac{2}{a}\right)-\left(\Gamma\left(1+\frac{1}{a}\right)\right)^2\right] \tag{J.48}$$

$$\mu_3 = 2\,b^3\,\Gamma\left(\frac{1}{a}+1\right)^3 - 3\,\Gamma\left(\frac{2}{a}+1\right)b^3\,\Gamma\left(\frac{1}{a}+1\right)+\Gamma\left(\frac{3}{a}+1\right)b^3 \tag{J.49}$$

$$\begin{aligned}\mu_4 = {} & -3\,b^4\,\Gamma\left(\frac{1}{a}+1\right)^4 + 6\,\Gamma\left(\frac{2}{a}+1\right)b^4\,\Gamma\left(\frac{1}{a}+1\right)^2 \\ & -4\,\Gamma\left(\frac{3}{a}+1\right)b^4\,\Gamma\left(\frac{1}{a}+1\right)+\Gamma\left(\frac{4}{a}+1\right)b^4\end{aligned} \tag{J.50}$$

$$\gamma_1 = \frac{\Gamma\left(1+\frac{3}{a}\right)b^3 - 3\mu\sigma^2-\mu^3}{\sigma^3} \tag{J.51}$$

$$\gamma_e = \frac{b^4\Gamma(1+\frac{4}{a})-4\gamma_1\sigma^3\mu-6\mu^2\sigma^2-\mu^4}{\sigma^4}-3 \tag{J.52}$$

$$\begin{aligned}\kappa_4 = {} & -b^4\left(6\,\Gamma\left(\frac{1}{a}+1\right)^4 - 12\,\Gamma\left(\frac{1}{a}+1\right)^2\Gamma\left(\frac{2}{a}+1\right)\right. \\ & \left.+4\,\Gamma\left(\frac{3}{a}+1\right)\Gamma\left(\frac{1}{a}+1\right)+3\,\Gamma\left(\frac{2}{a}+1\right)^2-\Gamma\left(\frac{4}{a}+1\right)\right)\end{aligned} \tag{J.53}$$

where μ is mean, and σ^2 is the variance.

Cauchy distribution (Cy) [162] All moments are undefined.

Log Cauchy distribution (LCy) [163, Page 443] All moments are undefined.

Gumbel distribution (Gb) [164]

$$\mu_2 = \frac{\pi^2 b^2}{6} \tag{J.54}$$

$$\mu_3 = 2.4\ b^3 \tag{J.55}$$

$$\mu_4 = 14.6\ b^4 \tag{J.56}$$

$$\gamma_1 = 1.14 \tag{J.57}$$

$$\gamma_e = 2.4 \tag{J.58}$$

$$\kappa_4 = 6.5\ b^4 \tag{J.59}$$

Gompertz distribution (Go) [137, 165]

$$\mu_2 \approx \frac{2}{b^2} e^{a/b} \left\{ -\frac{a}{b}\, {}_3F_3 \left[\begin{matrix} 1,1,1 \\ 2,2,2; \end{matrix} ; \frac{a}{b} \right] + \frac{1}{2} \left[\frac{\pi^2}{6} + \left(\gamma + \ln\left(\frac{a}{b}\right) \right)^2 \right] \right\} - \left[\frac{1}{b} e^{a/b} \left(\frac{a}{b} - \ln\left(\frac{a}{b}\right) - \gamma \right) \right]^2 \tag{J.60}$$

$$\gamma_1 \approx \begin{cases} 4.15a^{0.3} - 5b^{0.49} - 1.48a + 4.31b - 4.96ab, & \text{if } a > 0; \\ \frac{-12\sqrt{6}}{\pi^3}\zeta(3), & \text{if } a \approx 0. \end{cases} \tag{J.61}$$

$$\gamma_e \approx \begin{cases} -0.75 + 34.13a^{0.253} + 20b^{0.311} - 53.51(ab)^{0.14}, & \text{if } a > 0; \\ \frac{12}{5}, & \text{if } a \approx 0. \end{cases} \tag{J.62}$$

where $\gamma = 0.57722$ is the Euler-Mascheroni constant, ${}_pF_q \left[\begin{matrix} a_1, ..., a_p \\ b_1, ..., b_q; \end{matrix} ; z \right]$ symbolizes the generalized hypergeometric function.

Shifted Gompertz distribution (sGo) [138]

$$\mu_2 = \frac{1}{b^2}\left[\left(1+\frac{1}{a}\right)\int_0^a e^{-T}\log^2(T)dT - \frac{1}{a}\int_0^a Te^{-T}\log^2 TdT - \left\{\left(1+\frac{1}{a}\right)\int_0^a e^{-T}\log(T)dT - \frac{1}{a}\int_0^a Te^{-T}\log TdT\right\}^2\right] \tag{J.63}$$

$$\mu_2 \approx \frac{\pi}{\sqrt{(6)}b}, \quad \text{if} \quad a > 50 \tag{J.64}$$

$$\gamma_1 \approx \begin{cases} 2 & \text{if } a < 0.1 \\ 1.139 & \text{if } a > 50 \end{cases} \tag{J.65}$$

$$\gamma_e \approx \begin{cases} 6 & \text{if } a < 0.1 \\ 2.4 & \text{if } a > 50 \end{cases} \tag{J.66}$$

where $T := ae^{-bx}$. For 37/F dataset (a), $a = 8.9 \times 10^{11}$; For 37/F dataset (b), $a = 1.69\times10^{12}$; For 19/F dataset, $a = 3.42\times10^{10}$; For 25/F dataset, $a = 7.59\times10^{11}$. Hence, $\mu_2 = \frac{\pi}{\sqrt{(6)}b}$, $\gamma_1 = 1.139$, and $\gamma_e = 2.4$. See Table 1 of [138] for more numerical values of γ_1 and γ_e against different values of a.

Non-central chi-squared distribution (nCS) [166]

$$\mu_2 = 2(b+2a) \tag{J.67}$$

$$\mu_3 = 8(b+3a) \tag{J.68}$$

$$\mu_4 = 12(b+2a)^2 + 48(b+4a) \tag{J.69}$$

$$\gamma_1 = \frac{2^{3/2}(b+3a)}{(b+2a)^{3/2}} \tag{J.70}$$

$$\gamma_e = \frac{12(b+4a)}{(b+2a)^2} \tag{J.71}$$

$$\kappa_4 = 2^3(3)!\,(b+3a) \tag{J.72}$$

Scaled inverse chi-squared distribution (sCS) [167]

$$\mu_2 = \frac{2a^2b^2}{(a-2)^2(a-4)}, \text{ for } a > 4 \tag{J.73}$$

$$\gamma_1 = \frac{4}{a-6}\sqrt{2(a-4)}, \text{ for } a > 6 \tag{J.74}$$

$$\gamma_e = \frac{12(5a-22)}{(a-6)(a-8)}, \text{ for } a > 8 \tag{J.75}$$

Levy distribution (L) [168] All moments are infinite.

(3-parameter PDFs)

Skew normal distribution (SN) [168]

$$\mu_2 = b^2\left(1-\frac{2\delta^2}{\pi}\right), \quad \text{where } \delta = \frac{c}{\sqrt{1+c^2}} \tag{J.76}$$

$$\gamma_1 = \frac{4-\pi}{2}\frac{\left(\delta\sqrt{2/\pi}\right)^3}{\left(1-2\delta^2/\pi\right)^{3/2}} \tag{J.77}$$

$$\gamma_e = 2(\pi-3)\frac{\left(\delta\sqrt{2/\pi}\right)^4}{\left(1-2\delta^2/\pi\right)^2} \tag{J.78}$$

Non-standardized Student's t-distribution (symT3) [169, Page 17]

$$\mu_2 = \begin{cases} \frac{b^2 c}{c-2}, & \text{if } c > 2; \\ \infty, & \text{if } 1 < c \leq 2; \\ \text{undefined}, & \text{if } c \leq 1. \end{cases} \tag{J.79}$$

$$\mu_3 = 0, \quad \text{if } c > 3. \tag{J.80}$$

$$\mu_4 = \frac{b^4 c^2\left(\frac{6}{c-4}+3\right)}{(c-2)^2}, \quad \text{if } c > 4. \tag{J.81}$$

$$\gamma_1 = \begin{cases} 0, & \text{if } c > 3; \\ \text{undefined}, & \text{if } c \leq 3. \end{cases} \tag{J.82}$$

$$\gamma_e = \begin{cases} \frac{6}{c-4}, & \text{if } c > 4; \\ \infty, & \text{if } 2 < c \leq 4; \\ \text{undefined}, & \text{if } c \leq 2. \end{cases} \tag{J.83}$$

$$\kappa_4 = \frac{6\, b^4\, c^2}{(c-2)^2\ (c-4)}, \text{ if } c > 4. \tag{J.84}$$

Birnbaum-Saunders distribution (BS) [142, Page 323]

$$\mu_2 = (cb)^2(1 + \frac{5c^2}{4}) \tag{J.85}$$

$$\gamma_1 = \frac{4c(11c^2+6)}{(5c^2+4)^{\frac{3}{2}}} \tag{J.86}$$

$$\gamma_e = 3 + \frac{6c^2(93c^2+41)}{(5c^2+4)^2} \tag{J.87}$$

Burr distribution a.k.a. Singh-Maddala distribution (Brxii) [169, Page 25],[116, Eq. (5)]

$$\mu_2 = -g_1^2 + g_2, \quad \text{where} \quad g_r = a\ \beta\left(\frac{ca-r}{c}, \frac{c+r}{c}\right) \tag{J.88}$$

$$\gamma_1 = \frac{2g_1^3 - 3g_1g_2 + g_3}{(-g_1^2+g_2)^{3/2}} \tag{J.89}$$

$$\gamma_e = \frac{-3g_1^4 + 6g_1^2g_2 - 4g_1g_3 + g_4}{(-g_1^2+g_2)^2} - 3 \tag{J.90}$$

Generalized logistic distribution type-I a.k.a. skewed logistic distribution (gLg1) [143, Section 9.2]

$$\mu_2 = b^2 \left[\psi^{(1)}(c) + \psi^{(1)}(1)\right] \tag{J.91}$$

$$\mu_3 = \psi^{(2)}(c) - \psi^{(2)}(1) \tag{J.92}$$

$$\mu_4 = \psi^{(3)}(c) + \psi^{(3)}(1) \tag{J.93}$$

$$\gamma_1 = \frac{\psi^{(2)}(c) - \psi^{(2)}(1)}{\left[\psi^{(1)}(c) + \psi^{(1)}(1)\right]^{3/2}} \tag{J.94}$$

$$\gamma_e = \frac{\psi^{(3)}(c) + \psi^{(3)}(1)}{\left[\psi^{(1)}(c) + \psi^{(1)}(1)\right]^{2}} - 3 \tag{J.95}$$

$$\kappa_4 = \psi^{(3)}(c) + \psi^{(3)}(1) - 3b^2 \left[\psi^{(1)}(c) + \psi^{(1)}(1)\right] \tag{J.96}$$

Generalized logistic distribution type II (gLg2) [143, Section 9.2]

$$\mu_2 = b^2 \left[\psi^{(1)}(c) + \psi^{(1)}(1)\right] \tag{J.97}$$

$$\mu_3 = \psi^{(2)}(1) - \psi^{(2)}(c) \tag{J.98}$$

$$\mu_4 = \psi^{(3)}(c) + \psi^{(3)}(1) \tag{J.99}$$

$$\gamma_1 = \frac{\psi^{(2)}(1) - \psi^{(2)}(c)}{\left[\psi^{(1)}(c) + \psi^{(1)}(1)\right]^{3/2}} \tag{J.100}$$

$$\gamma_e = \frac{\psi^{(3)}(c) + \psi^{(3)}(1)}{\left[\psi^{(1)}(c) + \psi^{(1)}(1)\right]^{2}} - 3 \tag{J.101}$$

$$\kappa_4 = \psi^{(3)}(c) + \psi^{(3)}(1) - 3b^2 \left[\psi^{(1)}(c) + \psi^{(1)}(1)\right] \tag{J.102}$$

Generalized logistic distribution type III (gLg3) [143, Section 9.2]

$$\mu_2 = 2\,b^2\psi^{(1)}(c) \tag{J.103}$$

$$\mu_3 = 0 \tag{J.104}$$

$$\mu_4 = \psi^{(3)}(c) \tag{J.105}$$

$$\gamma_1 = 0 \tag{J.106}$$

$$\gamma_e = \frac{\psi^{(3)}(c)}{[2\psi^{(1)}(c)]^2} - 3 \tag{J.107}$$

$$\kappa_4 = \psi^{(3)}(c) - 3[2\psi^{(1)}(c)]^2 \tag{J.108}$$

Location family with standard generalized logistic distribution type IV (gLg4) [143, Section 9.2]

$$\mu_2 = \psi^{(1)}(b) + \psi^{(1)}(c) \tag{J.109}$$

$$\mu_3 = \psi^{(2)}(b) - \psi^{(2)}(c) \tag{J.110}$$

$$\mu_4 = \psi^{(3)}(b) + \psi^{(3)}(c) \tag{J.111}$$

$$\gamma_1 = \frac{\psi^{(2)}(b) - \psi^{(2)}(c)}{[\psi^{(1)}(b) + \psi^{(1)}(c)]^{3/2}} \tag{J.112}$$

$$\gamma_e = \frac{\psi^{(3)}(b) + \psi^{(3)}(c)}{[\psi^{(1)}(b) + \psi^{(1)}(c)]^2} - 3 \tag{J.113}$$

$$\kappa_4 = \psi^{(3)}(b) + \psi^{(3)}(c) - 3\left[\psi^{(1)}(b) + \psi^{(1)}(c)\right] \tag{J.114}$$

Shifted log-logistic distribution (sLLg) [170, Pages 630–631]

$$\mu_2 = b^2 \frac{\pi}{c}\left[2\csc\left(\frac{2\pi}{c}\right) - \frac{\pi}{c}\csc^2\left(\frac{\pi}{c}\right)\right], \quad \text{for} \quad c > 2 \tag{J.115}$$

$$\gamma_1 = \frac{3\csc\left(\frac{3\pi}{c}\right) - \frac{6\pi}{c}\csc\left(\frac{2\pi}{c}\right)\csc(\frac{\pi}{c}) + 2\left(\frac{\pi}{c}\right)^2\csc^3\left(\frac{\pi}{c}\right)}{\sqrt{\frac{\pi}{c}}\left[2\csc\left(\frac{2\pi}{c}\right) - \frac{\pi}{c}\csc^2(\frac{\pi}{c})\right]^{3/2}}, \quad \text{for} \quad c > 3 \tag{J.116}$$

$$\gamma_e = \frac{\begin{array}{c}4\csc\left(\frac{4\pi}{c}\right) - \frac{12\pi}{c}\csc(\frac{3\pi}{c})\csc(\frac{\pi}{c}) \\ +12\left(\frac{\pi}{c}\right)^2\csc(\frac{2\pi}{c})\csc^2(\frac{\pi}{c}) - 3\left(\frac{\pi}{c}\right)^3\csc^4(\frac{\pi}{c})\end{array}}{\frac{\pi}{c}\left[2\csc\left(\frac{2\pi}{c}\right) - \frac{\pi}{c}\csc^2(\frac{\pi}{c})\right]^2} - 3, \quad \text{for} \quad c > 4 \tag{J.117}$$

Pearson type V (IG3) [171, Page 83], [133, Section A.3.2.2]

$$\mu_2 = \frac{b^2}{(c-1)^2(c-2)} \tag{J.118}$$

$$\gamma_1 = \frac{4\sqrt{c-3}}{c-4}, \quad c > 3 \tag{J.119}$$

$$\gamma_e = \frac{30c - 96}{(c-4)(c-5)}, \quad c > 4 \tag{J.120}$$

Exponentially modified Gaussian distribution (XG) [146, Page 1734]

$$\mu_2 = 1 + \frac{1}{b^2c^2} \tag{J.121}$$

$$\mu_3 = \frac{2}{b^3c^3} \tag{J.122}$$

$$\mu_4 = 3\left(1 + \frac{2}{b^2c^2} + \frac{3}{c^4b^4}\right) \tag{J.123}$$

$$\gamma_1 = \frac{2}{b^3c^3}\left(1 + \frac{1}{b^2c^2}\right)^{-3/2} \tag{J.124}$$

$$\gamma_e = \frac{3\left(1 + \frac{2}{b^2c^2} + \frac{3}{c^4b^4}\right)}{\left(1 + \frac{1}{b^2c^2}\right)^2} - 3 \tag{J.125}$$

$$\kappa_4 = 3\left(1 + \frac{2}{b^2c^2} + \frac{3}{c^4b^4}\right) - 3\left[1 + \frac{1}{b^2c^2}\right]^2 \tag{J.126}$$

Exponential power distribution (XP) [172]

$$\mu_2 = \frac{b^2\Gamma(3/c)}{\Gamma(1/c)} \tag{J.127}$$

$$\gamma_1 = 0 \tag{J.128}$$

$$\gamma_e = \frac{\Gamma(5/c)\Gamma(1/c)}{\Gamma(3/c)^2} - 3 \tag{J.129}$$

Generalized extreme value distribution (GEV) [148, Page 5]

$$\mu_2 = \begin{cases} b^2\left(g_2 - g_1^2\right)/c^2 & \text{if } c \neq 0, c < \frac{1}{2}, \\ b^2\,\frac{\pi^2}{6} & \text{if } c = 0, \\ \infty & \text{if } c \geq \frac{1}{2}. \end{cases} \tag{J.130}$$

$$\gamma_1 = \begin{cases} \operatorname{sgn}(c)\frac{g_3 - 3g_2g_1 + 2g_1^3}{\left(g_2 - g_1^2\right)^{3/2}} & \text{if } c \neq 0, c < \frac{1}{3}, \\ \frac{12\sqrt{6}\,\zeta(3)}{\pi^3} & \text{if } c = 0, \\ \infty & \text{if } c \geq \frac{1}{3}. \end{cases} \tag{J.131}$$

$$\gamma_e = \begin{cases} \frac{g_4 - 4g_3g_1 - 3g_2^2 + 12g_2g_1^2 - 6g_1^4}{\left(g_2 - g_1^2\right)^2} & \text{if } c \neq 0, c < \frac{1}{4}, \\ \frac{12}{5} & \text{if } c = 0, \\ \infty & \text{if } c \geq \frac{1}{4}. \end{cases} \tag{J.132}$$

Here, $g_k = \Gamma(1 - kc)$.

Davis distribution (Dv) [149, Eq. (7.11)]

$$\mu_k = \frac{b^k \Gamma(c-k)\zeta(c-k)}{\Gamma(c)\zeta(c)} \tag{J.133}$$

where $\zeta(\cdot)$ represents the Riemann Zeta function.

Tukey lambda distribution (sTK) [173, Page 79]

$$\mu_2 = \begin{cases} \frac{2}{c^2}\left(\frac{1}{1+2c} - \frac{\Gamma(c+1)^2}{\Gamma(2c+2)}\right) & \text{if } c > -1/2; \\ \frac{\pi^2}{3}, & \text{if } c = 0. \end{cases} \tag{J.134}$$

$$\gamma_1 = 0, \quad c > -1/3 \tag{J.135}$$

$$\gamma_e = \begin{cases} \frac{(2c+1)^2}{2(4c+1)} \frac{g_2^2\left(3g_2^2 - 4g_1g_3 + g_4\right)}{g_4\left(g_1^2 - g_2\right)^2} - 3,, & \text{if } c > -1/4; \\ 1.2, & \text{if } c = 0. \end{cases} \tag{J.136}$$

Here, $g_k = \Gamma(kc+1)$.

Location family with standard Beta prime distribution (BP3) [174, Page 29], [175]

$$\mu'_k = \sum_{i=0}^{k} \binom{k}{i} b^{k-i} \frac{\beta(a+i, c-i)}{\beta(a,c)} \tag{J.137}$$

Location family with standard Gompertz distribution (Go3) [137, 165, 175]

$$\mu'_k = \sum_{i=0}^{k} \binom{k}{i} c^{k-i} \frac{i}{b^i} e^{a/b} \int_1^\infty (\ln x)^{i-1} x^{-1} e^{-\frac{ax}{b}} \, d\left(\frac{a}{b}\right) \tag{J.138}$$

Non-central F-distribution (F3) [126, Chapter 30]

$$\mu'_k = \left(\frac{c}{b}\right)^k \frac{\Gamma\left(\frac{1}{2}b + k\right)\Gamma\left(\frac{1}{2}c - k\right)}{\Gamma\left(\frac{1}{2}b\right)\Gamma\left(\frac{1}{2}c\right)} \sum_{j=0}^{k} \binom{r}{j} \frac{\Gamma\left(\frac{1}{2}k\right)}{\Gamma\left(\frac{1}{2}k + j\right)} \left(\frac{1}{2}ab\right)^j. \tag{J.139}$$

Pearson type III distribution a.k.a. location family with standard gamma distribution (G3) [176]

$$\mu_2 = b^2 c \tag{J.140}$$

$$\mu_3 = \frac{2\,(b^2\,c)^{\frac{3}{2}}}{\sqrt{c}} \tag{J.141}$$

$$\mu_4 = 3\,b^4\,c\,(c+2) \tag{J.142}$$

$$\gamma_1 = \frac{2}{\sqrt{c}} \tag{J.143}$$

$$\gamma_e = \frac{6}{c} \tag{J.144}$$

$$\kappa_4 = 6\,b^4\,c \tag{J.145}$$

Location family with standard Rice distribution (Rc3) [158, 175]

$$\mu_k^{'} = \sum_{i=0}^{k} \binom{k}{i} c^{k-i} b^i 2^{i/2}\,\Gamma(1+i/2)\;{}_1F_1(-i/2;1;-a^2/2b^2). \tag{J.146}$$

Location family with standard shifted Gompertz distribution (sGo3) [138]

$$\mu_2 = \frac{1}{b^2}\left[\left(1+\frac{1}{a}\right)\int_0^a e^{-T}\log^2(T)dT - \frac{1}{a}\int_0^a Te^{-T}\log^2 TdT - \left\{\left(1+\frac{1}{a}\right)\int_0^a e^{-T}\log(T)dT - \frac{1}{a}\int_0^a Te^{-T}\log TdT\right\}^2\right] \tag{J.147}$$

$$\mu_2 \approx \frac{\pi}{\sqrt{(6)}b}, \quad \text{if} \quad a > 50 \tag{J.148}$$

$$\gamma_1 \approx \begin{cases} 2 & \text{if } a < 0.1 \\ 1.139 & \text{if } a > 50 \end{cases} \tag{J.149}$$

$$\gamma_e \approx \begin{cases} 6 & \text{if } a < 0.1 \\ 2.4 & \text{if } a > 50 \end{cases} \tag{J.150}$$

where $T := ae^{-bx}$. For 37/F dataset (a), $a = 217$; For 37/F dataset (b), $a = 428$; For 19/F dataset, $a = 463$; For 25/F dataset, $a = 232$. Hence, $\mu_2 = \frac{\pi}{\sqrt{(6)}b}$, $\gamma_1 = 1.139$, and $\gamma_e = 2.4$. See Table 1 of [138] for more numerical values of γ_1 and γ_e against different values of a.

Location family with standard Weibull distribution (W3) [133, Section A.3.2.3], [175]

$$\mu'_k = \sum_{i=0}^{k}\binom{k}{i}c^{k-i}b^i\Gamma\left(1+\frac{i}{a}\right). \tag{J.151}$$

Location family with standard paralogistic distribution (pLg3) [133, Appendix A.2.3.4], [175]

$$\mu'_k = \sum_{i=0}^{k} \binom{k}{i} c^{k-i} \frac{b^i \Gamma(1+i/a)\,\Gamma(a-i/a)}{\Gamma(a)}, \quad -a < i < a^2. \tag{J.152}$$

Skewed Cauchy distribution (sCy) [152, Page 22] Moments are undefined.

Skewed Laplace distribution (sLp3) [152, Page 14]

$$\mu_2 = b^2 \tag{J.153}$$

$$\mu_3 = 4(vb)^3\, c(3+c^2) \tag{J.154}$$

$$\mu_4 = 24(vb)^4\, (1+4c^2+c^4) \tag{J.155}$$

$$\gamma_1 = 4v^3\, c(3+c^2) \tag{J.156}$$

$$\gamma_e = 24v^4\, (1+4c^2+c^4) \tag{J.157}$$

$$\kappa_4 = 24(vb)^4\, (1+4c^2+c^4) - 3b^4 \tag{J.158}$$

where $v = [2(1+c^2)]^{-1/2}$.

Pearson type II distribution (Pii) [171, Pages 68–69]

$$\mu_2 = \frac{b^2}{2c+1} \tag{J.159}$$

$$\gamma_1 = 0 \tag{J.160}$$

$$\gamma_e = \frac{-6}{2c+3} \tag{J.161}$$

Scale family with standard inverse Gaussian distribution (sIGs) [161]

$$\mu'_k = c^k e^{b/a} \sqrt{\frac{2b}{\pi}} a^{k-1/2} K_{1/2-k}\left(\frac{b}{a}\right) \tag{J.162}$$

where $K_{\cdot}(\times)$ symbolizes the modified Bessel function of the second kind.

Inverse Burr distribution a.k.a. Dagum distribution (Briii) [177, Eq. (6.7)]

$$\mu'_k = \frac{b^k \ \beta\left(c + k/a, 1 - k/a\right)}{\beta\left(c, 1\right)}, \quad \text{if } -ac < k < a. \tag{J.163}$$

(4-parameter PDFs)

Exponential generalized beta of the second kind a.k.a. location-scale family with standard generalized logistic distribution type IV (glg44) The raw moments without the location parameter a and scale parameter d are given below [143]:

$$\begin{aligned}
m'_0 &= 1 \\
m'_1 &= \left[\psi^{(0)}(b) - \psi^{(0)}(c)\right] \\
m'_2 &= \left[\psi^{(1)}(b) + \psi^{(1)}(c)\right] + \left[\psi^{(0)}(b) - \psi^{(0)}(c)\right]^2 \\
m'_3 &= \left[\psi^{(2)}(b) - \psi^{(2)}(c)\right] + 3m'_1 m'_2 - 2{m'_1}^3 \\
m'_4 &= \left[\psi^{(3)}(b) + \psi^{(3)}(c)\right] + 4m'_1 m'_3 - 6{m'_1}^2 m'_2 + 3{m'_1}^4
\end{aligned}$$

Then, the raw moments of glg44 are [175]:

$$\mu'_k = \sum_{i=0}^{k} \binom{k}{i} a^{k-i} d^i m'_i \tag{J.164}$$

Generalized hyperbolic skewed student t (ghsT4) [115]

$$
\begin{aligned}
\mu_1' &= c + \frac{cb^2}{d-2} \\
\mu_2 &= \frac{2\beta^2 b^4}{(d-2)^2(d-4)} + \frac{b^2}{d-2} \qquad \text{(J.165)} \\
\mu_3' &= c^3 + \frac{b^2\left(3c^2 c + 3\nu\right)}{d-2} + \frac{b^4\left(3\beta + 3cc^2\right)}{(d-2)(d-4)} + \frac{b^6 c^3}{(d-2)(d-4)(d-6)} \\
\mu_4' &= c^4 + \frac{b^2\left(6c^2 c + 4c^3 c\right)}{d-2} + \frac{b^4\left(3 + 12cc + 6c^2 c^2\right)}{(d-2)(d-4)} \\
&+ \frac{b^6\left(6\beta^2 + 4cc^3\right)}{(d-2)(d-4)(d-6)} + \frac{b^8 c^4}{(d-2)(d-4)(d-6)(d-8)} \\
\gamma_1 &= \frac{\mu_3' - 3\mu_1'\mu_2' + 2{\mu_1'}^3}{(\mu_2)^{3/2}} \qquad \text{(J.166)} \\
\gamma_e &= \frac{\mu_4' - 4\mu_1'\mu_3' + 6{\mu_1'}^2\mu_2' - 3{\mu_1'}^4}{(\mu_2)^2} \qquad \text{(J.167)}
\end{aligned}
$$

Variance gamma distribution (VG) [114, Page 22]

$$
\begin{aligned}
\mu_2 &= \frac{2c}{d^2 - b^2} + \frac{4cb^2}{\left(d^2 - b^2\right)^2} \qquad \text{(J.168)} \\
\gamma_1 &= (\mu_2)^{-3/2}\left(\frac{12cb}{\left(d^2 - b^2\right)^2} + \frac{16cb^3}{\left(d^2 - b^2\right)^3}\right) \qquad \text{(J.169)} \\
\gamma_e &= (\mu_2)^{-2}\frac{12c}{\left(d^2 - b^2\right)^2}\left(\frac{(4c+8)b^4}{\left(d^2 - b^2\right)^2} + \frac{(4c+8)b^2}{\left(d^2 - b^2\right)} + c + 1\right) - 3 \qquad \text{(J.170)}
\end{aligned}
$$

Hyperbolic distribution (Hy) [114, Page 15]

$$\mu_2 = \frac{b^2}{\zeta}\frac{K_2(\zeta)}{K_1(\zeta)} + \frac{c^2 b^4}{\zeta^2}\left(\frac{K_3(\zeta)}{K_1(\zeta)} - \frac{K_2^2(\zeta)}{K_1^2(\zeta)}\right) \tag{J.171}$$

$$\begin{aligned}\gamma_1 = {\mu_2}^{-3/2}\Bigg[&\frac{c^3 b^6}{\zeta^3}\left(\frac{K_4(\zeta)}{K_1(\zeta)} - \frac{3K_3(\zeta)K_2(\zeta)}{K_1^2(\zeta)} + \frac{2K_2^3(\zeta)}{K_1^3(\zeta)}\right)\\ &+ \frac{3cb^4}{\zeta^2}\left(\frac{K_3(\zeta)}{K_1(\zeta)} - \frac{K_2^2(\zeta)}{K_1^2(\zeta)}\right)\Bigg]\end{aligned} \tag{J.172}$$

$$\begin{aligned}\gamma_e = {\mu_2}^2\Bigg[&\frac{c^4 b^8}{\zeta^4}\left(\frac{K_5(\zeta)}{K_1(\zeta)} - \frac{4K_4(\zeta)K_2(\zeta)}{K_1^2(\zeta)} + \frac{6K_3(\zeta)K_2^2(\zeta)}{K_1^3(\zeta)} - \frac{3K_2^4(\zeta)}{K_1^4(\zeta)}\right)\\ &+\frac{b^6 c^2}{\zeta^3}\left(\frac{6K_4(\zeta)}{K_1(\zeta)} - \frac{12K_3(\zeta)K_2(\zeta)}{K_1^2(\zeta)} + \frac{6K_2^3(\zeta)}{K_1^3(\zeta)}\right) + \frac{3b^4}{\zeta^2}\frac{K_3(\zeta)}{K_1(\zeta)}\Bigg] - 3\end{aligned} \tag{J.173}$$

where $K_\times$ denotes the modified Bessel function of the second kind, and

$$\zeta = b\sqrt{d^2 - c^2}.$$

Normal Inverse Gaussian distribution (NIG) [178, Eqs. (34)–(37)]

$$\mu_2 = \frac{b^2 d^2}{(d^2 - c^2)^{3/2}} \tag{J.174}$$

$$\gamma_1 = \frac{3c}{d\sqrt{b(\sqrt{d^2 - c^2})}} \tag{J.175}$$

$$\gamma_e = \frac{3(1 + 4c^2/d^2)}{\left[b(\sqrt{d^2 - c^2})\right]} \tag{J.176}$$

Pearson distribution type I (Pi) [171, Pages 69]

$$\mu_2 = \frac{b^2 cd}{(c+d)^2(c+d+1)} \tag{J.177}$$

$$\gamma_1 = \frac{2\,(d-c)\sqrt{c+d+1}}{(c+d+2)\sqrt{cd}} \tag{J.178}$$

$$\gamma_e = \frac{6[(c-d)^2(c+d+1) - cd(c+d+2)]}{cd(c+d+2)(c+d+3)} \tag{J.179}$$

Pearson distribution type IV (Piv) [179, Page 4]

$$\mu_2 = \frac{b^2}{4(c-1)^2(2c-3)}\left(4(c-1)^2+\nu^2\right), \quad \text{for } c > 3/2 \tag{J.180}$$

$$\gamma_1 = \frac{-2d}{(c-2)}\sqrt{\frac{2c-2}{(2c-1)^2+d^2}}, \quad \text{for } c > 2 \tag{J.181}$$

$$\gamma_e = \frac{6\,(c-1)\left[(2c+5)\left[(2c-1)^2+d^2\right]-8\,(2c-1)^2\right]}{(2c-3)\,(2c-4)\left[(2c-1)^2+d^2\right]}, \quad \text{for } c > 5/2 \tag{J.182}$$

Pearson distribution type VI (Pvi) [171, Chapter 12]

$$\mu'_k = \sum_{i=0}^{k}\binom{k}{i}a^{k-i}b^k\frac{\beta(c+i,d-i)}{\beta(c,d)}, \quad \text{if } -c < k < d. \tag{J.183}$$

Skewed generalized error distribution (SGED) [152, Pages 8–9]

$$\mu_k = \sum_{r=0}^{k}\binom{k}{r}\left[(1+c)^{r+1}+(-1)^r\,(1-c)^{r+1}\right](-c)^{k-r}\left(\frac{(vb)^k}{2^{r-k+1}}\right)\left[\frac{\Gamma(\frac{2}{d})^{k-r}\Gamma\left(\frac{r+1}{d}\right)}{\Gamma\left(\frac{1}{d}\right)^{k+1-r}}\right] \tag{J.184}$$

where

$$v = \sqrt{\frac{\pi\Gamma(\frac{1}{d})}{\pi(1+3c^2)\Gamma(\frac{3}{d}) - 16^{\frac{1}{d}}c^2\Gamma(\frac{1}{2}+\frac{1}{d})^2\Gamma(\frac{1}{d})}}$$

Generalized t distribution (gT4) [152, Pages 10–11]

$$\mu_2 = b^2 \tag{J.185}$$

$$\gamma_1 = 0, \quad cd > 3 \tag{J.186}$$

$$\gamma_e = \frac{2\,\beta\left(\frac{5}{c}, d-\frac{4}{c}\right)\,\beta\left(d,\frac{1}{c}\right)}{\beta\left(\frac{3}{c}, d-\frac{2}{c}\right)^2} - 3, \quad cd > 4 \tag{J.187}$$

Skewed t distribution (sT4) [152, Pages 12–13]

$$\mu_k = \sum_{r=0}^{k}\binom{k}{r}\left[(1+c)^{r+1} + (-1)^r(1-c)^{r+1}\right](-c)^{k-r}\left(\frac{(vb)^k d^{k/2}}{2^{r-k+1}}\right) \left[\frac{\beta\left(\frac{r+1}{2}, d-\frac{r}{2}\right)\,\beta\left(1, d-\frac{1}{2}\right)^{k-r}}{\beta\left(\frac{1}{2}, d\right)^{k-r+1}}\right] \tag{J.188}$$

where

$$v = \frac{1}{d^{1/2}\sqrt{(3c^2+1)(\frac{1}{2d-2}) - \frac{4c^2}{\pi}\left(\frac{\Gamma(d-\frac{1}{2})}{\Gamma(d)}\right)^2}}$$

Generalized beta prime distribution a.k.a. generalized beta distribution of second kind (gBP4) [180, Page 38]

$$\mu'_k = \frac{b^h B(c+h/a, d-h/a)}{B(c,d)} \tag{J.189}$$

Generalized lambda distribution a.k.a. asymmetric lambda distribution (gTK4) [181, Pages 96-97]

$$\mu_1' = \begin{cases} \frac{(-1)^4}{c(c+1)} + \frac{(-1)^3}{d(d+1)}, & c \neq 0, d \neq 0, c \neq d; \\ \frac{(-1)^k c}{c+1}, & c \neq 0, d = 0; \\ 0, & c = d. \end{cases} \tag{J.190}$$

$$\mu_2' = \begin{cases} \frac{1}{c^2(2c+1)} - \frac{2\beta(c+1,d+1)}{cd} + \frac{1}{d^2(2d+1)}, & c \neq 0, d \neq 0; \\ \frac{(2c^3+c^2-c-1)}{c(c+1)(2c+1)} + \frac{2(E+\psi^{(1)}(c+2))}{c(c+1)}, & c \neq 0, d = 0; \\ \frac{\pi^2}{3}, & c = d = 0. \end{cases} \tag{J.191}$$

$$\mu_3' = \begin{cases} \frac{(-1)^4}{c^3(3c+1)} - \frac{3(-1)^4\beta(c+1,2d+1)}{cd^2} + \frac{(-1)^3}{d^3(3d+1)}, & c \neq 0, d \neq 0, c \neq d; \\ \frac{3(-1)^4\left(12c^5+10c^4-4c^3-c^2+4c+1\right)}{c^2(c+1)(2c+1)(3c+1)} - \frac{3(-1)^4\left(E+\psi^{(1)}(c+2)\right)}{c^2(c+1)} & \\ + \frac{3(-1)^4\left[\frac{\pi^2}{6}+\left(E+\psi^{(1)}(c+2)\right)^2-\psi^{(1)}(c+2)\right]}{c(c+1)}, & c \neq 0, d = 0; \\ 0, & c = d. \end{cases} \tag{J.192}$$

(J.193)

$$\mu_4' = \begin{cases} \frac{1}{c^4(4c+1)} - \frac{4\beta(3c+1,d+1)}{c^3 d} + \frac{6\beta(2c+1,2d+1)}{c^2 d^2} & \\ -\frac{4\beta(c+1,3d+1)}{cd^3} + \frac{1}{d^4(4d+1)}, & c \neq 0, d \neq 0; \\ \frac{4\left(144c^7+156c^6-18c^5-24c^4+7c^3-11c^2-7c-1\right)}{c^3(c+1)(2c+1)(3c+1)(4c+1)} & \\ +\frac{12\left(E+\psi^{(1)}(3c+2)\right)}{c^3(c+1)} - \frac{12\left(E+\psi^{(1)}(2c+2)\right)}{c^3(2c+1)} & \\ +\frac{4\left(E+\psi^{(1)}(3c+2)\right)}{c^3(3c+1)} - \frac{12\left[\frac{\pi^2}{6}+\left(E+\psi^{(1)}(c+2)\right)^2-\psi^{(1)}(c+2)\right]}{c^2(c+1)} & \\ +\frac{6\left[\frac{\pi^2}{6}+\left(E+\psi^{(1)}(2c+2)\right)^2-\psi^{(1)}(2c+2)\right]}{c^2(2c+1)} & \\ +\frac{4\left[\begin{array}{c} 3\left(\frac{\pi^2}{6}-\psi^{(1)}(c+2)\right)\left(E+\psi^{(1)}(c+2)\right) \\ +\left(E+\psi^{(1)}(c+2)\right)^3+2\zeta(3)+\psi^{(2)}(c+2) \end{array}\right]}{c(c+1)}, & c \neq 0, d = 0; \\ \frac{7\pi^4}{15}, & c = d = 0. \end{cases} \tag{J.194}$$

where E symbolizes the Euler's constant and $\psi^{(\mathrm{x})}(\cdot)$ represents the polygamma function.

Note that the kth raw moment of gTK4 exists iff $c > -\frac{1}{k}$ and $d > -\frac{1}{k}$.

Johnson's SU distribution (JSu) [153, Eq. (37)]

$$\mu_2 = \frac{b^2}{2}(\omega-1)\left(\omega\cosh(2\Omega+1)\right) \tag{J.195}$$

$$\mu_3 = -\frac{b^3}{4}\sqrt{\omega}(\omega-1)^2\left[\omega(\omega+2)\sinh(3\Omega)+3\sinh(\Omega)\right] \tag{J.196}$$

$$\mu_4 = \frac{b^4}{8}(\omega-1)^2\left[\omega^2\left(\omega^4+2\omega^3+3\omega^2-3\right)\cosh(4\Omega) + 4\omega^2(\omega+2)\cosh(2\Omega)+3(2\omega+1)\right] \tag{J.197}$$

where $\omega = e^{d^{-2}}$ and $\Omega = c/d$.

References

[1] M. Muaz, Y. I. Wu, K. T. Wong, and S. Da, "A higher-order "figure-8" sensor and an isotropic sensor for azimuth-elevation bivariate direction finding," accepted on March 06, 2018 to appear in *The Journal of the Acoustical Society of America*.

[2] Y. Song, K. T. Wong, and Y. Li, "Direction finding using a biaxial particle-velocity sensor," *Journal of Sound and Vibration*, vol. 340, pp. 354–367, 2015.

[3] Y. I. Wu, K. T. Wong, X. Yuan, S.-k. Lau, and S.-k. Tang, "A directionally tunable but frequency-invariant beamformer on an acoustic velocity-sensor triad to enhance speech perception," *The Journal of the Acoustical Society of America*, vol. 131, no. 5, pp. 3891–3902, 2012.

[4] T.-c. Lin, K. T. Wong, M. O. Cordel, and J. P. Ilao, "Beamforming pointing error of a triaxial velocity sensor under gain uncertainties," *The Journal of the Acoustical Society of America*, vol. 140, no. 3, pp. 1675–1685, 2016.

[5] A. Nehorai and E. Paldi, "Acoustic vector-sensor array processing," *IEEE Transactions on Signal Processing*, vol. 42, no. 9, pp. 2481–2491, 1994.

[6] Y. I. Wu, K. T. Wong, and S.-k. Lau, "The acoustic vector-sensor's near-field array-manifold," *IEEE Transactions on Signal Processing*, vol. 58, no. 7, pp. 3946–3951, 2010.

[7] Y. I. Wu, S.-k. Lau, and K. T. Wong, "Near-field/far-field array manifold of an acoustic vector-sensor near a reflecting boundary," *The Journal of the Acoustical Society of America*, vol. 139, no. 6, pp. 3159–3176, 2016.

[8] Y. Song, Y. L. Li, and K. T. Wong, "Acoustic direction finding using a pressure sensor and a uniaxial particle velocity sensor," *IEEE Transactions on Aerospace and Electronic Systems*, vol. 51, no. 4, pp. 2560–2569, 2015.

[9] X. Liu, J. Xiang, and Y. Zhou, "Passive tracking and size estimation of volume target based on acoustic vector intensity," *Chinese Journal of Acoustics*, vol. 3, p. 003, 2001.

[10] B. Hochwald and A. Nehorai, "Identifiability in array processing models with vector-sensor applications," *IEEE Transactions on Signal Processing*, vol. 44, no. 1, pp. 83–95, 1996.

[11] P. Tichavsky, K. T. Wong, and M. D. Zoltowski, "Near-field/far-field azimuth and elevation angle estimation using a single vector hydrophone," *IEEE Transactions on Signal Processing*, vol. 49, no. 11, pp. 2498–2510, 2001.

[12] K. T. Wong, "Blind beamforming/geolocation for wideband-ffhs with unknown hop-sequences," *IEEE Transactions on Aerospace and Electronic Systems*, vol. 37, no. 1, pp. 65–76, 2001.

[13] Y. Song and K. T. Wong, "Closed-form direction finding using collocated but orthogonally oriented higher order acoustic sensors," *IEEE sensors journal*, vol. 12, no. 8, pp. 2604–2608, 2012.

[14] Y. Song and K. T. Wong, "Azimuth-elevation direction finding using a microphone and three orthogonal velocity sensors as a non-collocated subarray," *The Journal of the Acoustical Society of America*, vol. 133, no. 4, pp. 1987–1995, 2013.

[15] H. F. Olson, *Acoustical Engineering*. Princeton, New Jersey, USA: David Van Nostrand Company, Inc., 1957.

[16] B. R. Beavers and R. Brown, "Third order gradient microphone for speech reception," in *Audio Engineering Society Convention 38*, vol. 18, no. 6, 1970, pp. 636–640.

[17] B. A. Cray, V. M. Evora, and A. H. Nuttall, "Highly directional acoustic receivers," *The Journal of the Acoustical Society of America*, vol. 113, no. 3, pp. 1526–1532, 2003.

[18] D. J. Schmidlin, "Directionality of generalized acoustic sensors of arbitrary order," *The Journal of the Acoustical Society of America*, vol. 121, no. 6, pp. 3569–3578, 2007.

[19] H. Lai and K. Bell, "Cramer-rao lower bound for DoA estimation using vector and higher-order sensor arrays," in *Conference Record of the Forty-First Asilomar Conference on Signals, Systems and Computers*. IEEE, 2007, pp. 1262–1266.

[20] H. F. Olson, "Electroacoustical signal translating apparatus," Nov. 10, 1942, U.S. Patent 2,301,744. [Online]. Available: https://patents.google.com/patent/US2301744A

[21] A. M. Wiggins, "Second order differential microphone," Nov. 7, 1950, U.S. Patent 2,529,467. [Online]. Available: https://www.google.com/patents/US2529467

[22] A. M. Wiggins, "Second order differential microphone," May 15, 1951, U.S. Patent 2,552,878. [Online]. Available: https://www.google.com/patents/US2552878

[23] A. M. Wiggins, "Higher order pressure gradient microphone system having adjustable polar response pattern," Jul. 21, 1959, U.S. Patent 2,896,189. [Online]. Available: https://www.google.com/patents/US2896189

[24] M. M. Rosenfeld, "Pressure gradient transducers," Dec. 11, 1962, U.S. Patent 3,068,328. [Online]. Available: https://www.google.com/patents/US3068328

[25] A. J. Brouns, "Second-order gradient noise-cancelling microphone," in *IEEE International Conference on Acoustics, Speech, and Signal Processing*, vol. 6, 1981, pp. 786–789.

[26] D. M. Warren and S. C. Thompson, "Microphone array having a second order directional pattern," Jul. 31, 2003, U.S. Patent Application 2003/014283. [Online]. Available: https://patents.google.com/patent/US7471798

[27] S. A. Klinke, "Directional microphone arrangement and method for signal processing in a directional microphone arrangement," Sep. 18,

2003, U.S. Patent Application 2003/0174852. [Online]. Available: https://patents.google.com/patent/US20030174852

[28] H.-E. de Bree, "An overview of microflown technologies," *Acta Acustica United with Acustica*, vol. 89, no. 1, pp. 163–172, 2003.

[29] R. Miles, "High-order directional microphone diaphragm," Nov. 8, 2005, U.S. Patent 6,963,653. [Online]. Available: https://patents.google.com/patent/US6963653

[30] S. A. Klinke, "Directional-microphone and method for signal processing in same," Oct. 10, 2006, U.S. Patent 7,120,262. [Online]. Available: https://patents.google.com/patent/US7120262B2

[31] D. M. Warren and S. C. Thompson, "Microphone array having a second order directional pattern," Jun. 20, 2006, U.S. Patent 7,065,220. [Online]. Available: https://patents.google.com/patent/US7065220B2

[32] P. C. Hines, A. L. Rosenfeld, B. H. Maranda, and D. L. Hutt, "Evaluation of the endfire response of a superdirective line array in simulated ambient noise environments," in *Oceans 2000 MTS/IEEE Conference and Exhibition*, vol. 3, 2000, pp. 1489–1494.

[33] K. T. Wong and M. D. Zoltowski, "Closed-form underwater acoustic direction-finding with arbitrarily spaced vector hydrophones at unknown locations," *IEEE Journal of Oceanic Engineering*, vol. 22, no. 3, pp. 566–575, 1997.

[34] K. T. Wong and M. D. Zoltowski, "Extended-aperture underwater acoustic multisource azimuth/elevation direction-finding using uniformly but sparsely spaced vector hydrophones," *IEEE Journal of Oceanic Engineering*, vol. 22, no. 4, pp. 659–672, 1997.

[35] K. T. Wong and M. D. Zoltowski, "Self-initiating music-based direction finding in underwater acoustic particle velocity-field beamspace," *IEEE Journal of Oceanic Engineering*, vol. 25, no. 2, pp. 262–273, 2000.

[36] M. D. Zoltowski and K. T. Wong, "Closed-form eigenstructure-based direction finding using arbitrary but identical subarrays on a sparse uniform cartesian array grid," *IEEE Transactions on Signal Processing*, vol. 48, no. 8, pp. 2205–2210, 2000.

[37] H. L. Van Trees, *Optimum Array Processing: Part IV of Detection, Estimation, and Modulation Theory*. New Jersey, USA: John Wiley & Sons, Inc., 2004.

[38] I. I. Gringorten and P. J. Yepez, "The division of a circle or spherical surface into equal-area cells or pixels." Phillips Lab Hanscom Air Force Base, Massachusetts, USA, Tech. Rep. PL-TR-92-2167, 1992.

[39] D. Skarlatos, "A numerical method for calculation of probability density function of equivalent level in the case of traffic noise," *Applied Acoustics*, vol. 38, no. 1, pp. 37–50, 1993.

[40] S.-k. Tang and W. H. Au, "Statistical structures of indoor traffic noise in a high-rise city," *The Journal of the Acoustical Society of America*, vol. 106, no. 6, pp. 3415–3423, 1999.

[41] C. Don and I. Rees, "Road traffic sound level distributions," *Journal of Sound and Vibration*, vol. 100, no. 1, pp. 41–53, 1985.

[42] H. J. Purkis, "Transport noise and town planning," *Journal of Sound and Vibration*, vol. 1, no. 3, pp. 323–334, 1964.

[43] I. Griffiths and F. J. Langdon, "Subjective response to road traffic noise," *Journal of Sound and Vibration*, vol. 8, no. 1, pp. 16–32, 1968.

[44] W. E. Scholes, "Traffic noise criteria," *Applied Acoustics*, vol. 3, no. 1, pp. 1–21, 1970.

[45] D. W. Robinson, "Towards a unified system of noise assessment," *Journal of Sound and Vibration*, vol. 14, no. 3, pp. 279–298, 1971.

[46] S. Cohen, D. C. Glass, and J. E. Singer, "Apartment noise, auditory discrimination, and reading ability in children," *Journal of Experimental Social Psychology*, vol. 9, no. 5, pp. 407–422, 1973.

[47] J. S. Bradley and B. A. Jonah, "The effects of site selected variables on human responses to traffic noise, part I: Type of housing by traffic noise level," *Journal of Sound and Vibration*, vol. 66, no. 4, pp. 589–604, 1979.

[48] J. Lambert, F. Simonnet, and M. Vallet, "Patterns of behaviour in dwellings exposed to road traffic noise," *Journal of Sound and Vibration*, vol. 92, no. 2, pp. 159–172, 1984.

[49] J. M. Fields, "Reactions to environmental noise in an ambient noise context in residential areas," *The Journal of the Acoustical Society of America*, vol. 104, no. 4, pp. 2245–2260, 1998.

[50] B. Berglund, T. Lindvall, and D. H. Schwela, "Guidelines for community noise," World Health Organization, Geneva, Switzerland, Tech. Rep., 1999. [Online]. Available: http://apps.who.int/iris/handle/10665/66217

[51] S. A. Stansfeld and M. P. Matheson, "Noise pollution: non-auditory effects on health," *British Medical Bulletin*, vol. 68, no. 1, pp. 243–257, 2003.

[52] E. Öhrström, A. Skånberg, H. Svensson, and A. Gidlöf-Gunnarsson, "Effects of road traffic noise and the benefit of access to quietness," *Journal of Sound and Vibration*, vol. 295, no. 1, pp. 40–59, 2006.

[53] L. C. den Boer and A. Schroten, "Traffic noise reduction in Europe: Health effects, social costs and technical and policy options to reduce road and rail traffic noise," CE Delft, Delft, The Netherlands, Tech. Rep. 14, 2007. [Online]. Available: https://www.cedelft.eu/index.php?/publicatie/traffic_noise_reduction_in_europe/821

[54] G. Belojevic, B. Jakovljevic, V. Stojanov, K. Paunovic, and J. Ilic, "Urban road-traffic noise and blood pressure and heart rate in preschool children," *Environment International*, vol. 34, no. 2, pp. 226–231, 2008.

[55] C. Ng and S.-k. Tang, "On monitoring community noise using arbitrarily chosen measurement periods," *Applied Acoustics*, vol. 69, no. 7, pp. 649–661, 2008.

[56] D. Chapman, "National building studies: A survey of noise in British homes," Her Majesty's Stationery Office, London, UK, Tech. Rep. 2, 1948.

[57] *Noise and Buildings*, Building Research Station, Digest No. 38, Series No. 2, London, UK, 1963.

[58] M. H. Cyril, *Handbook of Noise Control*. New York, USA: McGraw-Hill Education, 1979.

[59] S. Yamaguchi and Y. Kato, "A practical method of predicting noise produced by road traffic controlled by traffic signals," *The Journal of the Acoustical Society of America*, vol. 86, no. 6, pp. 2206–2214, 1989.

[60] M. Ohta, A. Ikuta, and N. Takaki, "A prediction method of road traffic noise with non-stationary and non-Poisson type traffic flow based on the generalization of Stratonovich's theory for random point processes," *Acta Acustica United with Acustica*, vol. 70, no. 4, pp. 273–283, 1990.

[61] S.-k. Tang and S. Chu, "Noise level distribution functions for outdoor applications," *Journal of Sound and Vibration*, vol. 248, no. 5, pp. 887–911, 2001.

[62] C. Steele, "A critical review of some traffic noise prediction models," *Applied Acoustics*, vol. 62, no. 3, pp. 271–287, 2001.

[63] V. E. Taylor, J. A. Marino, J. M. Yourno, and R. K. Radliff, "Long island expressway improvement project," Federal Highway Administration, New York, USA, Tech. Rep. FHWA-NY-EIS-81-02F, Mar. 1984. [Online]. Available: https://play.google.com/store/books/details?id=UaY1AQAAMAAJ&rdid=book-UaY1AQAAMAAJ&rdot=1

[64] S.-k. Tang, "A distribution function applicable to office noise study," *Journal of Sound and Vibration*, vol. 208, no. 4, pp. 603–615, 1997.

[65] D. N. May, "Freeway noise and high-rise balconies," *The Journal of the Acoustical Society of America*, vol. 65, no. 3, pp. 699–704, 1979.

[66] J. Zhang, W. Jiang, and N. Li, "Theoretical and experimental investigations on coherence of traffic noise transmission through an open window into a rectangular room in high-rise buildings," *The Journal of the Acoustical Society of America*, vol. 112, no. 4, pp. 1482–1495, 2002.

[67] S.-k. Tang and W. Chan, "Predictability of noise indices in a high-rise residential environment," *The Journal of the Acoustical Society of America*, vol. 114, no. 3, pp. 1222–1225, 2003.

[68] C. Mak, W. Leung, and G. Jiang, "Measurement and prediction of road traffic noise at different building floor levels in Hong Kong," *Building Services Engineering Research and Technology*, vol. 31, no. 2, pp. 131–139, 2010.

[69] W. M. To, C. M. Mak, and W. L. Chung, "Are the noise levels acceptable in a built environment like Hong Kong?" *Noise & health*, vol. 17, no. 79, p. 429, 2015.

[70] D. Johnson and E. Saunders, "The evaluation of noise from freely flowing road traffic," *Journal of Sound and vibration*, vol. 7, no. 2, pp. 287–309, 1968.

[71] C. Ng and S.-k. Tang, "On the addition of two incoherent unsteady noise records of different statistical structures," *Applied Acoustics*, vol. 67, no. 2, pp. 157–184, 2006.

[72] J. F. G. de Cevallos, C. Delgado, V. M. Sáez, and J. S. Santiago, "A project of urban traffic noise control," *Acta Acustica United with Acustica*, vol. 29, no. 4, pp. 219–224, 1973.

[73] U. Kurze, "Frequency curves of road traffic noise," *Journal of Sound and Vibration*, vol. 33, no. 2, pp. 171–185, 1974.

[74] F. Blandamura and R. Spagnolo, "A mathematical model for predicting the noise of freely flowing traffic," *Acta Acustica United with Acustica*, vol. 30, no. 4, pp. 236–240, 1974.

[75] K. Takagi, K. Hiramatsu, T. Yamamoto, and K. Hashimoto, "Investigations on road traffic noise based on an exponentially distributed vehicles model–single line flow of vehicles with same acoustic power," *Journal of Sound and Vibration*, vol. 36, no. 3, pp. 417–431, 1974.

[76] S. Yamaguchi, S. Ishihara, and Y. Kato, "A fundamental consideration on evaluating noise produced by road traffic controlled by traffic signals," *Applied Acoustics*, vol. 42, no. 1, pp. 55–73, 1994.

[77] S.-k. Tang, "On the addition of two incoherent unsteady noise records of similar statistical structures," *Applied Acoustics*, vol. 63, no. 8, pp. 829–848, 2002.

[78] S.-k. Tang, "On the addition of two incoherent unsteady noise records of similar statistical structures. Part 2: effects of long time span and diurnal variations," *Applied Acoustics*, vol. 64, no. 6, pp. 541–564, 2003.

[79] H. Fletcher and W. A. Munson, "Loudness, its definition, measurement and calculation," *Bell Labs Technical Journal*, vol. 12, no. 4, pp. 377–430, 1933.

[80] "Electroacoustics - Sound level meters – Part 1: Specifications," International Electrotechnical Commission, Geneva, Switzerland, Standard 61672-1:2003, 2003.

[81] "Noise assessment," Environmental Protection Department, The Government of the Hong Kong Special Administrative Region, accessed on Feb. 21, 2018. [Online]. Available: http://www.epd.gov.hk/epd/noise_education/web/ENG_EPD_HTML/m2/index.html

[82] A. Trapletti and K. Hornik, *Time Series Analysis and Computational Finance*, 2016, R package version 0.10-35. [Online]. Available: http://CRAN.R-project.org/package=tseries

[83] J. S. Bendat and A. G. Piersol, *Random Data: Analysis and Measurement Procedures*. New Jersey, USA: John Wiley & Sons, Inc., 2012.

[84] R Core Team, *R: A Language and Environment for Statistical Computing*, R Foundation for Statistical Computing, Vienna, Austria, 2016. [Online]. Available: https://www.R-project.org/

[85] N. Johnson, S. Kotz, and R. Balakrishnan, *Continuous univariate distributions*. New Jersey, USA: John Wiley & Sons, Inc., 1994, vol. 1.

[86] K. Pearson, "X. Contributions to the mathematical theory of evolution.—II. Skew variation in homogeneous material," *Philosophical Transactions of the Royal Society of London A: Mathematical, Physical and Engineering Sciences*, vol. 186, pp. 343–414, 1895.

[87] K. Pearson, "XI. Mathematical contributions to the theory of evolution. —X. Supplement to a memoir on skew variation," *Philosophical Transactions of the Royal Society of London A: Mathematical, Physical and Engineering Sciences*, vol. 197, no. 287-299, pp. 443–459, 1901.

[88] O. Barndorff-Nielsen, "Exponentially decreasing distributions for the logarithm of particle size," *Proceedings of the Royal Society of London. Series A, Mathematical and Physical Sciences*, vol. 353, no. 1674, pp. 401–419, 1977.

[89] J. B. McDonald and Y. J. Xu, "A generalization of the beta distribution with applications," *Journal of Econometrics*, vol. 66, no. 1, pp. 133–152, 1995.

[90] P. Theodossiou, "Financial data and the skewed generalized t distribution," *Management Science*, vol. 44, no. 12-part-1, pp. 1650–1661, 1998.

[91] J. B. McDonald and W. K. Newey, "Partially adaptive estimation of regression models via the generalized t distribution," *Econometric Theory*, vol. 4, no. 3, pp. 428–457, 1988.

[92] B. E. Hansen, "Autoregressive conditional density estimation," *International Economic Review*, vol. 35, no. 3, pp. 705–730, 1994.

[93] K. P. Burnham and D. R. Anderson, *Model Selection and Multimodel Inference: A Practical Information-Theoretic Approach*. New York, USA: Springer Science & Business Media, 2003.

[94] H. Akaike, "A new look at the statistical model identification," *IEEE Transactions on Automatic Control*, vol. 19, no. 6, pp. 716–723, 1974.

[95] C. J. Stone, "Local asymptotic admissibility of a generalization of Akaike's model selection rule," *Annals of the Institute of Statistical Mathematics*, vol. 34, no. 1, pp. 123–133, 1982.

[96] H. Bozdogan, "Model selection and Akaike's information criterion (AIC): The general theory and its analytical extensions," *Psychometrika*, vol. 52, no. 3, pp. 345–370, 1987.

[97] J. DeLeeuw, "Introduction to Akaike (1973) information theory and an extension of the maximum likelihood principle," in *Breakthroughs in Statistics: Foundations and Basic Theory*, S. Kotz and N. L. Johnson, Eds. New York, USA: Springer Science & Business Media, 1993, vol. 1, pp. 599–609.

[98] H. Akaike, "Information measures and model selection," *Bulletin of the International Statistical Institute*, vol. 50, no. 1, pp. 277–291, 1983.

[99] G. Casella and R. L. Berger, *Statistical Inference*. California, USA: Duxbury Pacific Grove, 2002.

[100] I. Kaplansky, "A common error concerning kurtosis," *Journal of the American Statistical Association*, vol. 40, no. 230, pp. 259–259, 1945.

[101] Z. W. Birnbaum, "On random variables with comparable peakedness," *The Annals of Mathematical Statistics*, vol. 19, no. 1, pp. 76–81, 1948. [Online]. Available: http://www.jstor.org/stable/2236059

[102] P. H. Westfall, "Kurtosis as peakedness, 1905–2014. R.I.P." *The American Statistician*, vol. 68, no. 3, pp. 191–195, 2014.

[103] H. Elbarmi and H. Mukerjee, "Peakedness and peakedness ordering in symmetric distributions," *Journal of Multivariate Analysis*, vol. 100, no. 4, pp. 594–603, 2009.

[104] H. E. Barmi and H. Mukerjee, "Peakedness and peakedness ordering," *Journal of Multivariate Analysis*, vol. 111, pp. 222–233, 2012.

[105] H. E. Barmi and R. Wu, "On estimation of peakedness-ordered distributions," *Communications in Statistics - Theory and Methods*, vol. 46, no. 10, pp. 4855–4869, 2017.

[106] J. L. Myers and A. D. Well, *Research Design and Statistical Analysis*, 2nd ed. New Jersey, USA: Mahwah: Lawrence Erlbaum Associates, 2003.

[107] W. H. Press, S. A. Teukolsky, W. T. Vetterling, and B. P. Flannery, *Numerical Recipes in C: The Art of Scientific Computing*, 2nd ed. New York, USA: Cambridge University Press, 1992.

[108] "Case study 2 – Noise mitigation through innovative designs and measures," Housing Department, The Government of the Hong Kong Special Administrative Region, accessed on Jan. 23, 2018. [Online].

Available: https://www.housingauthority.gov.hk/mini-site/hasr1314/en/common/pdf/09.pdf

[109] "Wing Cheong Estate at Sham Shui Po," Environmental Protection Department, The Government of the Hong Kong Special Administrative Region, accessed on Jan. 23, 2018. [Online]. Available: http://www.epd.gov.hk/epd/Innovative/greeny/eng/content/wing-cheong-estate-sham-shui-po.html

[110] "Residential–Wing Cheong Estate," Paul Y. Engineering, accessed on Jan. 23, 2018. [Online]. Available: http://www.pyengineering.com/en-us/projects/details/67

[111] "General holidays for 2014," Hong Kong Special Administrative Region Government, accessed on April 01, 2018. [Online]. Available: https://www.gov.hk/en/about/abouthk/holiday/2014.htm

[112] "General holidays for 2015," Hong Kong Special Administrative Region Government, accessed on April 01, 2018. [Online]. Available: https://www.gov.hk/en/about/abouthk/holiday/2015.htm

[113] "Technical memorandum for the assessment of noise from places other than domestic premises, public places or construction sites," Environmental Protection Department, Hong Kong, Tech. Rep. section 10 of the Noise Control Ordinance, 2002. [Online]. Available: http://www.epd.gov.hk/epd/english/environmentinhk/noise/guide_ref/tm_nondomestic.html

[114] E. Hammerstein, "Generalized hyperbolic distributions: Theory and applications to CDO pricing," Ph.D. dissertation, Universität Freiburg, 2010.

[115] K. Aas and I. H. Haff, "The generalized hyperbolic skew student's t-distribution," *Journal of Financial Econometrics*, vol. 4, no. 2, pp. 275–309, 2006.

[116] P. R. Tadikamalla, "A look at the Burr and related distributions," *International Statistical Review/Revue Internationale de Statistique*, pp. 337–344, 1980.

[117] A. C. Cullen and H. C. Frey, *Probabilistic Techniques in Exposure Assessment*, 1st ed. New York, USA: Springer, 1999.

[118] S. Nadarajah, "A generalized normal distribution," *Journal of Applied Statistics*, vol. 32, no. 7, pp. 685–694, 2005.

[119] K. T. Wong, C. J. Nnonyelu, and Y. I. Wu, "A triad of cardioid sensors in orthogonal orientation and spatial collocation–its spatial-matched-filter-type beam-pattern," *IEEE Transactions on Signal Processing*, vol. 66, no. 4, pp. 895–906, 2018.

[120] K. B. Smith and A. V. van Leijen, "Steering vector sensor array elements with linear cardioids and nonlinear hippioids," *The Journal of the Acoustical Society of America*, vol. 122, no. 1, pp. 370–377, 2007.

[121] G. H. Weiss, "On the noise generated by a stream of vehicles," *Transportation Research*, vol. 4, no. 3, pp. 229–233, 1970.

[122] M. Ohta, K. Nakamura, and N. Nakasako, "A new methodological trial on probabilistic prediction of road traffic noise based on the grouping model of

Poisson-type traffic-flow," *Acta Acustica United with Acustica*, vol. 58, no. 1, pp. 39–47, 1985.

[123] U. Kurze, "Statistics of road traffic noise," *Journal of Sound and Vibration*, vol. 18, no. 2, pp. 171–195, 1971.

[124] D. Skarlatos and E. Manatakis, "Noise probability density functions for Poisson type traffic flow," *Applied Acoustics*, vol. 27, no. 1, pp. 47–55, 1989.

[125] S. Yamaguchi and Y. Kato, "A prediction method of non-stationary road traffic noise based on fluctuation patterns of an average number of flowing vehicles," *Applied Acoustics*, vol. 27, no. 2, pp. 103–118, 1989.

[126] N. Johnston, S. Kotz, and N. Balakrishnan, *Continuous Univariate Distributions*. New Jersey, USA: John Wiley & Sons, Inc., 1994, vol. 2.

[127] M. J. Fischer, *Generalized Hyperbolic Secant Distributions: With Applications to Finance*. New York, USA: Springer Science & Business Media, 2013.

[128] M. Shoukri, I. Mian, and D. Tracy, "Sampling properties of estimators of the log-logistic distribution with application to Canadian precipitation data," *Canadian Journal of Statistics*, vol. 16, no. 3, pp. 223–236, 1988.

[129] L. L. Scharf and C. Demeure, *Statistical Signal Processing: Detection, Estimation, and Time Series Analysis*. Massachusetts, USA: Addison-Wesley Reading, 1991.

[130] S. Jackman, *Bayesian Analysis for the Social Sciences*. New Jersey, USA: John Wiley & Sons, Inc., 2009.

[131] A. Abdi, C. Tepedelenlioglu, M. Kaveh, and G. Giannakis, "On the estimation of the K parameter for the Rice fading distribution," *IEEE Communications letters*, vol. 5, no. 3, pp. 92–94, 2001.

[132] V. Witkovskỳ, "Computing the distribution of a linear combination of inverted gamma variables," *Kybernetika*, vol. 37, no. 1, pp. 79–90, 2001.

[133] S. A. Klugman, H. H. Panjer, and G. E. Willmot, *Loss Models: From Data to Decisions*. New Jersey, USA: John Wiley & Sons, Inc., 2012.

[134] A. Papoulis and S. U. Pillai, *Probability, Random Variables, and Stochastic Processes*. New York, USA: Tata McGraw-Hill Education, 2002.

[135] D. J. Olive, "Applied robust statistics," Jan. 16, 2005, accessed on Mar. 14, 2018. [Online]. Available: http://www.gene-quantification.com/David-Olive-2005.pdf.

[136] R. J. Oosterbaan, "Frequency and regression analysis," in *Drainage Principles and Applications*, H. P. Ritzema, Ed. Wageningen, The Netherlands: International Institute for Land Reclamation and Improvement, 1994, vol. 16, ch. 6, pp. 175–224.

[137] A. Lenart, "The moments of the Gompertz distribution and maximum likelihood estimation of its parameters," *Scandinavian Actuarial Journal*, vol. 2014, no. 3, pp. 255–277, 2014.

[138] F. Jiménez and P. Jodrá, "A note on the moments and computer generation of the shifted Gompertz distribution," *Communications in Statistics–Theory and Methods*, vol. 38, no. 1, pp. 75–89, 2008.

[139] A. Gellman, J. B. Carlin, H. S. Stern, and D. B. Rubin, *Bayesian Data Analysis*. London, UK: Chapman & Hall, 1995.

[140] J. Nolan, *Stable Distributions: Models for Heavy-tailed Data*. Massachusetts, USA: Birkhauser, 2003, processed: 14 February 2016.

[141] J. Anděl, I. Netuka, and K. Zvára, "On threshold autoregressive processes," *Kybernetika*, vol. 20, no. 2, pp. 89–106, 1984.

[142] Z. W. Birnbaum and S. C. Saunders, "A new family of life distributions," *Journal of Applied Probability*, vol. 6, no. 2, pp. 319–327, 1969.

[143] D. Zelterman, "Univariate generalized distributions," in *Handbook of the Logistic Distribution*, N. Balakrishnan, Ed. New York, USA: Marcel Dekker, Inc., 1992, vol. 123, pp. 209–221.

[144] C. Dagum, "A model of income distribution and the conditions of existence of moments of finite order," in *Proceedings of the 40th Session of the International Statistical Institute*, vol. 46, 1975, pp. 196–202.

[145] M. Becker and S. Klößner, *Pearson Distribution System*, 2016, R package version 0.98. [Online]. Available: https://CRAN.R-project.org/package=PearsonDS

[146] E. Grushka, "Characterization of exponentially modified Gaussian peaks in chromatography," *Analytical Chemistry*, vol. 44, no. 11, pp. 1733–1738, 1972.

[147] S. Nadarajah, "A generalized normal distribution," *Journal of Applied Statistics*, vol. 32, no. 7, pp. 685–694, 2005.

[148] G. Muraleedharan, C. G. Soares, C. Lucas, and L. Wright, "Characteristic and moment generating functions of generalised extreme value distribution (GEV)," in *Sea Level Rise, Coastal Engineering, Shorelines and Tides*, L. L. Wright, Ed. New York, USA: Nova Science, 2011, pp. 269–276.

[149] C. Kleiber and S. Kotz, "Miscellaneous size distributions," in *Statistical Size Distributions in Economics and Actuarial Sciences*. New Jersey, USA: John Wiley & Sons, Inc., 2003, ch. 7, pp. 235–250. [Online]. Available: http://dx.doi.org/10.1002/0471457175.ch7

[150] M. Freimer, G. Kollia, G. S. Mudholkar, and C. T. Lin, "A study of the generalized Tukey lambda family," *Communications in Statistics - Theory and Methods*, vol. 17, no. 10, pp. 3547–3567, 1988.

[151] S. M. Kay, *Fundamentals of Statistical Signal Processing. Detection Theory*. New Jersey, USA: Prentice Hall, Englewood Cliffs, 1998, vol. 2.

[152] C. Davis, "The skewed generalized t distribution tree package vignette," 2016. [Online]. Available: https://cran.r-project.org/web/packages/sgt/vignettes/sgt.pdf

[153] N. L. Johnson, "Systems of frequency curves generated by methods of translation," *Biometrika*, vol. 36, no. 1/2, pp. 149–176, 1949.

[154] E. W. Weisstein, "Central Moment," MathWorld–A Wolfram Web Resource, accessed on Apr. 07, 2018. [Online]. Available: http://mathworld.wolfram.com/CentralMoment.html

[155] D. Hogben, R. Pinkham, and M. Wilk, "The moments of the non-central t-distribution," *Biometrika*, vol. 48, no. 3/4, pp. 465–468, 1961.

[156] E. W. Weisstein, "Student's t-Distribution," MathWorld–A Wolfram Web Resource, accessed on May 22, 2018. [Online]. Available: http://mathworld.wolfram.com/Studentst-Distribution.html

[157] E. W. Weisstein, "Laplace Distribution," MathWorld–A Wolfram Web Resource, accessed on May 22, 2018. [Online]. Available: http://mathworld.wolfram.com/LaplaceDistribution.html

[158] "RiceDistribution," Wolfram Language & System Documentation Center, accessed on May 22, 2018. [Online]. Available: http://reference.wolfram.com/language/ref/RiceDistribution.html

[159] A. O. Daalhuis, "Confluent hypergeometric functions," in *NIST Handbook of Mathematical Functions*, F. W. J. Olver, D. W. Lozier, R. F. Boisvert, and C. W. Clark, Eds. New York, USA: Cambridge University Press, 2010, ch. 13, pp. 321–349.

[160] E. W. Weisstein, "Gamma Distribution," MathWorld–A Wolfram Web Resource, accessed on May 22, 2018. [Online]. Available: http://mathworld.wolfram.com/GammaDistribution.html

[161] E. W. Weisstein, "Inverse Gaussian Distribution," MathWorld–A Wolfram Web Resource, accessed on May 22, 2018. [Online]. Available: http://mathworld.wolfram.com/InverseGaussianDistribution.html

[162] E. W. Weisstein, "Cauchy Distribution," MathWorld–A Wolfram Web Resource, accessed on May 22, 2018. [Online]. Available: http://mathworld.wolfram.com/CauchyDistribution.html

[163] A. W. Marshall and I. Olkin, "Logarithmic distributions," in *Life Distributions: Structure on Nonparametric, Semiparametric and Parametric Families*. New York, USA: Springer, 2007, vol. 50, pp. 427–449.

[164] E. W. Weisstein, "Gumbel Distribution," MathWorld–A Wolfram Web Resource, accessed on May 23, 2018. [Online]. Available: http://mathworld.wolfram.com/GumbelDistribution.html

[165] A. Lenart, "The Gompertz distribution and maximum likelihood estimation of its parameters: a revision," *Max Planck Institute for Demographic Research Working Paper*, no. 2012-008, pp. 0–19, 2012.

[166] E. W. Weisstein, "Noncentral Chi-Squared Distribution," MathWorld–A Wolfram Web Resource, accessed on May 23, 2018. [Online]. Available: http://mathworld.wolfram.com/NoncentralChi-SquaredDistribution.html

[167] "InverseChiSquareDistribution," Wolfram Language & System Documentation Center, accessed on May 23, 2018. [Online]. Available: http://reference.wolfram.com/language/ref/InverseChiSquareDistribution.html

[168] "LevyDistribution," Wolfram Language & System Documentation Center, accessed on May 23, 2018. [Online]. Available: http://reference.wolfram.com/language/ref/LevyDistribution.html

[169] M. P. McLaughlin, *Compendium of Common Probability Distributions*. Virginia, USA: Regress+ Documentation (v2.7), 2016.

[170] *Risk Analysis and Simulation Add-In for Microsoft Excel – User's Guide*, Palisade Corporation, New York, USA, July 2016.

[171] G. E. Crooks, *Field Guide to Continuous Probability Distribution*. California, USA: John Wiley & Sons, Inc., 2017, ver. 0.11 beta.

[172] "ExponentialPowerDistribution," Wolfram Language & System Documentation Center, accessed on May 23, 2018. [Online]. Available: http://reference.wolfram.com/language/ref/ExponentialPowerDistribution.html

[173] J. S. Ramberg and B. W. Schmeiser, "An approximate method for generating asymmetric random variables," *Communications of the ACM*, vol. 17, no. 2, pp. 78–82, 1974.

[174] S. D. Dubey, "Compound gamma, beta and f distributions," *Metrika*, vol. 16, no. 1, pp. 27–31, 1970.

[175] E. W. Weisstein, "Binomial Theorem," MathWorld–A Wolfram Web Resource, accessed on May 23, 2018. [Online]. Available: http://mathworld.wolfram.com/BinomialTheorem.html

[176] E. W. Weisstein, "Pearson Type III Distribution," MathWorld–A Wolfram Web Resource, accessed on May 23, 2018. [Online]. Available: http://mathworld.wolfram.com/PearsonTypeIIIDistribution.html

[177] C. Kleiber, "A guide to the dagum distributions," in *Modeling Income Distributions and Lorenz Curves*, D. Chotikapanich, Ed. Springer, 2008, pp. 97–117.

[178] D. J. Scott, D. Würtz, C. Dong, and T. T. Tran, "Moments of the generalized hyperbolic distribution," *Computational Statistics*, vol. 26, no. 3, pp. 459–476, 2011.

[179] J. Heinrich, "A guide to the pearson type iv distribution," *University of Pennsylvania*, 2004.

[180] M. Graf and D. sislava Nedyalkova, *Generalized Beta Distribution of the Second Kind: Properties, Likelihood, Estimation*, 2015, R package version 2.1. [Online]. Available: https://cran.r-project.org/web/packages/GB2/index.html

[181] P. J. van Staden, "Modeling of generalized families of probability distributions in the quantile statistical universe," Ph.D. dissertation, University of Pretoria, 2013.